TUM School of Natural Sciences

METHOD DEVELOPMENT IN SOLID-STATE NMR USING CPMG-LIKE PULSE SEQUENCE

Timur Yasko

Vollständiger Abdruck der von der TUM School of Natural Sciences der Technischen Universität München zur Erlangung des akademischen Grades eines

Doktors der Naturwissenschaften (Dr. rer. nat.)

genehmigten Dissertation.
Vorsitz: Priv-Doz. Dr. Gerd Gemmecker
Prüfer der Dissertation: 1. Prof. Dr. Bernd Reif
2. Prof. Dr. Franz Hagn

Die Dissertation wurde am 11.09.2023 bei der Technischen Universität München eingereicht und durch die TUM School of Natural Sciences am 28.11.2023 angenommen.

Abstract

The rapid development of Nuclear Magnetic Resonance (NMR) enabled to explore multiple problems in biology, such as structure determination, dynamics of proteins, and properties of inorganic materials. Magic Angle Spinning (MAS) Solid-state NMR spectroscopy has become a powerful method for characterizing the structure of big molecules such as amyloids.

However, there are many challenges, in particular the low sensitivity of the experiments. In the past, two methods have been developed to increase the signal intensities in multidimensional experiments: ultra-fast MAS spinning and deuteration of the protein. In the solid-state, the resonance line width is determined by the Anisotropy of the Bulk Magnetic Susceptibilty (ABMS) which produces a dispersion of the chemical shifts. This tensor parameter cannot be suppressed by MAS spinning.

This is an issue in experiments, that employ long delays, leading to signal loss. For example, to transfer magnetization via weak interactions, the measurement of long-range scalar couplings across hydrogen bonds requires such extended delays because of the value of the J-coupling that is usually less than 2 Hz. The Carr-Purcell-Meiboom-Gill (CPMG) pulse sequence, which consists of a set of spin echo blocks, allows to refocus inhomogeneous lines. And this potentially allows to increase the sensitivity of the signal. Furthermore, as the Hamiltonian for the ABMS interaction is similar to the dependence of the isotropic chemical shift on the nuclear spin part, the CPMG pulse scheme can also induce line narrowing. It is shown in this thesis that the T_2 CPMG and HNCO CPMG experiments yield a gain of intensity even for delays, that extend 100 msec. Further, it is demonstrated that the CPMG method can be used to detect hydrogen bonds in a protein in a substantially reduced measurement time.

In another project of this thesis, the Rotational Echo- DOuble Resonance (REDOR) experiment is applied to experimentally determine dipolar couplings and order parameters for a microcrystalline SH3 and hIAPP amyloid fibrils. While the results obtained for the SH3 are similar to results from previous experiments, the hIAPP fibril sample showed that N- and C-terminal residues have similar order parameter values.

Zusammenfassung

Die rasante Entwicklung der Kernspinresonanzspektroskopie (NMR-Spektroskopie) hat eine praktische Anwendung in verschiedenen Bereichen, wie zum Beispiel der Strukturbestimmung von Proteinen, der Proteindynamik und der Eigenschaften anorganischer Materialien, ermöglicht. Festkörper-NMR-Spektroskopie mit Rotation der Probe im magischen Winkel (MAS-NMR) ist eine effektive Methode geworden, mit der man die Struktur von Makromolekülen, wie Amyloiden, charakterisieren kann.

Allerdings stellt die Verbesserung der Sensitivität eine große Herausforderung dar. Um dieses Problem zu bewältigen, werden deuterierte Proben verwendet, die während der Messung mit hoher Frequenz um eine zum statischen Magnetfeld im magischen Winkel orientierte Achse rotiert werden. Diese Ansätze können aber die Anisotropie der magnetischen Volumensuszeptibilität (anisotropy of bulk magnetic susceptibility, ABMS) nicht unterdrücken, und werden durch schnelle $T_2\prime$-Relaxation noch verkompliziert. Der Grund liegt daran, dass Fibrille und Membranproteine nicht kugelförmig sind, deshalb hängt die Stärke der induzierten Dipolfelder von der Orientierung in Bezug auf das externe Magnetfeld ab.

Im Fall von H-Brücken ist es notwendig die Experimente mit der großen Mischzeit durchzuführen da die skalaren Kopplungswerte weniger als 2 Hz sind. Dieses Problem kann mithilfe der CPMG-Pulssequenz, die aus Spin-Echo-Teilelementen besteht, gelöst werden, wodurch die Sensitivität verbessert wird. Der Kernspinteil des ABMS-Hamiltonoperators hat die gleiche Abhängigkeit wie der Hamiltonoperator der isotropen chemischen Verschiebung, wodurch die Linienbreite durch die Anwendung der CPMG-Pulssequenz verringert werden kann. Die Untersuchungen haben festgestellt, dass T_2- und HNCO-CPMG-Experimente bei Mischzeiten von mehr als 100 ms eine Erhöhung des Signals zeigen. Das bedeutet, dass man mit dieser Methode auch skalare Kopplungen über H-Brücken beobachten kann.

Der andere Teil dieser Arbeit ist der Anwendung von REDOR Experiment gewidmet, mit dem dipolare Kopplungswerte beziehungsweise Ordnungsparameter für SH3 und hIAPP Proteine bestimmt wurden. Während die Ergebnisse für SH3 ähnlich den Werten aus der Literatur sind, doch haben die Experimente mit hIAPP demonstriert, dass Aminosäure in N-und C-Terminalen gleiches Ordnungsparameter haben.

Acknowledgements

I want to thank everyone who helped during my Ph.D. work and beyond that. First, I would like to thank Prof. Bernd Reif for allowing me to conduct research in his group, being a patient supervisor, and always being available to answer my multiple questions.

Second, I thank Riddhiman Sarkar for his guidance in the solid-state NMR field, advice, and critical notes. Despite several difficulties during my Ph.D. work, he was ready to look at several problems and try to solve them together.

Third, I would like to thank Matthias Brandl for being "our technical guru" (even if you belong to another group) and for his profound knowledge of instrumentation. Also, I would like to thank him for explaining the main NMR basics, which were very difficult for me. Your help was valuable. Thanks a lot.

Also, I would like to thank Natasha Rodina for helping with all aspects of the lab work and some bureaucratic issues. I hope I did not bother you.

I also thank Olga Sieluzycka for being a calm and friendly roommate during my Ph.D. phase. Her infinite stories and good humor could convert a dull day into a sunny and funny one.

Also, I would like to thank the former and current group members Markus Fleisch, Benita Koch, Tejaswini Pradhan, Saba Suladze, and Arpita Sundaria for having a wonderful time.

It is also worth mentioning our secretary Asita Djamschidi who was always ready to answer my questions and helped to prepare all required documents in advance.

Furthermore, of course, I would never finish my Ph.D. without the absolute support of my parents and relatives, who were always on my side and always encouraged me not to give up. In particular, I would like to thank my mother and father, who always believed in me and shared their experience.

Contents

List of Figures

List of Abbreviations

ABMS Anisotropy of Bulk Magnetic Susceptibility

ADC Analogue Digital Converter

COSY correlation spectroscopy

CP Cross Polarization

CPMG Carr-Purcell-Meiboom-Gill

DFT Density functional theory

DNA Deoxyribonucleic acid

DSO diamagnetic spin-orbit

EPR Electron Paramagnetic Resonance

FC Fermi contact

FID Free Induction Decay

H-bonds Hydrogen bonds

HH Hartmann-Hahn condition

hIAPP Human islet amyloid polypeptide

HSQC Heteronuclear Single Quantum Correlation

INEPT Insensitive Nuclei Enhanced by Polarization Transfer

MAS Magic Angle Spinning

MO Molecular orbital

NMR Nuclear Magnetic Resonance

PAS Principal Axis System

PDSD Proton Driven Spin Diffusion

PSO paramegnetic spin-orbit

REDOR Rotational Echo Double-Resonance

rf radio frequency

SD spin dipolar

TROSY Transverse relaxation optimized spectroscopy

Chapter 1

Theoretical concepts of NMR

1.1 Theory of NMR

The rapid development of quantum physics in the XX century has led to the emergence of various new fields of research: superconductivity, semiconductor physics, quantum chemistry, quantum optics, electron microscopy, and others. Electron Paramagnetic Resonance (EPR) and Nuclear Magnetic Resonance (NMR) also belong to this category. Nowadays, NMR is considered as one of the best methods for the structural determination of biological molecules. In solution, molecules undergo Brownian motion and anisotropic components of interaction tensors are averaged up to a first order. However, anisotropic tensors contribute to relaxation processes in second order. As molecule weight increases, such contributions get stronger resulting in broad resonances. Deuteration is employed to circumvent stronger relaxation by chemically limiting a number of dipolar interactions that help in obtaining narrow resonances. However, there is another part of the NMR field that studies proteins ideally without any linmitation of molecule weight. This is solid-state NMR.

The concept of NMR is based on the oscillatory response of nuclei with non-zero nuclear spin in an external magnetic field (B_0). In the presence of a magnetic field, nuclear magnetic moment starts to precess around the axis of the external magnetic field. The frequency of this precession is called th Larmor frequency.

$$\omega_o = -\gamma B_0 \tag{1.1.1}$$

Parameter γ is called the gyromagnetic ratio, defined as the ratio of magnetic moment to its angular momentum. For each isotope, this value is unique. The sign of Larmor frequency defines whether the nucleus precesses clockwise or anticlockwise.

The energy of nuclear magnetic moment (μ_0) at the external magnetic field is given as:

$$E = -\mu B_0 \tag{1.1.2}$$

The sign of energy defines the orientation of the magnetic moment.

The longitudinal magnetization along the magnetic field is undetectable because its magnitude is 4 times lower than the typical diamagnetism of the sample. NMR takes another approach to detect a signal. A transverse magnetization is created by applying a strong radio frequency (rf) pulse. When the pulse is turned off, spins resume their precessional motion. The precession frequency is equal to the precession of individual spins. The transverse magnetic moment precessed at Larmor frequency decays due to relaxation processes. This precession can be detected in an electric wire coil. The detected signal collected by the coil is called the free induction decay (FID).

Nuclei have a spin and are positively charged. Hence, they create the magnetic field. They are oriented along the axis of rotation, which is random. But if nuclei are placed in the external magnetic field, they will not be randomly oriented: they will be either parallel or antiparallel to the external magnetic field. The most preferred orientation, which requires less energy, is the low-energy state (parallel to the magnetic field), and the least preferred orientation is the high-energy state (antiparallel). Nuclei can move between these energy levels by applying a rf pulse. The minimal energy required for such a transition is:

$$\Delta E = \gamma \hbar B \tag{1.1.3}$$

As mentioned before, the orientation of nuclei depends on their properties, particularly the gyromagnetic ratio, and external magnetic field. There are lots of

atoms involved in an occupation of low and high-energy levels(on the order of Avogadro constant, $N_A \sim 6.02 * 10^{23}$). Occupation of energy level obeys Boltzmann distribution (see fig. 1.1):

$$\frac{N_{Upper}}{N_{Lower}} = \exp^{\frac{\Delta E}{kT}} = \exp^{\frac{h\nu}{kT}} \tag{1.1.4}$$

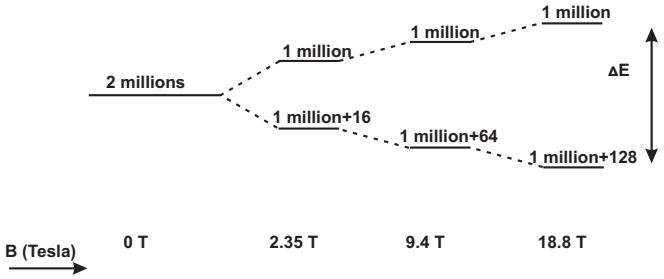

Figure 1.1: *Occupation of energy levels at different magnetic fields.*

The main feature of each NMR spectrum is the chemical shift (σ). It is unique for each nucleus in the molecule and identifies the observed material's structure. Each atom has its resonance frequency:

$$\omega = -\gamma(1-\sigma)B \tag{1.1.5}$$

Chemical shift arises from different shielding of nuclei by the electrons in the external magnetic field. The chemical shift can be expressed in ppm (parts per million) to make it independent of the B_0. For example, typical values for the chemical shift for ^{1}H atom is $\approx$ 10 ppm, for ^{13}C and ^{15}N $\approx$ 300 ppm. Chemical shift (σ) is defined by sample (ν_{sample}) and reference (ν_{ref}) frequencies:

$$\sigma = \frac{\nu_{sample} - \nu_{ref}}{\nu_{ref}} \tag{1.1.6}$$

The electronic environment of electrons is anisotropic (not symmetric). There-

fore, chemical shift is also anisotropic.

1.1.1 Theory of Solid-State NMR

The principle of solution-state NMR is based on the fact that molecules tumble with Brownian motion. Therefore, anisotropic compounds of interactions are averaged out (dipolar coupling, J-coupling, and quadrupolar coupling). As a consequence, spectra have a narrow linewidth. This is not the case in solid-state since molecules do not tumble and are close to each other in space, making spectral lines broad (see fig. 1.2). The averaging of dipolar, chemical shift anisotropy and quadrupolar interactions can be achieved at a certain angle between the rotor and the external magnetic field called Magic Angle. The magnitude of this angle is equal to 54.74°, and it is called Magic Angle Spinning (MAS).

The total energy of a spin system is described by Hamiltonian (Hamilton operator), which expresses all possible interactions in a particular system. The Hamiltonian is considered as the sum of Zeeman, chemical shift (CS), J-coupling, dipolar coupling (dd), and rf terms and can be expressed as:

$$\widehat{H} = \widehat{H}_{Zeeman} + \widehat{H}_{rf} + \widehat{H}_{CS} + \widehat{H}_{J} + \widehat{H}_{dd} \tag{1.1.7}$$

The Zeeman Hamiltonian is responsible for the interaction between the magnetic field and magnetic moment of an atom ($\mu_z = -\gamma I_z$) is given by:

$$\widehat{H}_{Zeeman} = -\gamma B I_z \tag{1.1.8}$$

Since the Zeeman Hamiltonian is dominant among all other terms Hamiltonian, it is practical to represent it in a rotating frame:

$$\widehat{H}_{Zeeman} = (\omega_o - \omega_{ref}) I_z = \Omega_0 I_z \tag{1.1.9}$$

where ω_o is the Larmor frequency, ω_{ref} is the reference frequency in the rotating frame, and Ω_0 is the offset frequency. The rf Hamiltonian in the same rotating frame has the following form:

$$\widehat{H}_{rf} = \omega_{nut}(I_x \cos(\phi) + I_y \sin(\phi)) \tag{1.1.10}$$

where ω_{nut} is the nutation frequency and serves as a measure of the rf field amplitude, I_x and I_y are Cartesian angular momentum operators, and ϕ is the pulse phase.

The Hamiltonian for the chemical shift is represented by an offset frequency in the rotating frame

$$\widehat{H}_{CS} = \gamma I \sigma B = \gamma(I_x \sigma_{xx}^{PAS} + I_y \sigma_{yy}^{PAS} + I_z \sigma_{zz}^{PAS}) \tag{1.1.11}$$

where σ^{PAS} corresponds to the chemical shift tensor in the principal axis system (PAS) where the matrix is diagonal

$$\sigma^{PAS} = \begin{pmatrix} \sigma_{xx}^{PAS} & 0 & 0 \\ 0 & \sigma_{yy}^{PAS} & 0 \\ 0 & 0 & \sigma_{zz}^{PAS} \end{pmatrix} \tag{1.1.12}$$

The components of chemical shift in PAS can be used to define the isotropic chemical shift (σ_{iso}), anisotropy(δ), and asymmetry (η)

$$\sigma_{iso} = \frac{1}{3}(\sigma_{xx}^{PAS} + \sigma_{yy}^{PAS} + \sigma_{zz}^{PAS}) \tag{1.1.13}$$

$$\delta = \sigma_{zz}^{PAS} - \sigma_{iso} \tag{1.1.14}$$

$$\eta = \frac{\sigma_{yy}^{PAS} - \sigma_{xx}^{PAS}}{\sigma_{zz}^{PAS} - \sigma_{iso}} \tag{1.1.15}$$

By appyling a rotation matrix R(α,β,γ), where α, β, γ refer to Euler angles, the expression for the chemical shift in PAS can be written in the following form:

$$\sigma^{CS,PAS}(\beta, \gamma) = \frac{\delta}{2}(3\cos^2\beta - 1 - \eta \sin^2\beta \cos(2\gamma)) \tag{1.1.16}$$

The presence of scalar coupling (J-coupling) originates from the bonding electrons running between nuclear spins. The J-coupling is mediated through chemical bonds and provides the local electronic environment. The magnitude of this coupling is small compared to the dipolar coupling and varies between 1-2 Hz for long-range bonds (for example, ${}^{3h}J_{NC}$) to approximately 90-150 Hz in one-bond couplings between ${}^{1}H -{}^{13} C$ or ${}^{1}H -{}^{15} N$. The Hamiltonian for scalar coupling can be written

in the following form:

$$\widehat{H}_J = 2\pi J_{IS}(\vec{I} \cdot \vec{S}) \tag{1.1.17}$$

This expression reduces to the expression for heteronuclear coupling, due to doubly rotating frame

$$\widehat{H}_J = 2\pi J_{IS} I_z S_z \tag{1.1.18}$$

Unlike the chemical shift, J-coupling is independent of the external magnetic field. Furthermore, the J-coupling has a sign. The sign is positive if spins have the same sign of gyromagnetic ratio connected by one chemical bond, and the opposite sign if spins have opposite signs of gyromagnetic ratio.

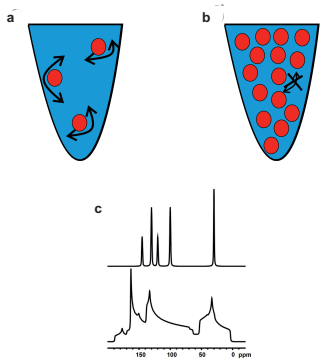

Figure 1.2: ***(a)**: Illustration of how molecules are placed for solution-state NMR. Molecules tumble in solution. **(b)**: Typical example of solid-state protein where molecules do not tumble. **(c)**: 1D spectra for solution (top) and solid (bottom) NMR. Figure from [3].*

The Hamiltonian for dipolar coupling for 2 particles with spin $\frac{1}{2}$ is given by

$$\widehat{H}_{dd} = b_{12}\left(\frac{3}{r^3}(\vec{I} \cdot \vec{r}(\vec{S} \cdot \vec{r}) - \vec{I}\vec{S})\right) \tag{1.1.19}$$

where $b_{12} = -\mu_0 \frac{\gamma_1 \gamma_2 \hbar}{4\pi r^3}$ is a dipolar coupling constant, μ_0 is magnetic permeability, and $\vec{r}$ is the distance between nuclei and spins are represented as $\vec{I}$ and $\vec{S}$. This expression will be derived in the following section.

Consider a system of 2 charged particles q_1 and q_2 with radiuses r_1 and r_2,

respectively. Coulomb's law can be written in the following way

$$\vec{F} = k * q_1 * q_2 \frac{\vec{r_2} - \vec{r_1}}{|\vec{r_2} - \vec{r_1}|^3} \tag{1.1.20}$$

The electric field induced by a point charge q_1 has the following form

$$\vec{E} = \frac{\vec{F}}{q_2} = k * q_1 * \frac{\vec{r_2} - \vec{r_1}}{|\vec{r_2} - \vec{r_1}|^3} \tag{1.1.21}$$

From another side, the electric field can be expressed from the gradient of an electric potential $\vec{E} = -\nabla\phi$. This formula can be written using a dipole $\vec{p_1} = q_1 * l$

$$\vec{E} = k * \left(-\frac{p_1}{r^3} + \frac{3(\vec{p_1} \cdot \vec{r})\vec{r}}{r^5} \right) \tag{1.1.22}$$

The interaction energy of 2 charged particles can be written:

$$W = \vec{p_2} \cdot \vec{E_1} = k * \left(-\frac{p_1 * p_2}{r^3} + \frac{3(\vec{p_1} \cdot \vec{r}(\vec{r} \cdot \vec{p_2}))}{r^5} \right) \tag{1.1.23}$$

In magnetostatics, the expression is analogous to magnetic dipoles. Also, this expression can be rewritten using polar coordinates. In the secular approximation, non-frequency dependant terms are retained, and one obtains

$$\widehat{H} = -\mu_0 \frac{\gamma_1 \gamma_2 \hbar}{4\pi r^3} * \frac{3\cos^2(\beta) - 1}{2} * (3I_z S_z - \mathbf{IS}) \tag{1.1.24}$$

In this expression, angle β refers to the angle between axis z and the line, connecting S and origin (I). This expression becomes 0 if $3\cos^2(\beta) - 1 = 0 \Rightarrow \beta = 54.74°$ (Figure 1.3).

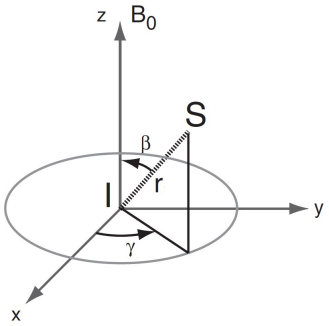

Figure 1.3: *Spherical coordinate system for 2 particles. Figure from [6].*

In the rotor fixed frame, the Hamiltonian can be represented by spatial and nuclear spin operators. Under MAS, one can suppress the dipolar interaction to the first order. Dipolar interaction under MAS can be written using Wigner rotation matrices

$$\widehat{H}_{dd} = \sum_{m=-2}^{m=2} \omega_{0,m}(\Omega_{set}) \exp^{im\omega_r t} \widehat{T}_{20} \tag{1.1.25}$$

$$\widehat{T}_{20} = \frac{1}{\sqrt{6}} \left(2I_z S_z - \frac{1}{2} I^+ S^- - \frac{1}{2} I^- S^+ \right) \tag{1.1.26}$$

where $\widehat{T}_{20}$ is nuclear spin operator and $\omega_{0,m}(\Omega)$ are spatial terms with spherical angles $\Omega_{set} = \{\alpha, \beta\}$. It turns out that the term m≠0 are zero. Hence, $\omega_{0,m}$ can be represented in a laboratory frame using the Wigner rotation matrix

$$\omega_{0,m} = -2b_{IS} d^2_{0,-m}(\beta_{CR}) \exp\{[im(\gamma_{CR} + \omega_{rt} t)]\} d^2_{-m,0}(\beta_{RL}) \tag{1.1.27}$$

where $d^2_{0,-m}(\beta_{CR})$ and $d^2_{0,-m}(\beta_{RL})$ are reduced Wigner rotation matrices with angles in crystal fixed-rotor(CR) frame and rotor-laboratory(RL) frame.For m=0 this expression becomes zero if $\beta_{RL} = 54.7°$.

However, it is insufficient to put the rotor at a magic angle to let it spin. It is also necessary to achieve a high spinning speed so that the spinning frequency would be commensurate to the size of the anisotropic interaction, which is typically on the order of kHz except for quadrupolar coupling (which can be MHz) (Figure 1.4). Besides, the maximum spinning frequency is limited by the size of a rotor and by the speed of sound(see table) [4].

Diameter, mm	**Maximum spinning frequency, kHz**	**sample volume μl**
4	15	70
3.2	25	30
1.6	40	8
1.3	67	1.7
0.7	111	0.7

Table 1.1: Rotor diameter and the corresponding limited spinning frequency with the amount of sample required to balance the rotor.

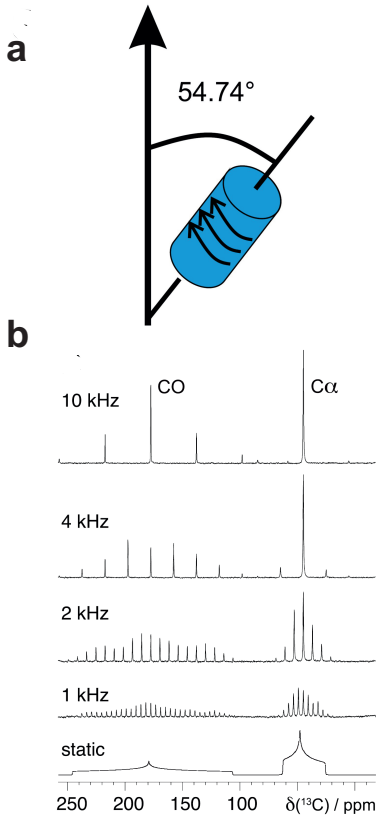

Figure 1.4: ***(a)*** *Schematic representation of NMR rotor relative to the external magnetic field.* ***(b)*** *The 1D spectrum of glycine. With the increased spinning frequency, the linewidth decreases. Figure from [5].*

1.1.2 Polarization transfer techniques

NMR can give information about the interaction of atoms via their internuclear interactions. It can be done by polarization transfer, where the magnetization from atom I goes to atom S. Most NMR experiments start with the excitation of a proton atom because of its high gyromagnetic ratio, which is 4 times larger than for carbon and 10 times larger than for nitrogen. However, two polarization techniques make it possible to transfer polarization: Insensitive Nuclei Enhanced by Polarization Transfer (INEPT, figure 1.5) and Cross Polarization (CP, figure 1.6).

The INEPT scheme starts with the excitation on the I channel by applying $\pi/2$ pulse on y-axis, which results in an I_x operator. The next step is spin echo (homonu-

clear or heteronuclear, it depends on I and S atoms), where J-coupling and chemical shift contributions are only considered. In case $\tau = \frac{1}{2J}$ the magnetization becomes antiphase $2I_yS_z$. The π pulses serve to refocus chemical shift evolution. Finally, by applying $\pi/2$ pulses on both channels, the magnetization becomes $-2S_yI_z$. Usually, most experiments are proton detected. Hence, magnetization goes back proton via a retro-INEPT process.

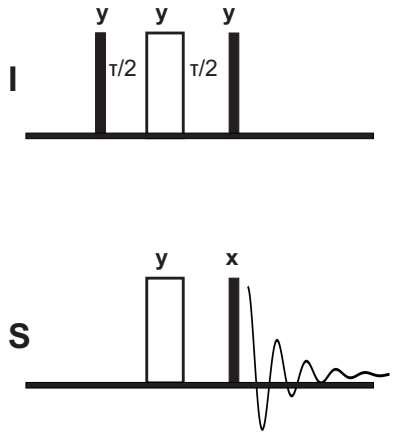

Figure 1.5: *INEPT scheme for polarization transfer.*

In solid-state NMR, CP is commonly used as it utilizes dipolar coupling. The principle of this technique is based on Hartmann-Hahn (HH) condition:

$$\omega_I = \omega_S \tag{1.1.28}$$

$$\gamma_I B_I = \gamma_S B_S \tag{1.1.29}$$

It starts with the excitation of magnetization on the I channel, and then a spin lock field is applied to either the I or S channels. Effective polarization transfer happens under HH condition. Typical rf fields vary between 50 kHz and 100 kHz. Typical CP contact time is on the order of 1 msec in organic solids. Under MAS, the matching condition becomes

$$\omega_I = \omega_S + n\omega_r \tag{1.1.30}$$

where ω_r refers to the rotor frequency and $-2 \leq n \leq 2$.

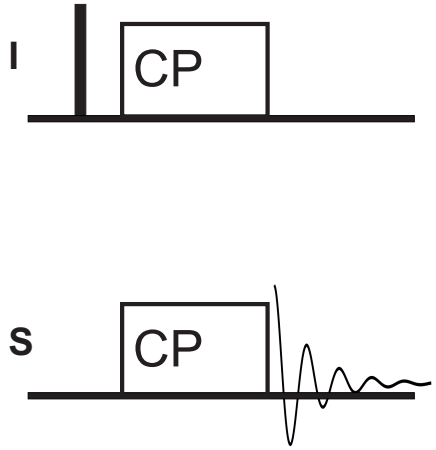

Figure 1.6: *CP scheme for polarization transfer.*

1.1.3 Practical application of solid-state NMR

NMR has become popular in different research fields, including chemistry, biology, quantum computers, and metal-organic frameworks. This section is focused mainly on biological application for measuring interatomic distances and assignment methods.

Assignment methods for structural biology

Resonance assignment is a crucial step to start the structural analysis of any protein. The protein is considered a sequence of several amino acids. This sequence has to be identified (or assigned). Three-dimensional experiments are implemented for this. The isotope labeling of the protein is a fundamental aspect of such an experiment. Proteins are synthesized via bacteria. These bacteria are placed in a medium that is full of salts and other microelements necessary for them. If an ammonium chloride is added to this medium with an isotope ^{15}N and glucose with ^{13}C, then the protein becomes labeled with nitrogen and carbon atoms, respectively. After this, a 1D spectrum has to be launched to find out whether it is possible to observe functional groups (see figure 1.7)

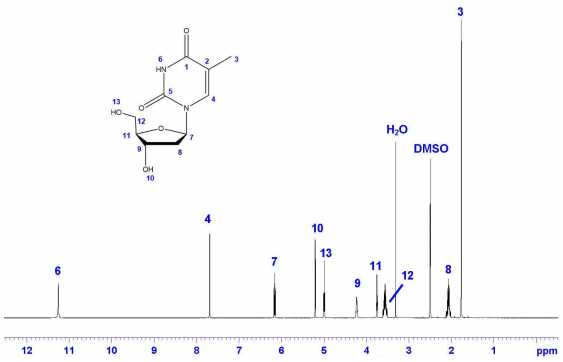

Figure 1.7: *1D proton spectrum of thymidine. Figure from [1].*

However, 1D spectra do not help assign proteins with a large molecular mass. In addition to that, spectral lines become very broad. Therefore, multidimensional experiments are implemented. A standard 2D experiment is a Heteronuclear Single Quantum Correlation (HSQC). This experiment gives a correlation between N-H atoms in an amide bond via J-coupling. The mechanism is based on the magnetization transfer from the proton to the nitrogen atom and then back for detection. Based on the results, it is possible to quantify a sample's quality and determine whether one should do additional labeling or deuterate it.

Triple resonance experiments are necessary to complete a full assignment of the protein. Multiple pulse schemes such as CBCANNH, CBCA(CO)NNH and others. CBCANNH experiment makes a correlation between amide group NH with Cα, and Cβ chemical shifts for each residue with the preceding. CBCA(CO)NNH experiment correlates only amide group only to the preceding Cα Cβ chemical shifts (see figure 1.8).

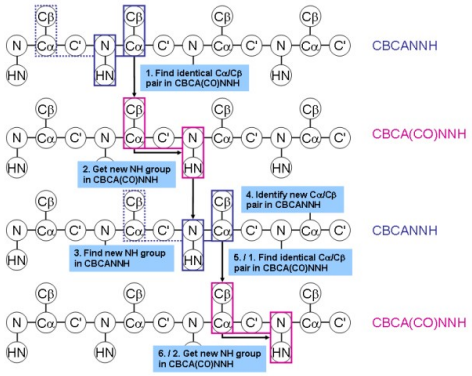

Figure 1.8: *Triple resonance assignment experiments. Figure from [2].*

Internuclear distance measurements

There are two types of atom bonds. If atoms are equivalent, it is called a homonuclear bond. Otherwise, it is a heteronuclear bond.

In homonuclear atoms, a series of 2D experiments are performed to measure the intensity of cross-peaks using Proton Driven Spin Diffusion (PDSD). The experiment starts with magnetization transfer from protons to least sensitive atoms (^{13}C, for example) to create a transversal magnetization. A decoupling is used to suppress a heteronuclear interaction. Then, the magnetization is oriented along the z-axis during the mixing time, usually between 1 msec and 1 sec in organic compounds. Spin diffusion occurs during this time, characterized by the spontaneous magnetization exchange between spins due to the dipolar interaction.

As for the heteronuclear atoms, the Rotational Echo DOuble-Resonance experiment (REDOR) is considered one of the most powerful methods in solid-state NMR. The main part is represented by a spin echo with a π pulse on the most sensitive atom (^{1}H). Furthermore, a set of π pulses are set in an insensitive atom before and after the central π pulse on the proton. The dipolar coupling is averaged every rotor period. Therefore, π pulses on insensitive atoms must be placed every half rotor

period so that the dipolar Hamiltonian will not vanish (see figure 1.9).

REDOR consists of 2 experiments: with and without a set of π pulses. It helps to get rid of effects from spin-spin relaxation. And finally, the ratio from 2 experiments at different dephasing times is defined, which gives a Bessel function of the first order.

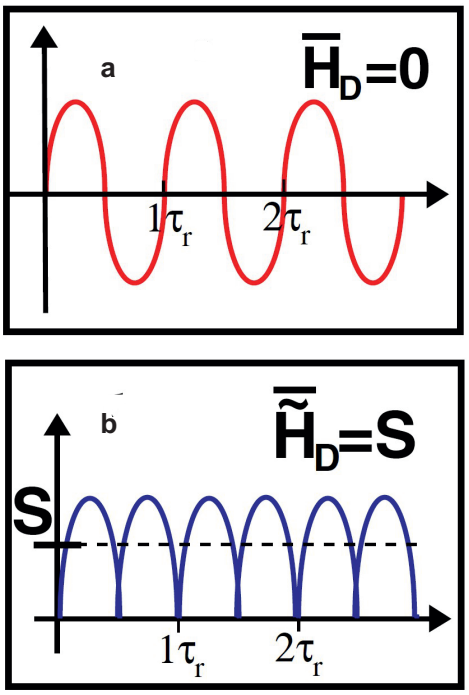

Figure 1.9: *Principle of REDOR experiment.* ***(a)*** *No π pulses are applied on insensitive nuclei.* ***(b)*** *π pulses are applied, and the dipolar Hamiltonian is non-zero. Figure from [6].*

1.1.4 The setup of the NMR spectrometer

The schematic representaion of NMR spectrometer is shown in figure 1.10. The key element is a magnet. It is a coil of superconducting wire where the electric current flows and the magnetic field is induced. The whole system is under low temperatures (less than 6K). This is because a magnet is superconducting. The main advantage is that the current flows forever without any supply. On another side, it is necessary to keep the magnet in a helium medium which is expensive. As the helium evaporates,

this system is shielded with liquid nitrogen.

The next component is an NMR sample(rotor for solid-sate NMR) with a rf coil that detects the magnetization signal. It is required to put the rotor close to the center of a coil for signal sensitivity optimization. The transmitter is responsible for applying rf pulses and receiver for detecting signals. The frequency synthesizer serves as a source of rf pulses, creating a signal at a stable frequency.

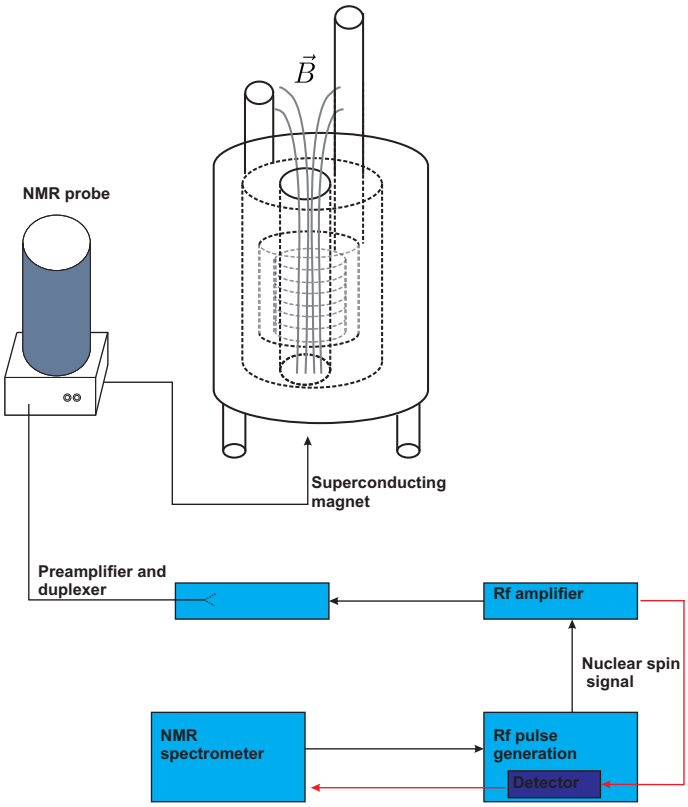

Figure 1.10: *The scheme of NMR spectrometer. Main components are superconducting magnet, NMR probe, preamplifier with a duplexer, rf amplifier, rf pulse generator and NMR spectrometer with a computer. Adapted from [7].*

The detected NMR signal from the sample is weak due to the number of atoms involved in the signal generation. Modern electronic devices have solved this problem by creating amplifiers. The first pre-amplifier is placed close to the probe. It magnifies a signal before it reaches a console of a spectrometer. A duplexer is an

extra element separating signals from the receiver and the transmitter. This is because the coil can simultaneously generate hundreds of Watts of rf power and detect a signal of several μV. The duplexer serves as an acting switch: when the rf power is routed to the probe, the received is disconnected and opposite. An analog-digital converter (ADC) serves for signal transformation. ADC samples data points and represents them as FID.

Chapter 2

CPMG pulse scheme

2.1 Development of relaxation dispersion NMR

In solution-state NMR, the methods for relaxation dispersion were developed in 1950s [8]. The first experiment was proposed by Erwin Hahn [9] and called spin echo. This experiment was designed for the determination of T_2 relaxation time without the effect of inhomogeneous magnetic field. The experiment consisted of 2 $\pi/2$ pulses, 2 τ delays and echo (signal detection). It can be written as

$$\pi/2_x - \tau - \pi/2_x - \tau - echo \tag{2.1.1}$$

where τ is large enough for dephasing the transverse magnetization. The experiment is repeated several times at different evolution times τ. The T_2 is determined from derived from the exponential decay of echo amplitudes $A(\tau) = A(0) * \exp^{\frac{-\tau}{T_2}}$. However, Hahn noticed that the experiment was sensitive to molecular diffusion, therefore, in the case of macroscopic motion, individual magnetic moments "move in the same sense and at the same rate before and after the refocusing pulse". As a result, only half of the initial magnetization was observed in Hahn echo.

Carr and Purcell [10] suggested a modification of the Hahn echo experiment to eliminate the effect of molecular diffusion. Their idea was to replace the second $\pi/2$ pulse by a π pulse, which leads to the following pulse scheme:

$$\pi/2_x - \{\tau - \pi_x - \tau\}_N - echo \tag{2.1.2}$$

with N=1,2,3, ... Similar to the Hahn echo experiment, the magnetization evolves from z-axis onto -y-axis after the first $\pi/2$ pulse. Then evolution time τ starts where magnetization dephases in the transverse plane. After the π pulse, the magnetization is rotated around the x-axis, then it evolves for a second duration time τ before it refocuses along y-axis. If N is more than 1, then the refocussing repeats every time, therefore, the magnetization varies between +y and -y. In order to solve a problem with diffusion contribution, Carr and Purcell suggested applying a train of spin echoes $\{\tau - \pi_x - \tau\}_N$ implying decreasing the length of τ. If the repetition rate of the spin echo train is high (or if τ is short), then refocusing occurs before diffusion can cause a significant shift in the precession frequency of an individual magnetic moment [8].

2.2 The CPMG method

Carr-Purcell-Meiboom-Gill (CPMG) pulse scheme is a set of several spin echo blocks with a constant time evolution (CT) (see figure 2.1). All π pulses are equally spaced (τ_{CPMG}). Each π pulse reverses the Zeeman Hamiltonian and does not affect the dipolar term. As a result, T_2 curve is dependent on $\widehat{H}_{dipolar}$. The main parameter is τ_{CPMG} delay which quantifies the rate of precession of magnetization around the axis of an applied rf pulse. The overview of practical applications of CPMG is covered in this chapter.

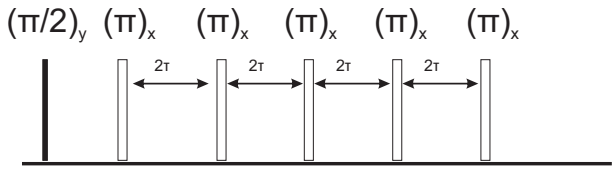

Figure 2.1: *An illustration of the CPMG pulse scheme. π pulses are spaced by 2τ delays.*

2.3 Protein dynamics

Protein dynamics has been one of the main objects of interest for most biologists. NMR spectroscopy can probe the protein dynamics over a wide range of scales, from nanoseconds to some seconds [11]. More precisely, it can be done by T_2 experiments (or R_2 dispersion experiments) which help to understand the internal dynamics and thermodynamics of proteins. The CPMG pulse scheme is extensively used for this purpose.

CT-CPMG experiment measures the R_2 relaxation rate as a function of τ_{CPMG}. The observed relaxation rate ($R_2(\nu_{CPMG})$) is a sum of theoretical relaxation rate (R_2) and the contribution of a chemical exchange ($R_{ex}(\nu_{CPMG})$) as a function of CPMG field

$$R_2(\nu_{CPMG}) = R_2 + R_{ex}(\nu_{CPMG}) \tag{2.3.1}$$

$$\nu_{CPMG} = \frac{1}{4\tau_{CPMG}} \tag{2.3.2}$$

CT-CPMG is mainly applied on ^{15}N to examine populated states in proteins. The chemical shift and J- coupling affects the transversal magnetization on the nitrogen channel. Consequently, in-phase and antiphase components of the magnetization contribute to the relaxation rate but at different rates. Thus, 2 CPMG train pulses are implemented where one starts with the in-phase, and another one starts with the antiphase ^{15}N magnetization [12]. However, there are two drawbacks. First, the total evolution time has to be short due to the antiphase relaxation. Second, an even number of pulses must be applied on each pulse block to eliminate errors. Hence, 4 echo elements have to be in each CPMG block. The experiment that solves these problems employs a strong ^1H continuous wave field to decouple protons [13]. Despite this, a high power decoupling on the proton channel may cause the heating of a sample with a high salt concentration by dielectric and inductive losses [14]- [15]. The pulse sequence introduced by Yang´s group employs a single train CW-CT-CPMG dispersion [16]. In this work, the off-resonance effects have less impact on the transversal relaxation rate when CPMG pulses are weak. In addition, the first train pulse uses yyx(-x) phase cycling on π pulses while the second train has yy phases.

Methyl groups with ^{13}C labeling are suitable for measuring the dynamics of proteins using the TROSY (Transverse relaxation optimized spectroscopy) experiment [17]. The main challenges are the presence of $13C -^{13} C$ J-coupling and proton-carbon dipolar cross-correlation. It can be overcome by detecting either CH_3 or CHD_2 groups. For the CH_3 group, TROSY CT-CPMG is able to extract a slower decaying relaxation. In this case, REBURP selective pulses are applied for CPMG [18]. The concept of detecting CHD_2 group employs the decoupling of deuterons as a function of ν_{CPMG}. However, it is complicated to select only CHD_2 and suppress CH_3 group. It is desired to use amino acid precursors containing CHD_2 methyl groups.

2.4 Anisotropy of bulk magnetic susceptibility

In solid-state NMR, ^1H line broadening arises from homogeneous (coherent and incoherent) and inhomogeneous effects. Chemical shift dispersion is explained by inhomogeneous broadening. Homogeneous incoherent broadening is a result of relaxation processes. The relaxation is a random time-dependent fluctuation of a local magnetic field resulting in the exponential decay of an NMR signal [5]. The R_2 relaxation rate characterizes the process, and the Lorentzian function describes the peak in the NMR spectrum

$$S(\omega) = S(0)\frac{R_2}{R_2^2 + (\omega - \Omega)} \tag{2.4.1}$$

where S_0 is the signal at zero time, and Ω is a resonant frequency. The linewidth of the signal is proportional to R_2.

Homogeneous coherent broadening has a larger contribution compared to the incoherent term and comes from dipolar interactions of atoms with a high gyromagnetic ratio. Experimental and theoretical results have shown that the proton linewidth is nearly inversely proportional to the product of spinning speed and magnetic field strength [19], [20].

Several factors also contribute to the broadening of linewidth. In particular, it turns out that deuteration has a limited effect on spectral quality [21]. Spinning

angle adjustment contributes by a few Hz [22]. The shim has a contribution less than 1 Hz.

The rest contribution comes from the anisotropy of bulk magnetic susceptibility. (ABMS) [23].In a powder sample, crystallites are inhomogeneously distributed. The magnetic polarization induced by the external magnetic field leads to a broadening of the resonance line. The crystallites behave like magnetic dipoles. Moreover, crystallites, membrane proteins, and fibrils are nonspherical, therefore, one can not suppress ABMS by MAS. Introducing the anisotropic susceptibility tensor χ, the magnetic dipolar moment ($\vec{M}$) can be expressed as

$$\vec{M} = \mu_0^{-1} \chi B V \tag{2.4.2}$$

where V is the volume of a sample. In secular approximation, the Hamiltonian for a spin S and magnetic moment $\vec{M}$ is

$$\widehat{H} = \vec{S}\widehat{D}\vec{M} = (D_{zx}\chi_{xz} + D_{zy}\chi_{yz} + D_{zz}\chi_{xz})\mu_0^{-1} S_z B V \tag{2.4.3}$$

where χ_{ij} are Cartesian coordinates of the susceptibility tensor and $d_{ij} = \frac{\mu_0 \gamma}{4\pi r^3}(\delta_{ij} - 3\vec{r_i}\vec{r_j})$ are equivalent components of dipolar interaction.

However, since the Hamiltonian for the ABMS interaction has the same form as the isotropic chemical shift on the nuclear spin term, the CPMG pulse scheme can suppress ABMS and narrow line widths [24].

Chapter 3

Hydrogen bonds

3.1 The theory of H-bonds

Hydrogen bonds (H-bonds) are responsible for stabilizing the three-dimensional fold of proteins. Several techniques can be used to detect H-bonds, such as X-ray and neutron diffraction. In NMR, the presence of J coupling provides evidence of these bonds. Correlation spectroscopy (COSY) is a type of experiment that identifies donor (N−H) and acceptor (C=O) groups. The overlap of donor and acceptor electronic orbitals determines the size of H-bond scalar coupling [25]. Typical values for ${}^{2h}J$ are between 6-11 Hz [26], while for ${}^{3h}J_{NC'}$, it is usually less than 1-2 Hz [27, 28].

H-bond coupling is mediated via electrons [29]. Four terms contribute to the nuclear spin Hamiltonian for electron-mediated nuclear spin-spin couplings: paramagnetic spin-orbit (PSO), diamagnetic spin-orbit (DSO), spin dipolar, (SD) and Fermi contact (FC).

$$\widehat{H}_{nuclear} = \widehat{H}_{PSO} + \widehat{H}_{DSO} + \widehat{H}_{SD} + \widehat{H}_{FC} \tag{3.1.1}$$

The Fermi contact term is often dominant and accounts for more than 94% of total values for ${}^{2h}J_{NN}$,[1] J_{NH} and ${}^{3h}J_{NC'}$ [1].

[1]The symbol ${}^{nh}J_{AB}$ means the following: one of the n bonds connecting A and B nuclei in the chemical structure is the H-bond

Computed results for ${}^{2h}J_{NN}$ showed an exponential dependence on distance between N atoms for Watson-Crick base pairs [30]. The values are in range from 6 to 8 Hz [31]. The same result is also valid for the imino proton chemical shifts. However, ${}^{1}J_{NH}$ has a different behavior. Particularly, the maximum value reached $\sim 2.8\mathring{A}$, which can be experimentally observed in duplex DNA.

The geometry of the H-bonds has an impact on the ${}^{3h}J_{NC'}$(see figure 3.1). Particularly, theoretical results in formamide dimers demonstrate that the value of long-range J-coupling has an exponential dependence on r_{HO} and reaches its maximum when the angle θ_2 is straight. Angle θ_2 and ρ give a small contribution.

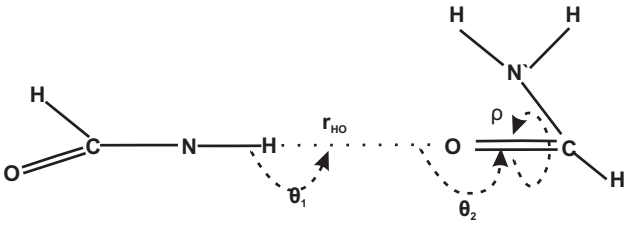

Figure 3.1: *Geometric dependence of* ${}^{3h}J_{NC'}$ *coupling. Three parameters are introduced: H-bond distance* r_{HO}*, internal angles* θ_1*,* θ_2 *and angle* ρ *measured around* C=O *bond. Adapted from [31].*

Density Functional Theory (DFT) does not help to find out which electronic wavefunctions are responsible for magnetization transfer. Therefore, molecular orbital (MO) needs to be used. In this model [32], the FC contribution to the J-coupling constant is given by

$$J_{AB} = \frac{16}{9} h\mu_e^2 \gamma_A \gamma_B \langle a|\delta_A|a\rangle \ \langle b|\delta_B|b\rangle \, \pi_{ab} \tag{3.1.2}$$

where μ_e is a Bohr magneton, a,b are atomic/hybrid orbitals centered on A and B, π_{ab} is an atom-atom polarizability. The expression for the π_{ab} is the following

$$\pi_{ab} = 4 \sum_{i,occ} \sum_{j,unocc} \frac{c_{ia} c_{ib} c_{ja} c_{jb}}{\varepsilon_i - \varepsilon_j} \tag{3.1.3}$$

where the terms in the numerator refer to the coefficients of orbitals in occupied and

unoccupied MO and ε_i,ε_j are energies. The consequence is that FC contribution to the nuclear coupling correlates to the orbital coefficients and energies. However, to get explicit expressions for 3.1.2, it is convenient to introduce an NHN′ model. The model is represented by 2 sp^2 orbitals and 1s orbital on hydrogen (see figure 3.2). The resonance integrals β,β' and β'' describe the interaction between orbitals.

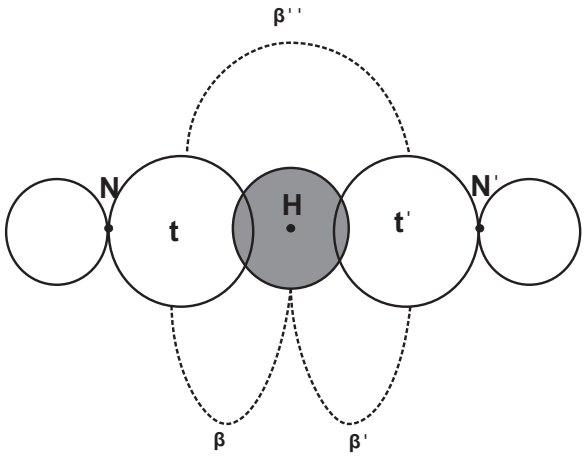

Figure 3.2: *NHN′ model of nuclear spin-spin coupling. The hybrid orbital t centered on N is directed toward the 1s atomic orbital h on H, and t′ denotes a hybrid orbital on N′. β, β' and β'' are resonance integrals associated with different pairs of orbitals. Adapted from [31].*

The atom-atom polarizabilities for 3 types of J-couplings ($^{2h}J_{NN'}$,$^{1h}J_{NH}$,$^{1h}J_{HN'}$), respectively, have the following form

$$\begin{aligned} \pi_{tt'} &= -\frac{\beta^2\beta'^2}{2r^3(\beta^2+\beta'^2}\left(3+\frac{(\alpha_h-\alpha_t)^2}{\beta^2+\beta'^2}\right) \\ \pi_{th} &= \frac{\beta^2}{2r^3} \\ \pi_{ht'} &= \frac{\beta'^2}{2r^3} \end{aligned} \tag{3.1.4}$$

with $r = \sqrt{\beta'^2+\beta^2+\frac{(\alpha_h-\alpha_t)^2}{4}}$ and α_h and α_t as Coulomb integrals. These expressions have 2 main outcomes. First, H-bond scalar couplings have an exponential dependence. Second, the polarization is symmetric with respect to the nitrogen donor and acceptor atoms.

It is also worth to mention the effect of ${}^1H/{}^2H$ exchange of H-bond scalar coupling. The lower zero-point vibrational energy of deuterated compounds and the anharmonicities of bond potentials lead to a shortening of covalent D−X bonds on the order of few hundredths of an Angstrom [33]. The shortening of covalent bond is accompanied by a change of donor-acceptor distance. Studies have shown the reduction of H-bond ${}^{2h}J_{NN}$ in selectively labeled double-stranded DNA after H_2O/D_2O solvent exchange by 0.3-0.4 Hz [34]. Additionally, the deutaration of protein backbone h-bonds showed a decrease of ${}^{3h}J_{NC'}$ coupling by 0.03±0.03 Hz [35]. As a consequence, the deuteration of all H-bonds in a protein should lead to the change in the total internal energy and is expected to contribute to the destabilization in D_2O [36].

3.2 Experimental observations of H-bonds

The following section is devoted to the literature overview that covers some experiments which were implemented for the characterization of H-bonds in solution and solid-state NMR.

3.2.1 Detection of hydrogen bonds ${}^{3h}J_{NC'}$ scalar couplings

Direct detection of H-bonds can be established via HNCO (see figure 3.3) experiment with a significant dephasing time [27, 37].

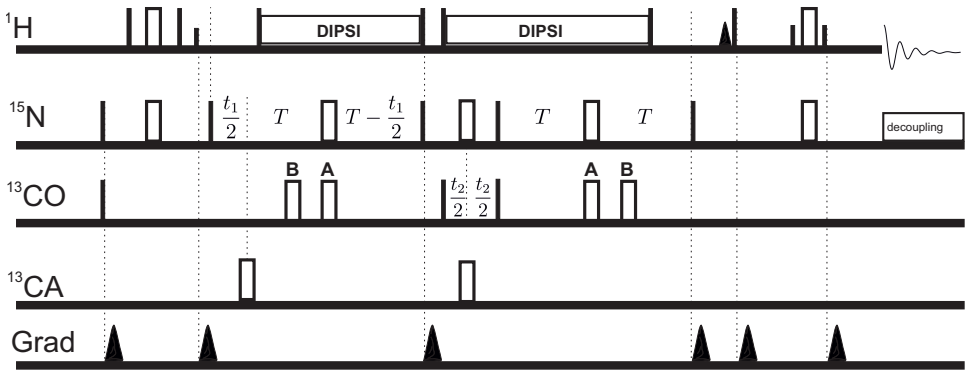

Figure 3.3: *HNCO INEPT-based conventional scheme. DIPSI refers to the proton decoupling. A refers to the centered π pulse on nitrogen and carbon channels for long-range ${}^{3h}J_{NC'}$ experiment. B refers to the ${}^{1h}J_{NC'}$ reference experiment with a shift of 16.5 msec. Adapted from [27].*

In a classical HNCO experiment, the dephasing time 2T from N_x to $2N_yC'_z$ magnetization is usually shorter than $\frac{1}{(2*{}^{1h}J_{NC'})}$ (about 33 msec). In contrast to this, the long-range experiment is carried out with a total time of $\frac{2}{({}^{1h}J_{NC'})} \approx 132$ msec. In this case, the one bond transfer from the in-phase operator to the anti-phase operator is refocussed. Results in [27] were presented for ${}^{15}N -{}^{13}C$ enriched Human ubiquitin. The experiment lasted 12 hours, and 31 backbone H-bonds were observed. A second reference experiment with a shift π pulse on carbon (B in figure 3.3) serves for the determination of long-range coupling. Experimental results for ${}^{3h}J_{NC'}$ were in a range between 0.24 and 0.9 Hz. The largest coupling was found in β-sheet conformations (average value of 0.65 Hz), and ${}^{3h}J_{NC'}$ values in α-helical structures had a mean value of 0.38 Hz.

3.2.2 Detection of CH/π interaction in proteins

XH/π interactions refer to the H-bond interactions where the sp^2-hybridized covalent bond acts as an acceptor [38]. If X is a carbon atom, the interaction is dispersive and equivalent to the H-bond. In proteins, the high concentration of methyl and aromatic groups is present in the hydrophobic cores, which makes methyl/π interaction significant for functionality. The research in paper [38] was devoted to the identification of the geometric relation between the methyl group and aromatic ring and, subsequently, analyze weak scalar coupling. Three parameters were used for

the study: distance between the donor carbon and the center of the acceptor ring; ϕ_1 angle between the ring normal and a vector connecting methyl carbon and the center of the ring; ϕ_2 angle between C−H and ring center-H vectors (see figure 3.4). The model consisting of toluene and ethane showed that the J-coupling ($^{h\pi}J_{CMeCaro}$) has an exponential dependence on distance. As for the angle, the $^{h\pi}J_{CMeCaro}$ is equal for all carbons in the aromatic ring when the donor methyl group is above the ring ($\phi_1 = 0$). When ϕ_1 increases, coupling demonstrates a different behavior for different atoms and increases for nuclei that are above the methyl group. The angle ϕ_2 has a small effect on the coupling.

Long-range HCC NMR experiment (see figure 3.4 **(b)**) of triple labeled ubiquitin has shown cross peaks originating from Meπ interactions. At -0.2 ppm, the chemical shift of L50-δ_2 protons, two correlations have been observed in the aromatic region of the carbon spectrum, and the peaks were assigned to C_{δ_1/δ_2} and $C_{\epsilon_1/\epsilon_2}$ nuclei of Y57. Furthermore, the cross peak was observed between the L67 δ_2 methyl group and F45 C_{δ_1/δ_2} nuclei. The presented results show that one can detect $^{h\pi}J_{CMeCaro}$ up to 0.1 Hz.

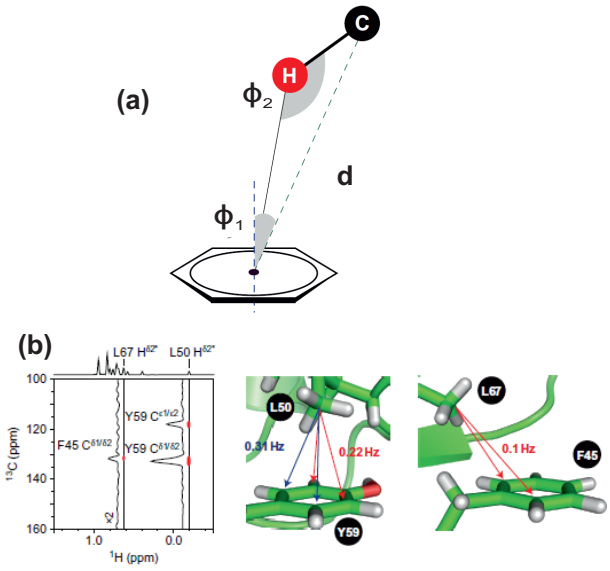

Figure 3.4: ***(a)*** *Schematic representation of Meπ interaction.* ***(b)*** *Long-range 2D HCC spectrum of triple labeled ubiquitin (left) with cross peaks between L50 and Y59 (center) and L67 and F45 (right). Figure from [38].*

3.2.3 Measurement of H-bonds in solid-state NMR

J-based correlation spectroscopy has also been demonstrated in solids [39, 40]. The sensitivity of experiments is a big challenge here due to the small value of ${}^{3h}J_{NC'}$ and ${}^{2h}J_{NN}$ and the presence of secular anisotropic interactions that result in a transverse dephasing. Typical solutions imply the application of a high spinning speed and an extensive deuteration of a sample [41]. One of the first papers that demonstrated the presence of H-bonds in solid-state NMR was published by P. Schanda [42]. INEPT-based HNCO experiment [27] was implemented for a triple-labeled ubiquitin. The crucial part of the experiment was the N$-$C$'$ correlation with a total duration of 66 msec for the coherence transfer from ${}^{15}N$ donor to ${}^{13}C'$ acceptor. Another feature of this experiment was the sensitivity. As the size of coupling for 4 cross peaks was less than 1 Hz, it required to do multiple 3D experiments with a total acquisition time of 112 hours. Furthermore, the results were surprising as only seven H-bond correlations have been observed out of 31 as it has been measured in solution-state NMR [27].

Chapter 4

Human islet amyloid polypeptide

Nowadays, more than 50 diseases are associated with the self-assembly of proteins into amyloid fibrils [43, 44]: Alzheimer's disease, type 2 diabetes, Parkinson's disease, and others. Human islet amyloid polypeptide (hIAPP) is a 37-residue hormone that is cosecrected with insulin. The protein is involved in blood sugar regulation and preventing gastrit emptying. HIAPP self-associates in amyloid fibrils and is considered the main part of amyloid deposit typical for T2D disease which affects more than 300 million people. It is assumed that pancreatic islet amyloidosis contributes to the progression of T2D, β-cell loss. Hiapp and β-amyloid polypeptides were found in brain plaques in Alzheimer's disease.

4.1 Structure, expression, and regulation of IAPP

IAPP belongs to the group of calcitonin-like peptide hormones, which also include calcitonin, calcitonin gene-related peptide, and adrenomedulin [45, 46]. The IAPP gene is located on the short arm of chromosome 12 in human DNA [47]. Pancreatic β- cells transcribe the peptide (pre-pro hIAPP) containing 3 exons and 2 introns [48]. The signal peptide from the pre-pro IAPP, which controls the protein secretion and translocation in living organisms, consists of 89 amino acids and generates 67-amino acid long pro-IAPP. The protein disulfide isomerase enzyme enables the formation of a disulfide bond between residues 2 and 7 (C2 and C7, respectively), which is responsible for the catalysis of protein folding, defining the three-dimensional structure. Then pro-IAPP is involved in subsequent post-translational modifications of proteases which serve for cleaving polypeptide bonds by hydrolysis. Eleven residues from N-terminal and 16 residues from C-terminal are removed by prohormone con-

vertase and prohormone convertase $\frac{1}{3}$ proteases, respectively. The third protease, carboxypeptidase, removes lysine and arginine amino acids from the C-terminal, exposes residue number 38 (glycine), and amidation of residue number 38 (tyrosine) takes place. The final form of the hormone, the mature form, contains 37 amino acids with one disulfide bond between residues 2 and 7 and an amidated C-terminus [49, 50].

A comparison of amino acid sequences confirmed that proline residues 25,28, and 29 in rat and mouse iapp prevent it from misfolding and aggregation [51]. As a consequence, mature IAPP is monomeric in rodents. Hence, IAPP aggregation has been peformed in transgenic mice overexpressing hIAPP [52]. In case of a fat diet, several symptoms are developed, including hyperglycemia, glucose intolerance, and pancreatic β-cell mass [52].

Glucose acts as a regulator of expression for both IAPP and insulin [53]. Subsequently, these genes share similar sequence elements in the promoter region. However, certain differences are present as well. For example, the pancreatic and duodenal homeobox 1 gene is sufficient for promoting insulin promoter activity [54], while the IAPP promoter requires Ca^{2+} signaling to be activated [53]. Furthermore, studies demonstrated a higher IAPP secretion from β-cell of diabetic rats compared to insulin under the influence of dexamethasone [55]. Other studies have shown that the IAPP gene is regulated independently from the insulin gene [56].

IAPP crosses the blood-brain barrier to reach its binding sites in the central nervous system, activates receptors that suppress glucagon release from the pancreas, and regulates gastric emptying [57, 58]. It implies that hIAPP and insulin both keep blood sugar under control by suppressing the endogenous glucose production in the liver [59]. Several studies demonstrated the role of IAPP in the spread of pancreatic β-cells [60], in controlling body weight and energy balance [61], and in significant weight reduction effects. Therefore, IAPP analogs have been considered as a treatment against obesity [62].

4.2 The structure of hIAPP

The aggregation process for hIAPP consists of three steps: the lag phase, represented by monomers; the elongation phase, characterized by the formation of protofibrils and the elongation; and the saturation phase, where fibrils are matured [63]. Since the aggregation kinetics of IAPP have a short lag time [64], the aggregation process follows nucleation-polymerization-mechanism. In other words, a small nucleus induces the growth of an oligomer and eventually results in the formation of mature fibrils [65]. The accumulation and formation processes of the aggregates are associated with the death of the pancreatic β-cells.

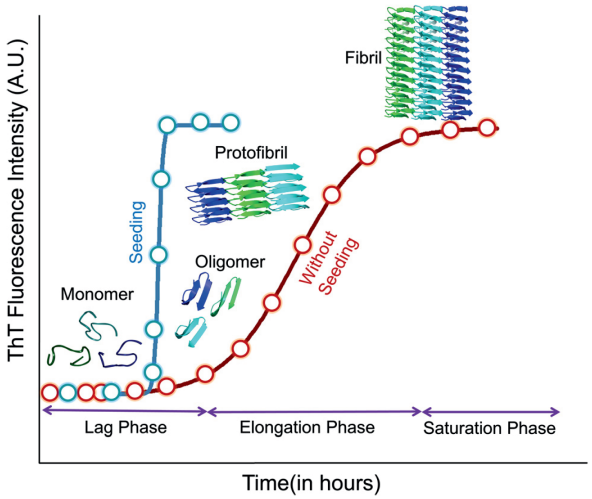

Figure 4.1: *Aggregation kinetics of hIAPP. The blue curve refers to the faster aggregation due to the presence of seeding. The red curve corresponds to the non-seeded aggregation. Figure from [46].*

Since hIAPP undergoes several modifications during aggregation processes, it is crucial to analyze structural changes in peptides during the fibrillation pathway to understand the elements which initiate the start of type 2 diabetes. It can be performed using a combination of techniques such as NMR, circular dichroism, and Fourier transform infrared spectroscopies [50, 66]. Early results have evidenced the presence of a random coil structure in monomeric hIAPP [67]. Subsequent studies have shown that the partial helical conformation is observed in monomeric hIAPP,

which adopts β-sheet to form mature fibrils [68, 69]. ThioflavinT fluorescence, a universal marker for amyloid fibril investigations, manages to monitor structural transitions in hIAPP. Diffraction studies have shown that well-defined form β-strand aggregates are parallel to each other, resulting in a cross-β-sheet conformation [70]. This arrangement leads to the formation of twisted ribbon-like fibrils of amyloid deposits [71]. The morphology and relative density of fibrils can be quantified using the combination of multiple techniques, such as atomic force microscopy (AFM), transmission electron microscope (TEM), and others [72]. However, these methods provide only the macroscopic structural information. To have an insight into atomic level information, it is possible to use NMR spectroscopy.

Solid-state NMR is useful for obtaining the structural at the atomic level since it does not require solubility or crystalline order in the samples. In other words, fibrils can be studied in their nature form. Rotational resonance and isotropic-edited FTIR experiments showed that hIAPP fibrils contained a more compact, highly pleated structure. To prove this, 10 amino acid peptide long segment of hIAPP (residues 20-29) were analyzed [73]. Additionally, the same sequence part was solved using $^{13}C-^{15}N$ uniformly labeled segment (residues 22-27) by 2D dipolar assisted rotational resonance (DARR) [74]. The authors came to a conclusion that "the fibrillation core segment pack as an antiparallel ladder in hetero zipper class with hydrophobic interaction between side chains of F23 and L27 in a parallel, and F23 and I26 in an anti-parallel fashion" [74]. Further research results confirmed that the β-sheet in the central region (residues 23-28) is vital for amyloid formation.

In this thesis, the aim was to quantify N- and C-terminals of hIAPP protein. The unpublished results from the group of prof. Reif revealed that CP-based experiments enable to observe rigid parts of this protein. That means that the dipolar coupling is not averaged out. From another side, Cryo-EM have not provided any information about N-terminal part [75]. To deal with this problem, one can implement REDOR method to determine order parameter of the residues. The results will be presented in chapter 7.

Chapter 5

T_2 CPMG experiments

The results of the CPMG pulse scheme applied for the T_2 experiment are presented in this chapter. The pulse scheme of the experiment is shown in figure 5.1. The experiment starts with the excitation on the proton channel by applying a hard $\frac{\pi}{2}$ pulse (1.4 usec). Then, the cross-polarization starts from proton to nitrogen atoms using the HH condition. The CP consists of 2 shaped pulses: ramp40100.100 (proton) and square.100 (nitrogen). The duration of CP pulse is 800 usec. The next part is a t_1 evolution in the indirect dimension with a proton decoupling. After a t_1 evolution, a CT-CPMG starts with a fixed total evolution time and pulses on nitrogen. The water suppression was achieved using MISSISSIPPI. The relaxation delay was set to 3 sec. The number of scans was set to 16.

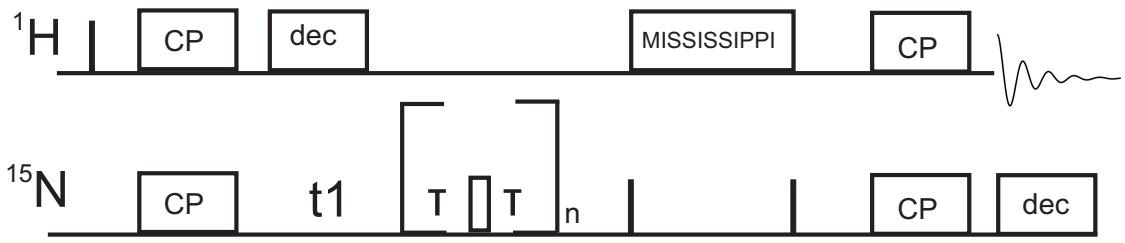

Figure 5.1: *Pulse scheme for T_2 CPMG experiment. For CP ramp40.100 and square.100 shaped pulses were used with a duration of 800 usec. Water suppresion was achieved using MISSISSIPPI. Sltppm and Waltz decoupling schemes were employed at 15 kHz in direct and indirect dimensions, respectively.*

The aim was to demonstrate the sensitivity increase using a triple labeled (^{2}H,

^{15}N, ^{13}C) 20% back exchanged and fully back exchanged with 100% H_2O SH3 proteins. The spinning speed was set to 55 kHz for the 1.3 mm rotor. All measurements were performed on a 500 MHz Bruker spectrometer setting the temperature at 230 K with 1100 l/h-1300 l/h gas flow. The actual calibrated temperature was 290 K. T_2 CPMG experiments were performed at different evolution times (2T): 40 msec, 60 msec and 120 msec.

Figure 5.2 shows the results of the T_2 CPMG experiment with 40 msec evolution time. The y-axis depicts the ratio between measured and reference intensities for assigned residues. According to the results, the ratio tends to increase with the CPMG frequency. For the analysis, it is required to quantify a gain for each specific residue. The expression for the transverse magnetization (or, intensity) as a function of time t is given by

$$I(t) = I_0 \exp^{\frac{-t}{T_2}} \tag{5.0.1}$$

where I_0 is the reference intensity without CPMG block, $I(t)$ is the intensity at time t ($2T = 2 * n * \tau$), T_2 is relaxation time, n is the number of CPMG blocks, 2*τ is the delay between two π pulses. If one substitutes the time with the $\nu_{CPMG} = \frac{1}{4\tau}$, then expression becomes

$$I(\nu_{CPMG}) = I_0 \exp^{\frac{-n}{2\nu_{CPMG}T_2}} \tag{5.0.2}$$

The problem is that the function (5.0.2) is not continuous since it has uncertainty at $\nu_{CPMG} = 0$. However, since $1 - \exp^{-x}$ and $\exp^{-1/x}$ do behave similarly and the intensity ratio tends to saturate , one can transform the expression, such as

$$I = p - a * \exp^{\frac{-\nu_{CPMG}}{b}}; \quad b = \nu_{CPMG} \ln\left(\frac{a}{p - \exp^{\frac{-n}{2\nu_{CPMG}T_2}}}\right) \tag{5.0.3}$$

where parameter 1-a shows a gain of an intensity ratio as a function of frequency. Parameter b is an "effective" CPMG field that characterizes the rate of intensity saturation. If the parameter b is small, the function grows slowly, and vice versa. Parameter p is the ratio between I_{CPMG} at very high ν_{CPMG} (infinitely large) and the reference intensity (without evolution time). In the case of 40 msec evolution

time, the p was set to 1, therefore, the expression is

$$I = 1 - a * \exp^{\frac{-\nu_{CPMG}}{b}} \tag{5.0.4}$$

The equation in (5.0.3) has the following meaning: single refocussed T_2 experiment has a low intensity value. When the number of spin echo blocks increases (i.e ν_{CPMG} increases), then the intensity ratio increases as well up to the limited value. This limit is called the saturation level and the intensity ratio can not be increased beyond this limit.

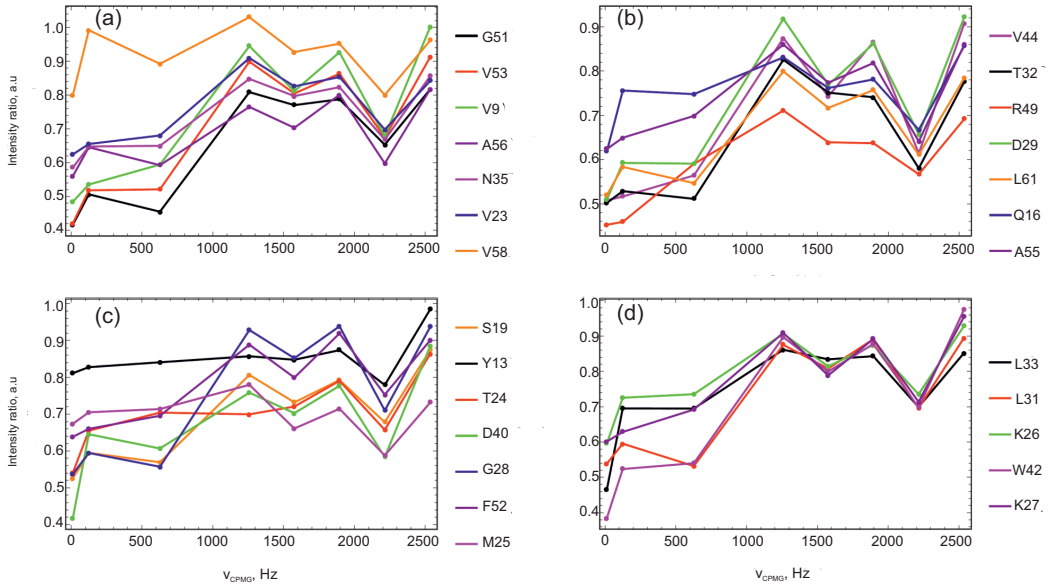

Figure 5.2: *Results for T_2 CPMG experiment for 40 msec evolution time. In this experiment, hard π pulses were used for CPMG trains (5.56 usec at -20dB). The ν_{CPMG} varied from 4 to 2500 Hz. The resulting curves were normalized by dividing the intensity value of the reference experiment (without CPMG) for each residue.*

Experimentally it has been found that it is necessary to use soft π pulses (see figure 5.3) on ^{15}N. Application of hard pulses results in random intensities, which does not improve by changing the MAS frequency. The problem is that the curves for residues in figure 5.2 are not smooth and have dips at certain ν_{CPMG} values which contradicts to the idea that the intensity ratio has to grow monotonous.

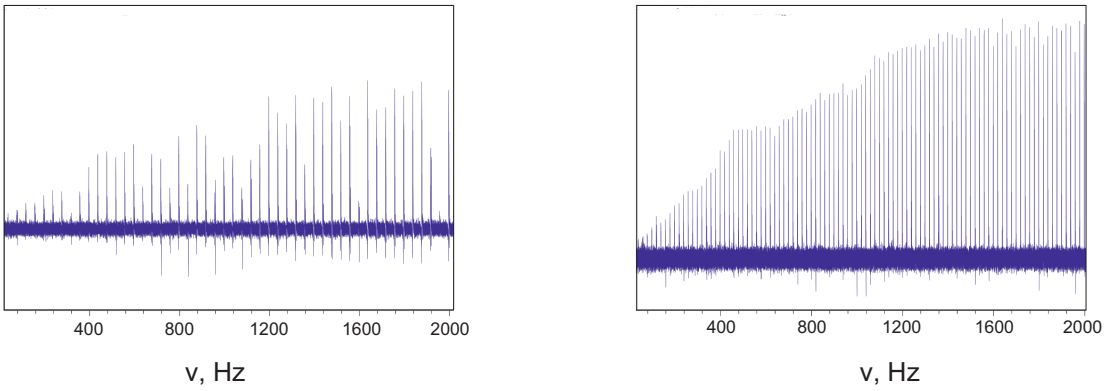

Figure 5.3: *A comparison of hard (left) and soft (right) pulses as a function of* ν_{CPMG} *for 40 msec (hard) and 60 msec (soft), respectively. In particular, there are dips of intensities for hard pulses. These minima are mostly random and not dependent on the rotor period. However, for soft pulses, the intensity curve demonstrates monotonous growth.*

Figure 5.4 shows the results for relaxation rates as a function of CPMG frequency. The expression for R_2 (see equation 2.3.1) is the following:

$$R_2 = -(\frac{1}{2T})ln(\frac{I_{CPMG}}{I_0}) \tag{5.0.5}$$

where 2T is the total evolution time (see figure 5.1), I_0 is a reference intensity recorded without evolution time, and I_{CPMG} is the intensity at a certain CPMG field.

Figure 5.5 describes a relative gain of signal for assigned residues. The gain has been calculated from the expression (5.0.1) and was defined as a ratio between a saturated state where there is no more signal increase (it corresponded to 1) and a starting point (1-a). The intensity is in arbitrary units since it is normalized by the reference experiment (without CPMG evolution time). According to the results, the gain ranges from 1.2 to 2.6.

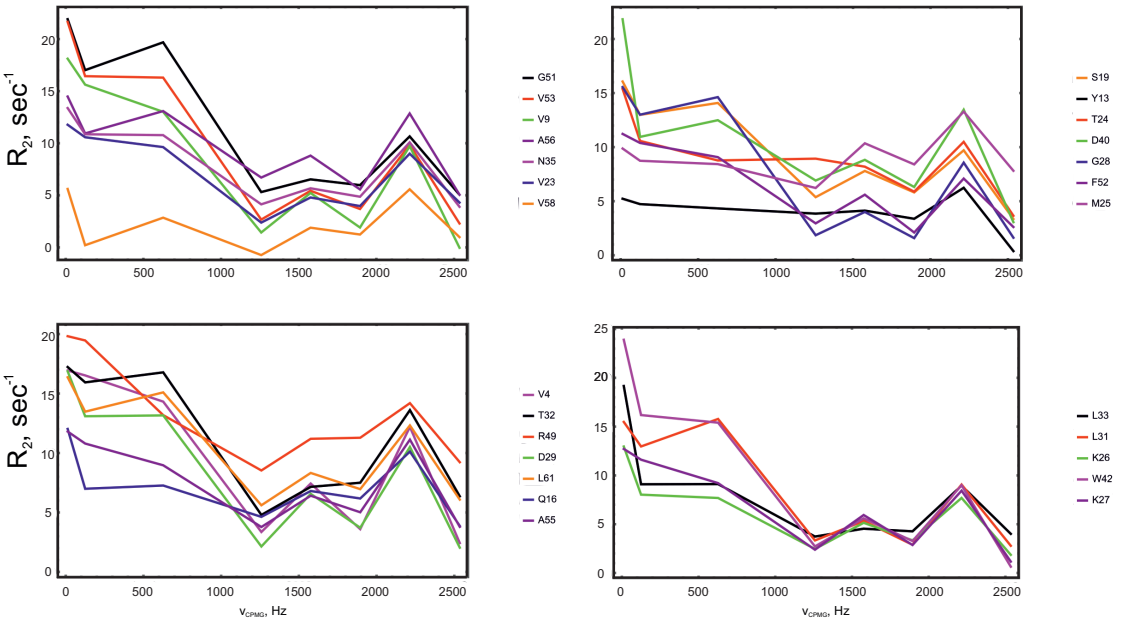

Figure 5.4: *R_2 as a function of ν_{CPMG} for 40 msec experiment. The nonmonotonous behavior of curves is due to the hard π pulses.*

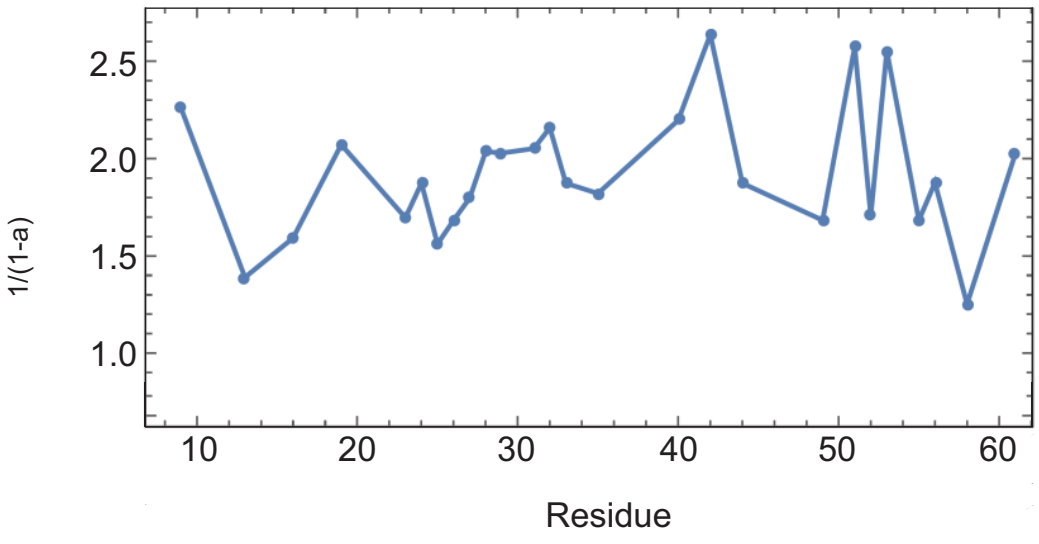

Figure 5.5: *Calculation of a gain for residues. The gain varies between 1.2 and 2.6.*

Figure 5.6 depicts 1D spectra of conventional (single spin echo) and CPMG experiments. In this case, the red curve refers to the $\nu_{CPMG} = 2000$ Hz corresponding to 200 loops in CPMG pulse trains. Based on this comparison, it is becoming evident that the gain for 40 msec evolution time experiment is less than 2.5.

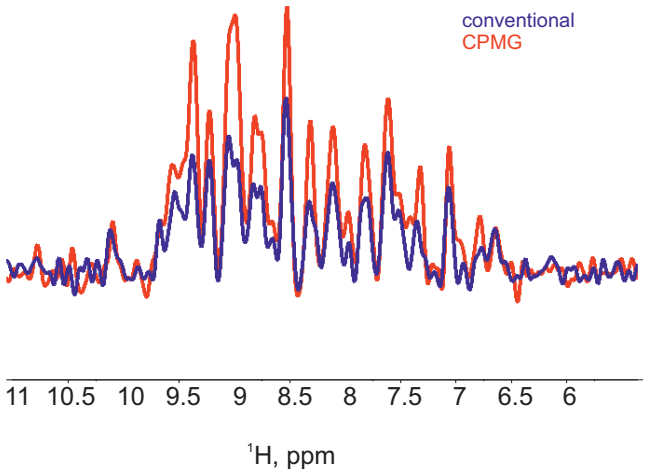

Figure 5.6: *1D spectra for conventional (blue) and CPMG (red) experiments for 2T= 40msec. ν_{CPMG}=2 kHz, which is equivalent to 200 loops. Both experiments were performed at 16 scans and relaxation rate=3 sec.*

Experimental results have shown an increase in a signal for CT-CPMG at 40 msec. To confirm that CPMG works for other CT values, two sets of experiments were performed at 60 and 120 msec. Figure 5.7 illustrates the results for 60 msec CT-CPMG. Here, soft pulses were used in spin echo blocks. Consequently, the normalized intensity curve is smoother than for the 40 msec case. Moreover, the saturation of curves was reached at 0.4. This makes it different from the previous experiment. Therefore, the intensity curve has a different saturation level. It implies a different value of parameter p for expression (5.0.1). Since the saturation was reached around 0.4, one can consider this value as a starting value for the fit. To illustrate the accuracy of the fit parameter, a fit function for residue G28 is shown in figure 5.8.

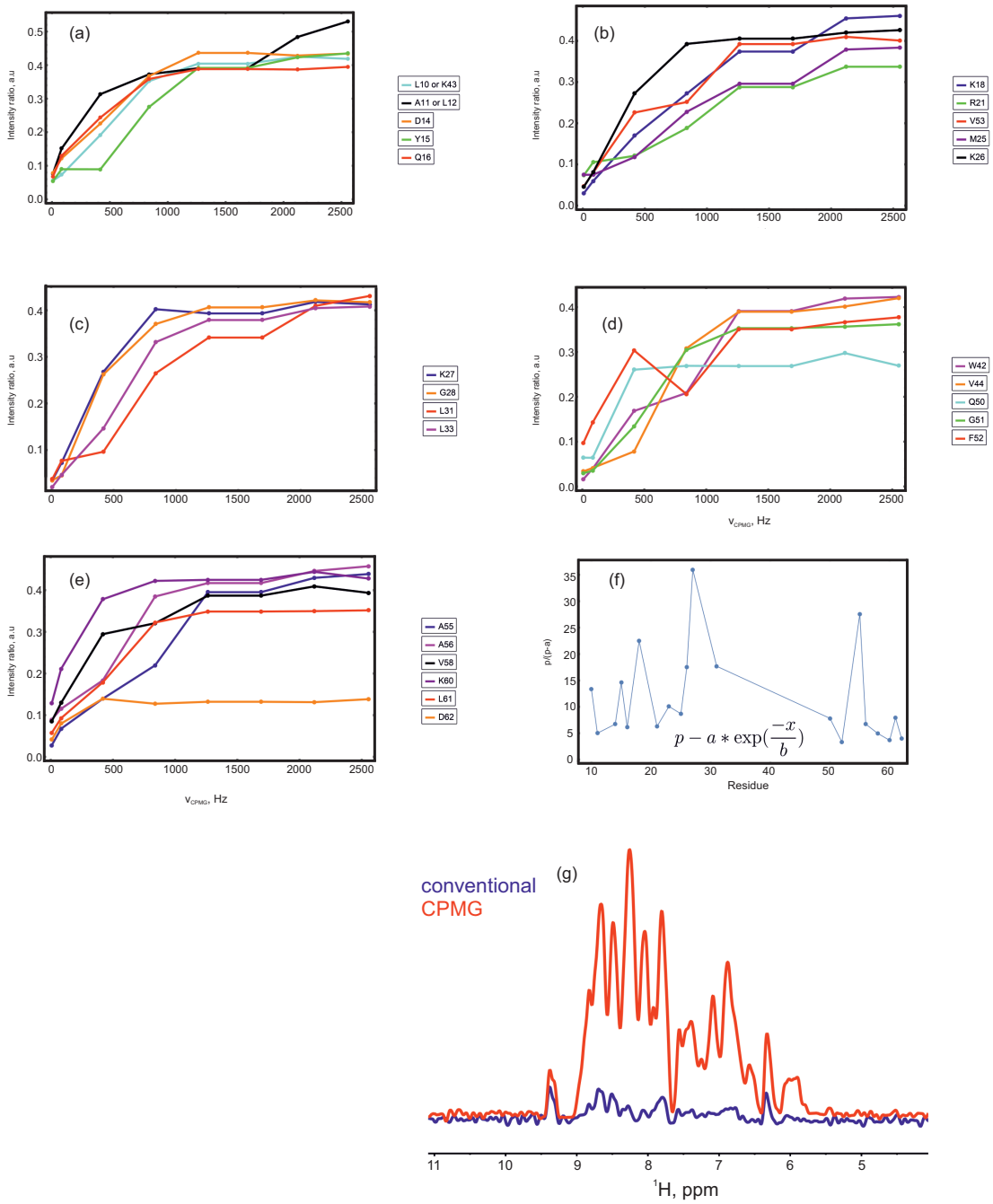

Figure 5.7: *T_2 CPMG experiment for 2T=60 msec. Compared to the 40 msec experiment, soft π pulses (80 usec) are used here. Consequently, the intensity curves look smoother than in the previous experiment (a-e). In addition, the gain is larger due to the T_2 relaxation, which becomes more significant at larger evolution times (f). 1D spectra are also shown in (g).*

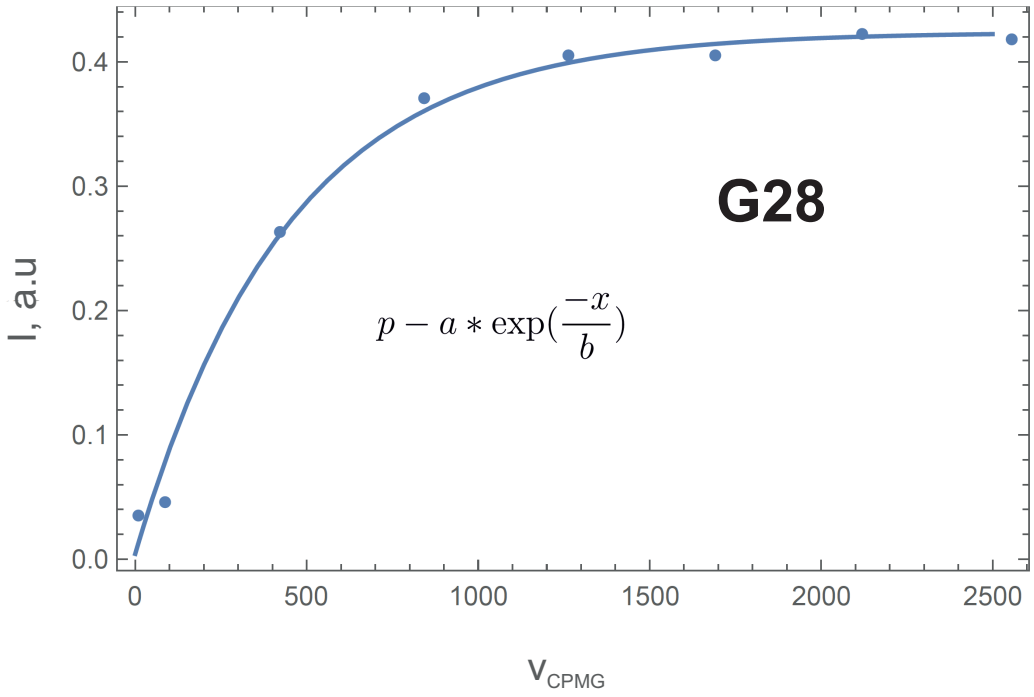

Figure 5.8: *The fit function for residue G28. Three parameters (p,a and b) are used for the simulation. The fitted curve is in good agreement with the theoretical results. The experiment was done at 2T=60 msec.*

CT-CPMG experiment for 120 msec is shown in figures 5.9 and 5.10. As the evolution is more than 100 msec, it is expected to see no signal in the standard spin echo experiment (red figure 5.9) due to the fast T_2' decay. In a conventional case corresponding to $\nu_{CPMG} = 4$ Hz, five residues are visible in HN plane. With an increase in the CPMG field the number of visible increases, and all possible assigned residues become visible at $\nu_{CPMG} = 1400$ Hz (figure 5.10).

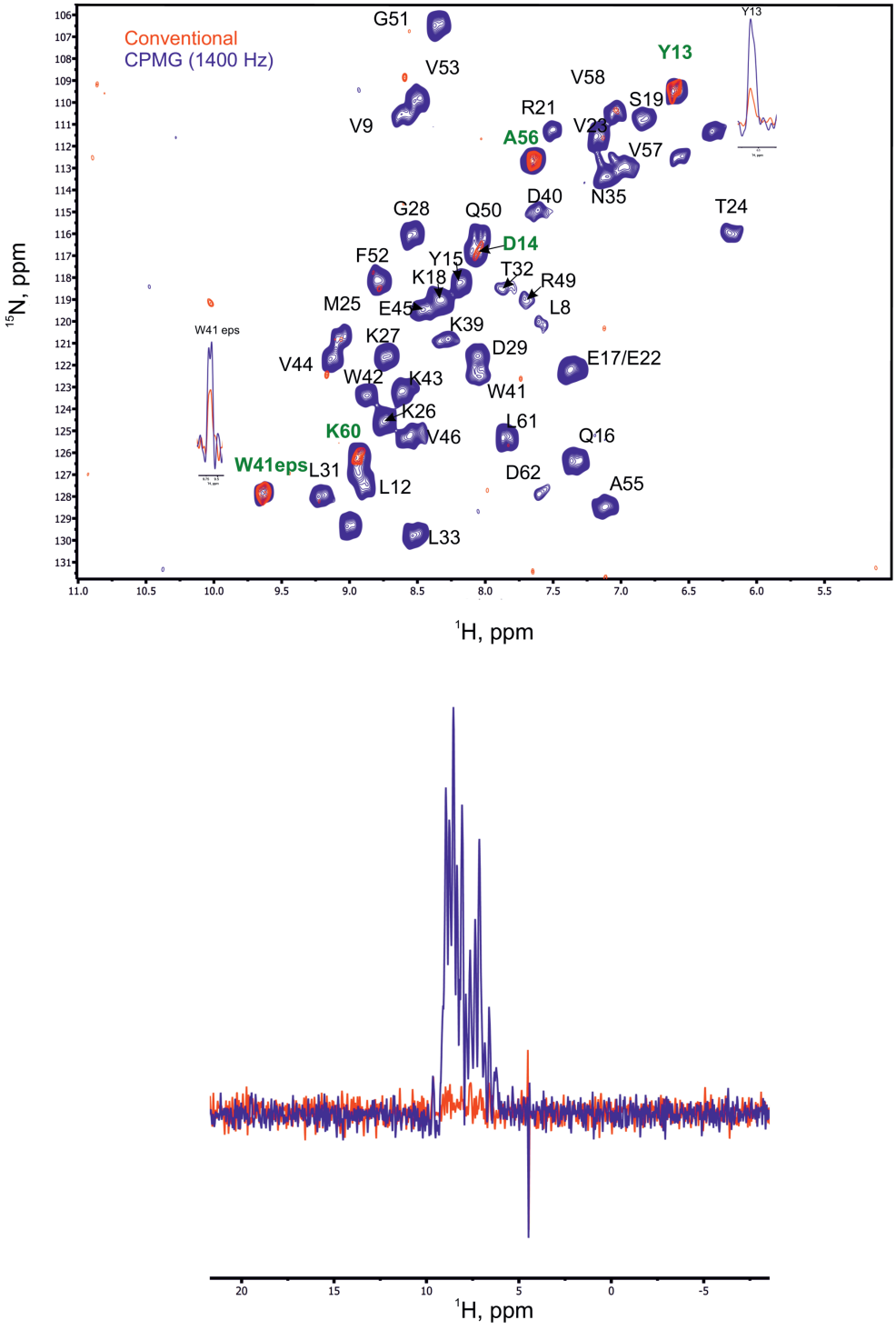

Figure 5.9: *T_2 CPMG experiment for 2T=120 msec. Since T_2' relaxation decays too fast, only 5 peaks are visible in a single spin echo case. In contrast, the CPMG experiment has a larger signal (see figure bottom). Therefore, all peaks can be assigned.*

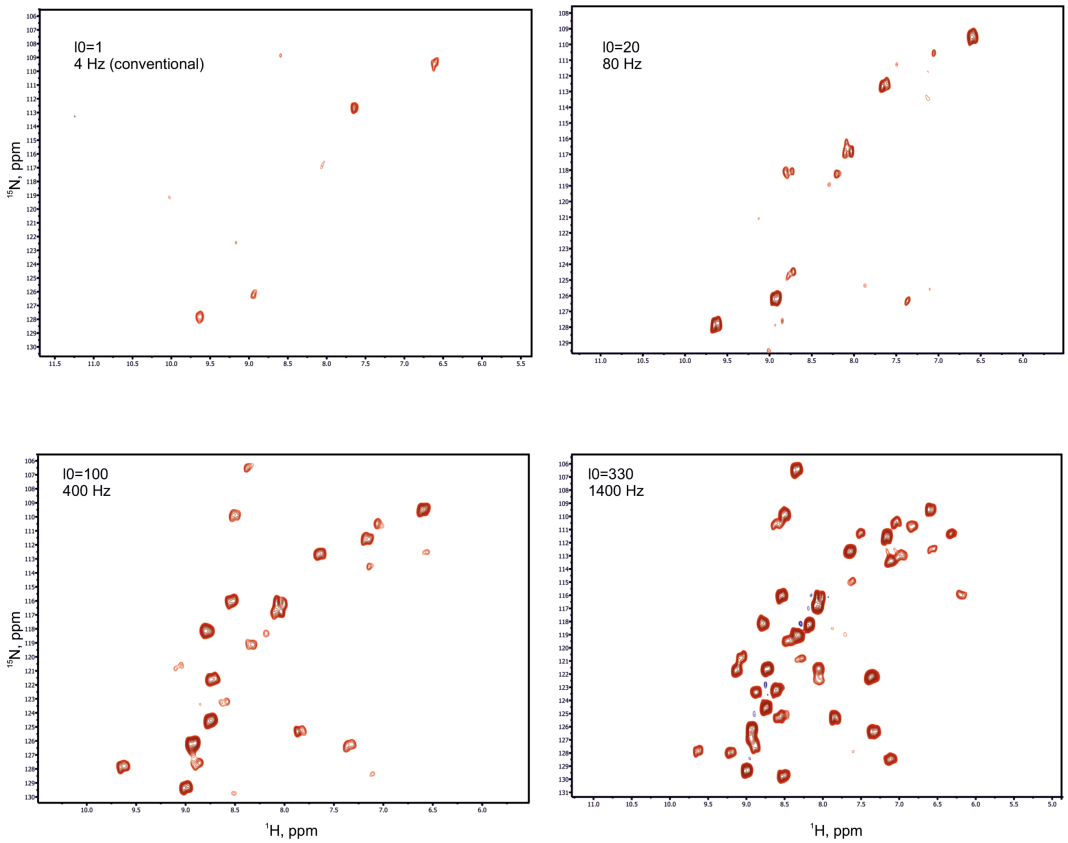

Figure 5.10: *T_2 CPMG for 2T=120 msec. The quality of NH spectra as a function of ν_{CPMG}.*

There is a problem which has not been discussed so far: how does the ^{1}H decoupling affect the sensitivity of a signal during CPMG. To answer this question, test experiments were done (see figure 5.11). In particular, two types of decoupling were tested: sltppm (as it has been mainly used for HNH type of experiments) and DIPSI (this decoupling is used for HNCO experiments, see [31]). According to the results, both decoupling schemes do not give a gain of a signal. Moreover, there is a decrease of a signal at high ν_{CPMG}. It is also essential to note that the DIPSI was set at low power (2.6 kHz), which is mainly done during HNCO experiments (which will be discussed in the next section)

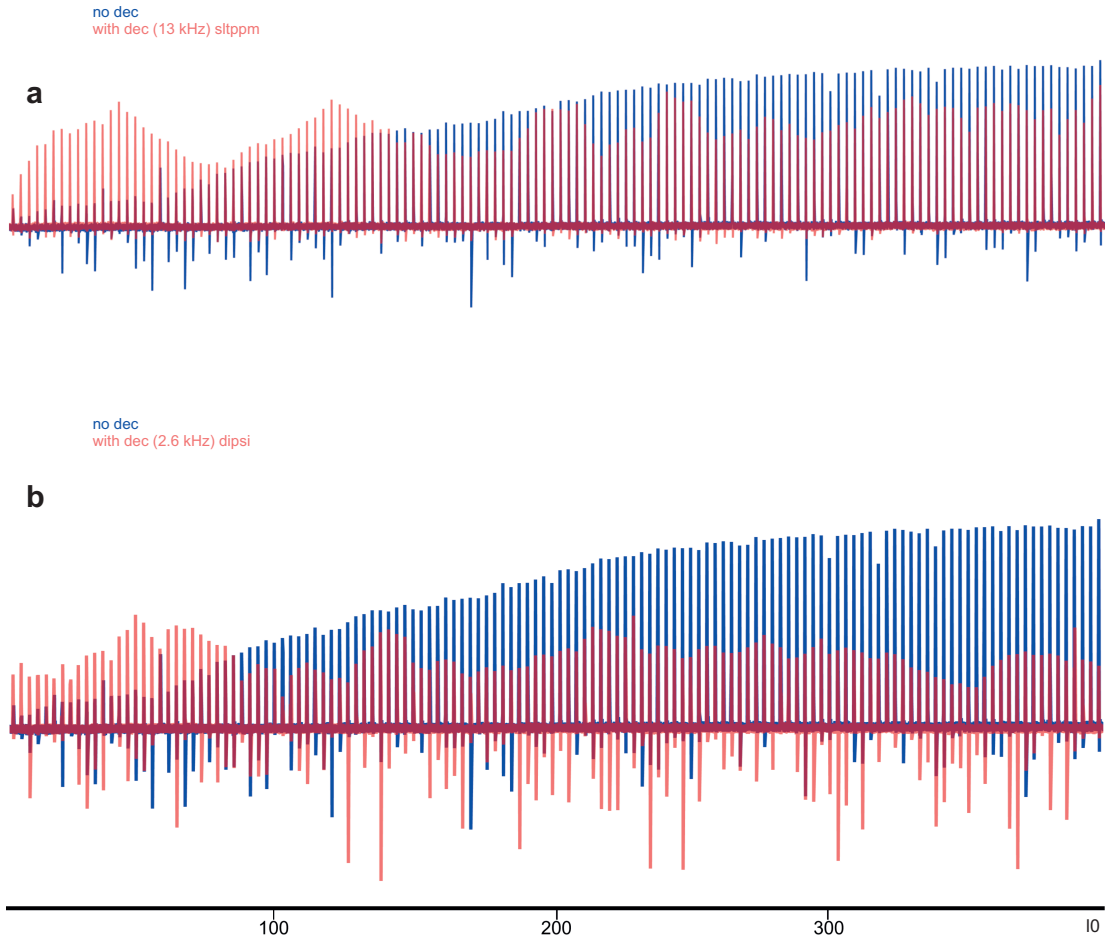

Figure 5.11: *An effect of decoupling on signal sensitivity. The experiment was done for 2T=96 msec using two different decoupling schemes: sltppm (a) and DIPSI (b) at 13kHz and 2.6 kHz, respectively. Based on the results, it is possible to see that decoupling hinders the increase in intensity's signal as it remains constant. In non-decoupling case, the bulk signal increases up to 3 times.*

Chapter 6

HNCO CPMG experiments

The content of this chapter is divided into two parts: the first part is related to the sensitivity improvement for the HNCO experiment and the second part discusses the detection of H-bonds.

6.1 Sensitivity Enhancement of HNCO Experiments by applying CPMG-like pulse schemes

The pulse scheme for the HNCO CPMG experiment is shown in figure 6.1. Similar to the experiment of Paul Schanda [42], this experiment is INEPT-based. INEPT blocks contain hard pulses for ^1H (1.4 usec for $\pi/2$ pulse) and ^{15}N (2.78 usec for $\pi/2$ pulse). Shaped pulses are represented by Gaussian pulse cascades G4 and Q5 (for excitation $\pi/2$ pulses) and Q3 (refocussing π pulses) with a duration of 200 usec. The water suppression was achieved using MISSISSIPPI.

The presented pulse scheme has two main differences compared to the standard HNCO experiments. First, compared to the experiments in [27, 39, 42], the continuous wave decoupling is substituted by π pulse on the ^{1}H channel centered during t_1 evolution. The reason is that the decoupling hinders the signal intensity increase with the increased ν_{CPMG}. Second, t_2 occurs after NC$'$ correlation. Since it is not trivial to implement the CPMG pulse scheme during CT evolution, the evolution in the ^{15}N dimension occurs after the CPMG block.

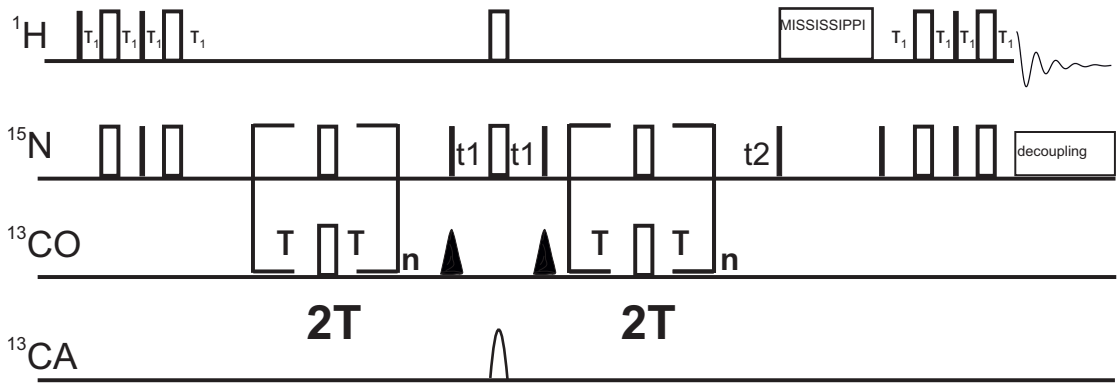

Figure 6.1: *HNCO CPMG INEPT-based pulse scheme. The delays in the INEPT block were set to 2.7 msec. Filled rectangular pulses refer to $\pi/2$ pulses (shaped and hard) and open pulses are π pulses. Total mixing time during NC′ correlation is equal to 4T. Similar to T_2 CPMG experiments, there is no continuous wave decoupling. Therefore, π pulse is set in the middle of t1 evolution. The second t2 evolution in the ^{15}N channel occurs after mixing time. It may affect the sensitivity of the experiment for low ν_{CPMG} values.*

Another question that had to be analyzed was the choice of phase cycling during the applying π pulses in CPMG train pulses. There are two options: constant phase cycling (ph=0 or 1) or xy phase cycling [76]. The experimental observations (see figure 6.2) showed that xy phase cycling was the most effective since it compensates errors caused by pulse imperfections [77]. In particular, there is a negligibly slight intensity difference for xy-16 and xy-32. Therefore, one can assume that xy-16 is the optimal phase cycling scheme.

The critical part of the experiment was a choice of appropriate π pulses. The point is that for the T_2 CPMG experiment, both hard and soft pulses showed a signal gain, although there were dips of the intensity at random ν_{CPMG}. For HNCO, hard pulses applied on both channels (^{15}N and ^{13}C) did not give any signal gain. Hence, the adjustment of pulse duration is essential in such kind of experiments. Consequently, soft π pulses with a duration of at least 20 usec (applied on both channels) demonstrated a gain during the optimization of ν_{CPMG}.

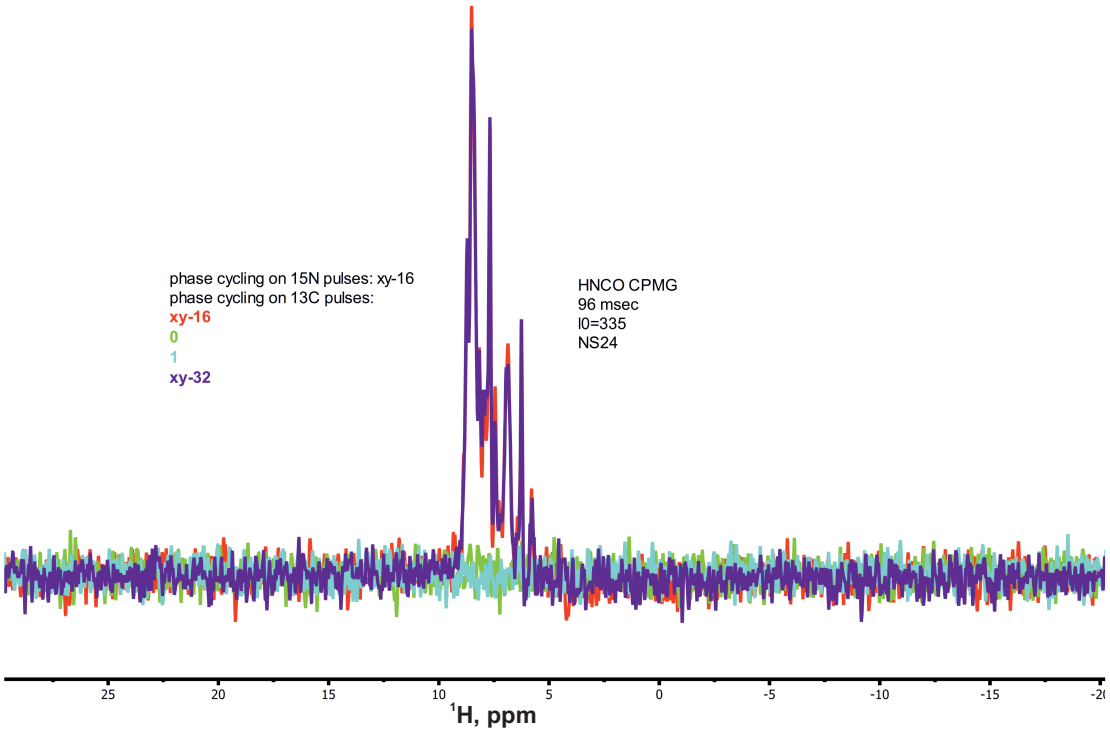

Figure 6.2: *1D spectra at 4T=96 msec for different phase cycles. Primitive (x or y) phase cycling is impractical at higher ν_{CPMG}. However, the implementation of xy phase cycling is promising. Moreover, xy-16 seems optimal since it gives the same gain as xy-32.*

Figure 6.3 compares the of HNCO CPMG experiment at a certain ν_{CPMG} (which is equal to 436 Hz in this case) at 2T=32 msec. In this case "conventional" experiment refers to $n = 1$. The results give evidence of the signal gain in the CPMG short-range experiment.

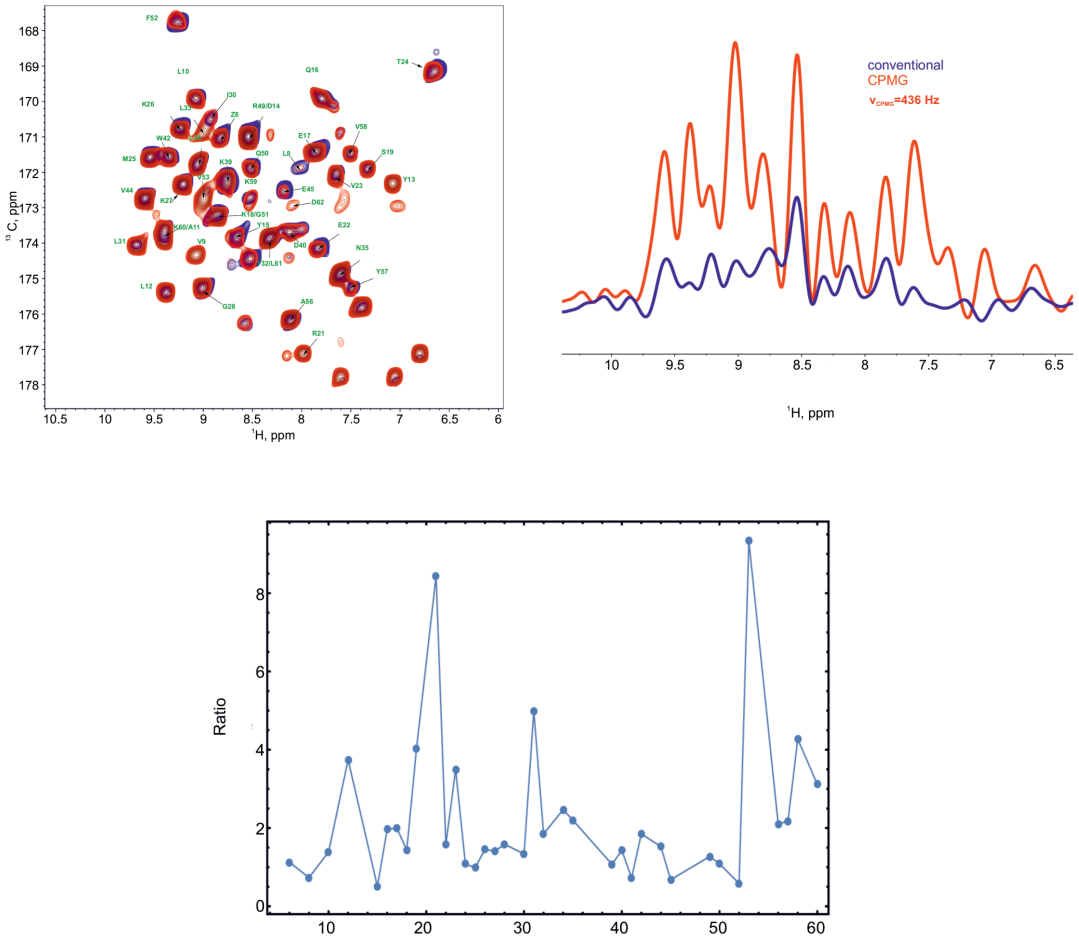

Figure 6.3: *HNCO CPMG at 2T=32 msec (4T=64 msec) for SH3 20% back exchanged protein. Blue refers to the conventional experiment (n=1) and red refers to* $\nu_{CPMG} = 436$ *Hz. The number of scans was set to 16. The ratio of intensities varies between 1 and 8 for the majority of assigned residues. However, five residues do show a gain of less than 1.*

Figure 6.4 illustrates the same results for 4T=66 msec and 96 msec, respectively. Since the decoupling is absent during NC′ correlation and T_2' relaxation starts to dominate, it is obvious to observe a smaller signal for conventional experiment. In the CPMG case, the sensitivity of the signal increases for larger ν_{CPMG}

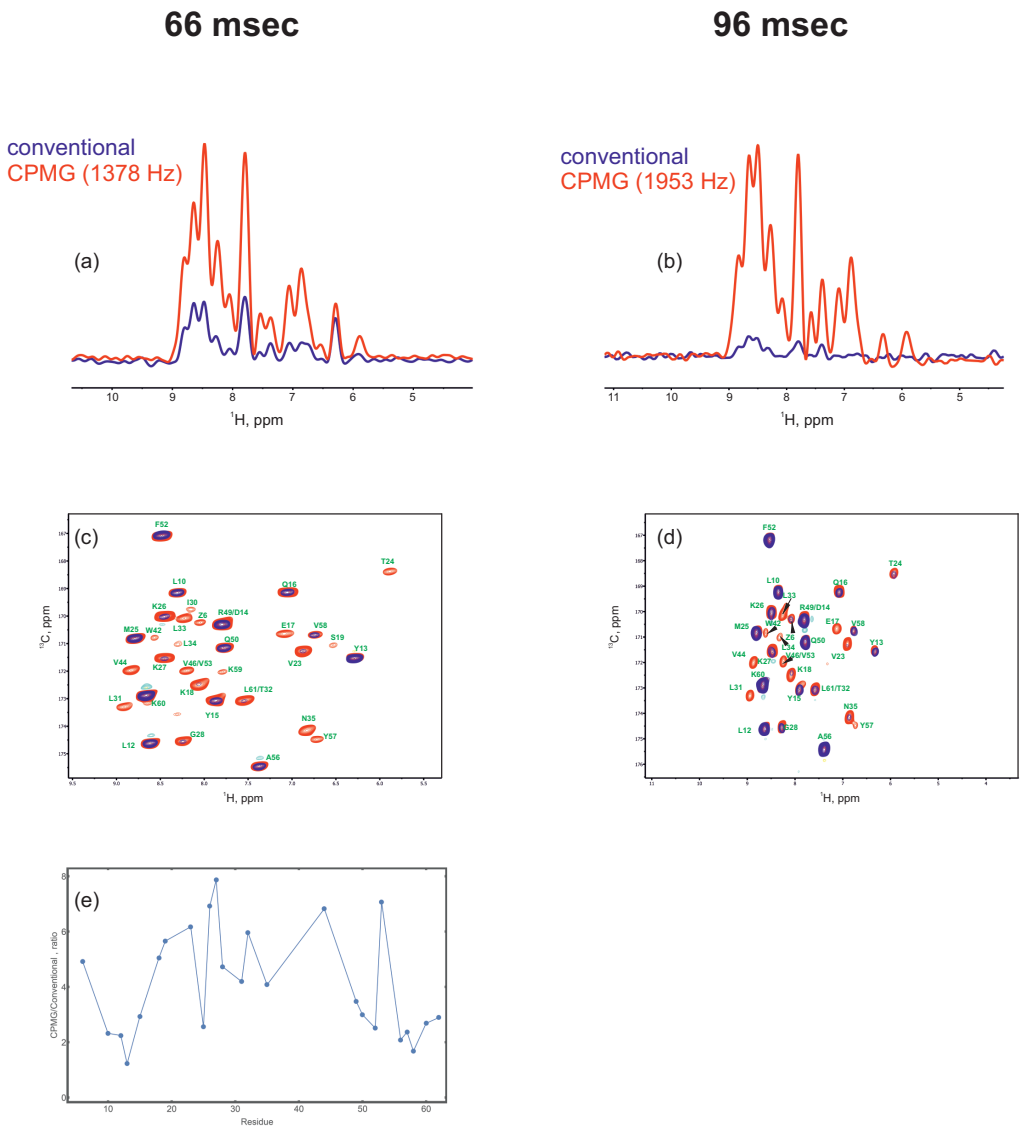

Figure 6.4: *HNCO CPMG for 2T=33 msec (4T=66 msec) and 48 msec (4T=96 msec), respectively. Figures (a) and (b) demonstrate 1D spectra of conventional and CPMG experiments for 66 and 96 msec mixing times; (c) and (d) display CH spectra with assigned residues. Even for $\nu_{CPMG} < 2$ kHz, the intensity gain is more extensive than in the conventional case. Figure (e) shows the signal gain for 66 msec mixing time experiment.*

Finally, figure 6.5 displays the CH spectrum for 2T=132 msec. Typically, for larger mixing times, the T_2' relaxation becomes significant. Hence, it requires lots of scans. In this CPMG experiment, it took 96 scans (for example, to get a comparable spectrum in a standard HNCO experiment with the same mixing time, which

may require at least 512 scans) to receive a relatively good spectrum where most residues are assigned. What is more surprising is that the $\nu_{CPMG} = 860$ Hz, which is relatively small.

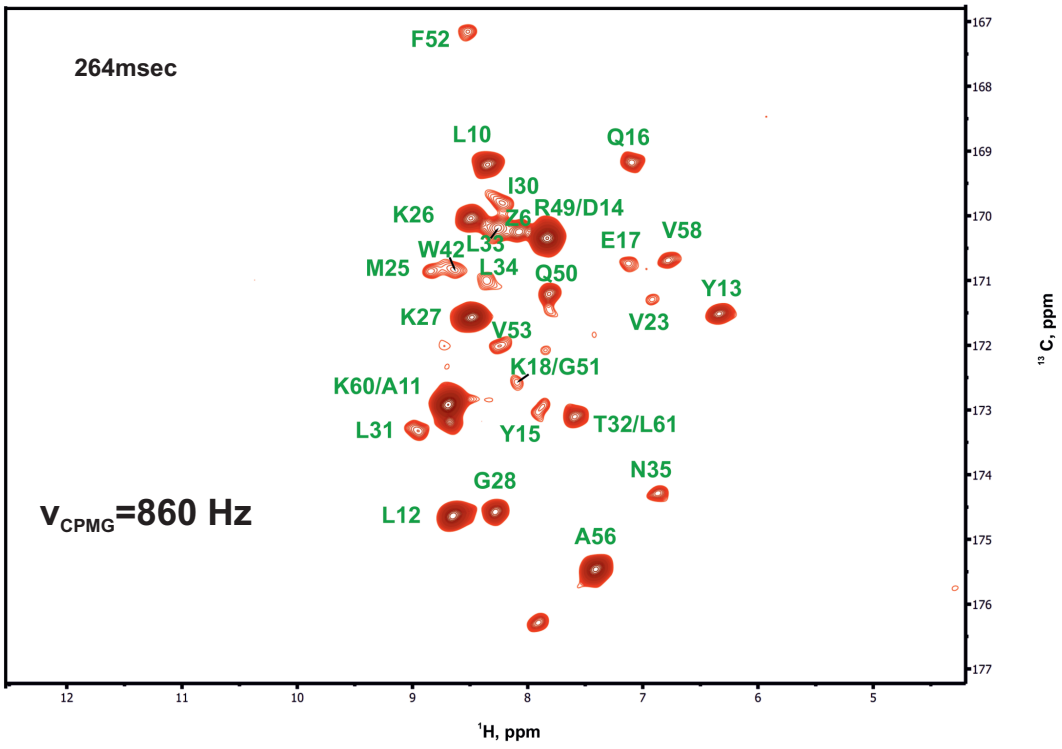

Figure 6.5: *HNCO CPMG experiment for 4T=264 msec. Although the ν_{CPMG} is less than 1 kHz, the majority of residues can be assigned in the CH spectrum.*

To summarize this paragraph's results, the signal gain increases as a function of ν_{CPMG}. Additionally, it becomes visible for values up to 2 kHz. Furthermore, these results are considered for experiments without a continuous decoupling during NC′ correlation. Despite this, it is also necessary to determine whether the CPMG method can detect H-bonds. The following question will be discussed in the next paragraph.

6.2 The Observation of H-bonds in Solid-State NMR using CPMG pulse scheme

6.2.1 Conventional HNCO Experiment

This paragraph is focussed on the practical aspects of H-bonds detection for SH3 protein. Mainly, the results presented here correspond to the HNCO CPMG experiment, which has been mentioned in the previous paragraph as well as the standard HNCO experiment. In this paragraph, it is also called "conventional", but compared to the previous one, this term is related to the experiment that has been taken from solution-state NMR and adapted for the solid-state case experiment.

First, it was necessary to repeat a conventional short-range experiment to complete the residues assignment in the HC plane. For this purpose, triple resonance HCONH and HCANH experiments have been recorded using NUS [78] (Non-Uniform Sampling). The principle of NUS is that records non-uniform data points. Subsequently, reconstruction algorithms help to get a correct spectrum from a sparse data set. This method is beneficial for multidimensional experiments (in particular, for 3D experiments). The obtained result is demonstrated in figure 6.6. Also, the aim was to compare the results of the HC assignment from [39]. According to the results, most residues have similar chemical shift values except for residues E45, I30, and D29. In figure 6.6, residues have actual chemical shift values.

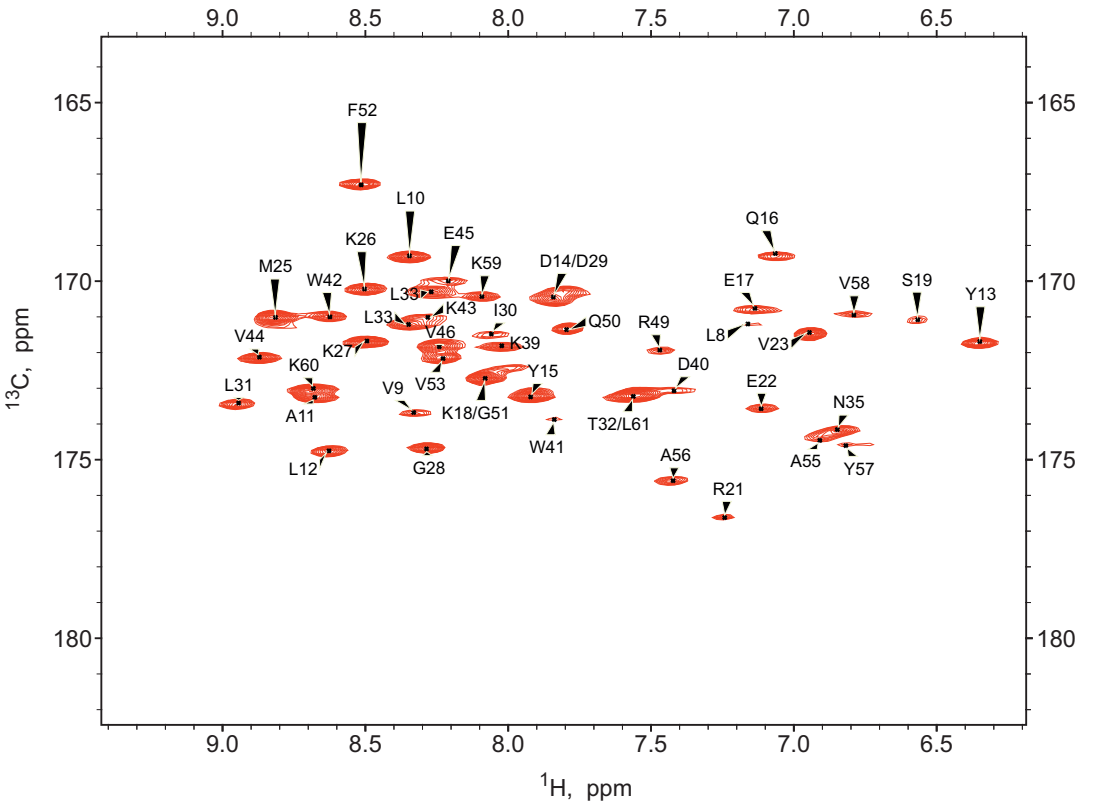

Figure 6.6: *HC spectrum of SH3 recorded for CP-based HNCO short range experiment using NUS.*

The next step was to identify all possible H-bonds for the SH3 protein. As the structure of this particular protein has been well studied, it was sufficient to find them using the PyMol program [79]. The complete list of all possible H-bonds is shown in table 6.1. For the visualization, the crystal structure 2NUZ has been employed.

In order to get the H-bond, there must be a donor and acceptor. Usually, the donor is a strongly electronegative atom (such as N), which is covalently bonded to the H-bond. Acceptor is an electronegative atom or ion which contains a lone pair involved in the H-bond (for example, carbonyl (C′) atom). The visual representation of the F52-R21 H-bond is represented in figure 6.7.

As it has been mentioned several times, detecting H-bonds is possible via long-

Pair, number	**Donor residue, HN**	**Acceptor residue, CO**	**Distance, Å**
1	V9	L31	2.8
2	L10	K59	2.8
3	A11	D29	2.9
4	L12	Y57	2.8
5	Y15	M25	3.0
6	T24	E17	3.3
7	M25	Y15	2.9
8	K26	D29	2.9
9	K27	D14	2.8
10	G28	A11	2.9
11	D29	A11	3.0
12	L31	V9	2.8
13	T32	E45	3.2
14	L33	E7	2.9
15	L34	K43	2.8
16	N35	K43	3.1
17	T37	N35	3.0
18	W42	V53	2.9
19	K43	N35	3.0
20	V44	G51	2.9
21	E45	T32	2.8
22	V46	R49	2.8
23	G51	V44	3.0
24	F52	R21	2.9
25	V53	W42	3.0
26	A55	D40	2.8
27	K59	L10	2.9
28	L61	L8	3.1

Table 6.1: A complete list of H-bonds that the PyMol software program has predicted.

range HNCO experiments. Practically, the H-bond is represented by two peaks at a particular nitrogen chemical shift: the most substantial peak is a diagonal peak (in other words, directly bonded peak, donor), and the weakest peak (cross peak), which belongs to the acceptor. Both these peaks have the same ^{1}H chemical shift. The analysis of all H-bonds has been performed using POKY software [80].

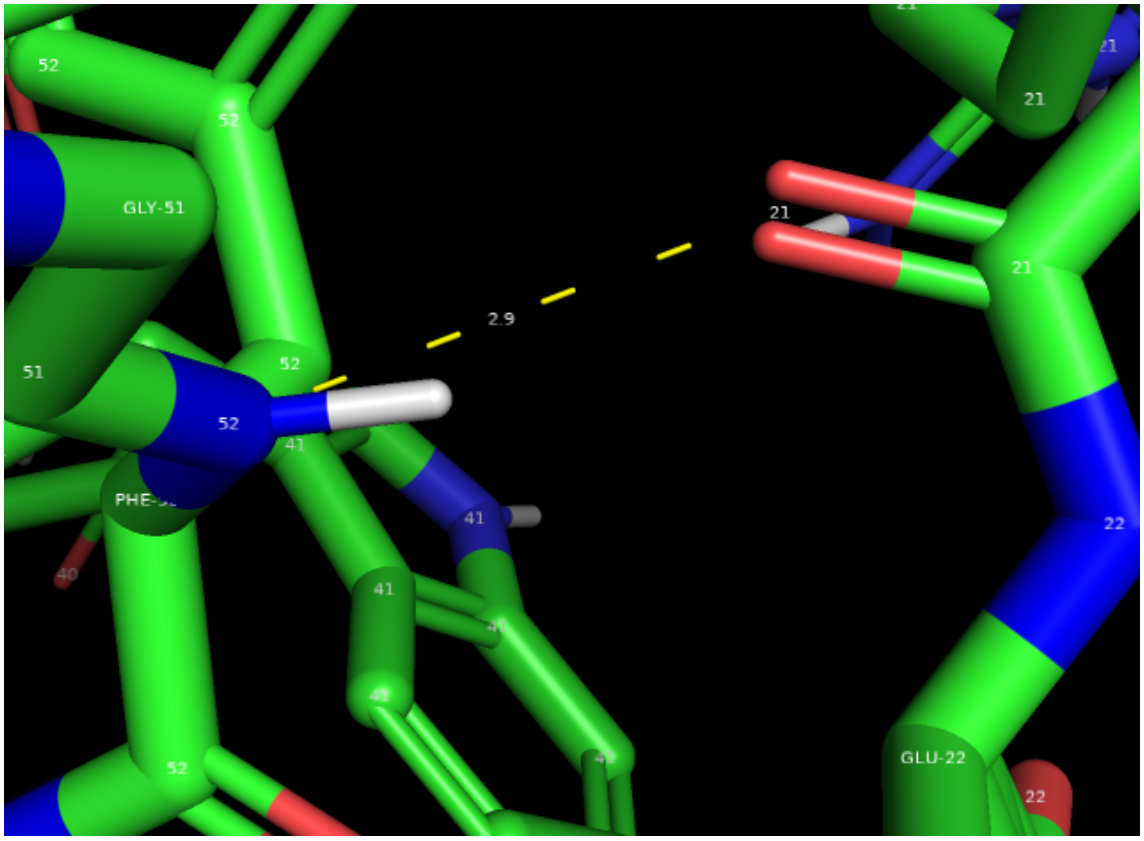

Figure 6.7: *An example of the H-bond between residues F52 (donor) and R21 (acceptor). Blue corresponds to the N atom, while green-red lines refer to the* C=O *group and white is a amide proton. The distance between atoms is in Angstroms.*

Figure 6.8 shows the H-bond Y15-M25 recorded in conventional HNCO experiment. Left and right strips were extracted from the short-range experiment. In particular, the left one is the donor (Y15) and the right one is the next following acceptor residue (in this case, it is K26). The middle strip is extracted from the long-range experiment and has the same ^{15}N frequency as a donor. The experiment was recorded with 4T=132 msec total mixing time. The number of scans was set to 32. Since the S/N ratio was too small, it was required to record an additional experiment with the same parameters resulting in 72 hours of total acquisition time. The 4 H-bonds (L31-V9, V44-G51, M25-Y15, L10-K59) are illustrated in Appendix B.

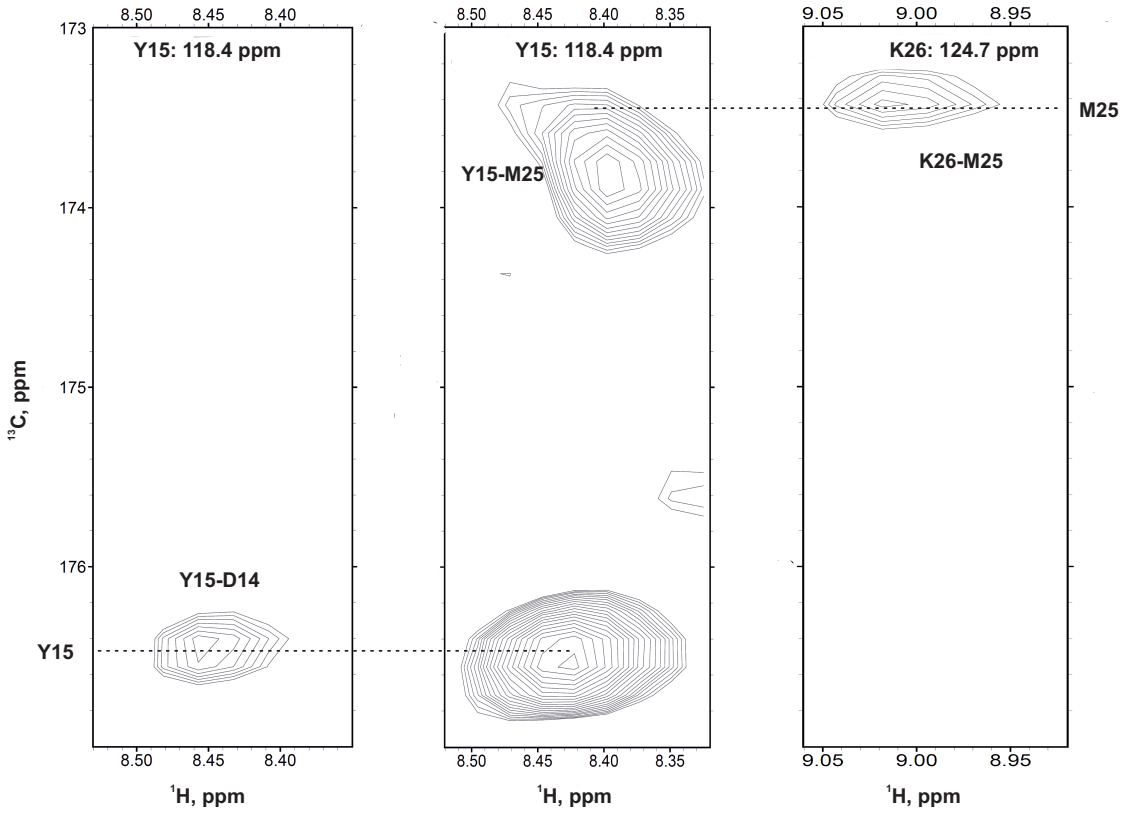

Figure 6.8: *H-bond Y15-M25 detected using HNCO conventional experiment with 4T=132 msec mixing time. The left and right strips are from short-range experiments and the middle strip with a cross peak is from a long-range experiment.*

6.2.2 HNCO CPMG

As soon as conventional experiments were finished, the next intriguing part was to record HNCO CPMG experiments. The idea is that CPMG method increases the sensitivity of the signal, hence, one can observe cross-peaks using less number of scans, therefore, reducing experimental time. Three different mixing times (4T) have been chosen: 96 msec, 132 msec, and 264 msec. The first mixing time was chosen due to optimization reasons, as the signal was relatively high in this case. As for the rest mixing times, the idea was to refocuss direct $^{1}J_{NC\prime}$. In this case, T value has to be proportional to $\frac{n}{^{1}J_{NC\prime}}$, where $^{1}J_{NC\prime}$ is 15 Hz, n is integer. In particular, n=1 and n=2 were chosen. Besides, two aspects were taken into account: first, ^{15}N π pulses were set from 20 usec to 38.8 usec in CPMG blcoks to make them rotor synchronized; second, the loop counter was increased, therefore, ν_{CPMG} was

typically more than 2 kHz (7.6 kHz for 96 msec, 8.7 kHz for 132 msec and 3.25 kHz for 264 msec). One-dimensional spectra for three mixing times and comparison to the conventional experiments are shown in figure 6.9. Since the T_2' relaxation is dominant at larger mixing times, 96 scans were required for 264 msec to see the effect of CPMG. Overall, the S/N ratio is more than five for 132 and 264 msec. For 4T=96 msec, the gain is not so high which makes sense because of the short time.

Experimental observations revealed that carbon carrier frequency affects the quality of the HC spectrum. Optimization was performed from 167 to 185 ppm (see figure 6.10). The range corresponds to the CO chemical shift value. The outcome revealed a Gaussian-like behavior of 1D spectra with a maximum of 173-177 ppm. Another problem was related to the quality of 2D HC spectra (see figure 6.11). At specific carrier frequencies, some artifacts have emerged generating extra peaks that could be identified as cross-peaks (see 167 ppm and 182 ppm). However, in the case of 173 ppm, the artifacts have not been visible but to ensure that they will not contribute to the "possible" H-bonds, Bloch Siegert ^{13}C-shaped pulses were introduced in t1 evolution. Also, it is worth noting that not all detected H-bonds had cross peaks at carrier frequency value. It indicates that possible artifacts did not contribute to the H-bond pairs.

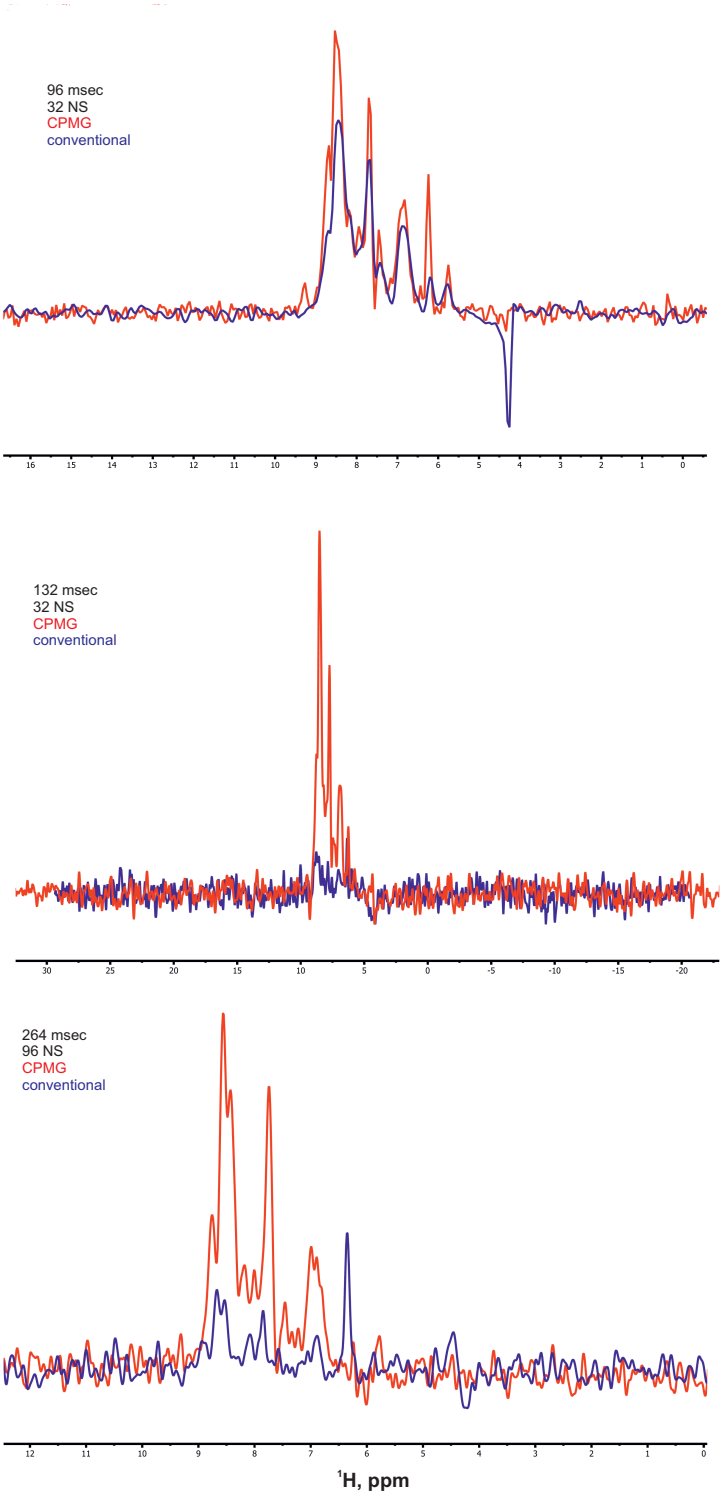

Figure 6.9: *1D spectra of HNCO conventional (blue) and CPMG (red) with different mixing times. HNCO CPMG experiments seem to show a more significant gain for longer mixing times 2T=66 msec (4T=132 msec) and 2T=132 msec (4T=264 msec), respectively.*

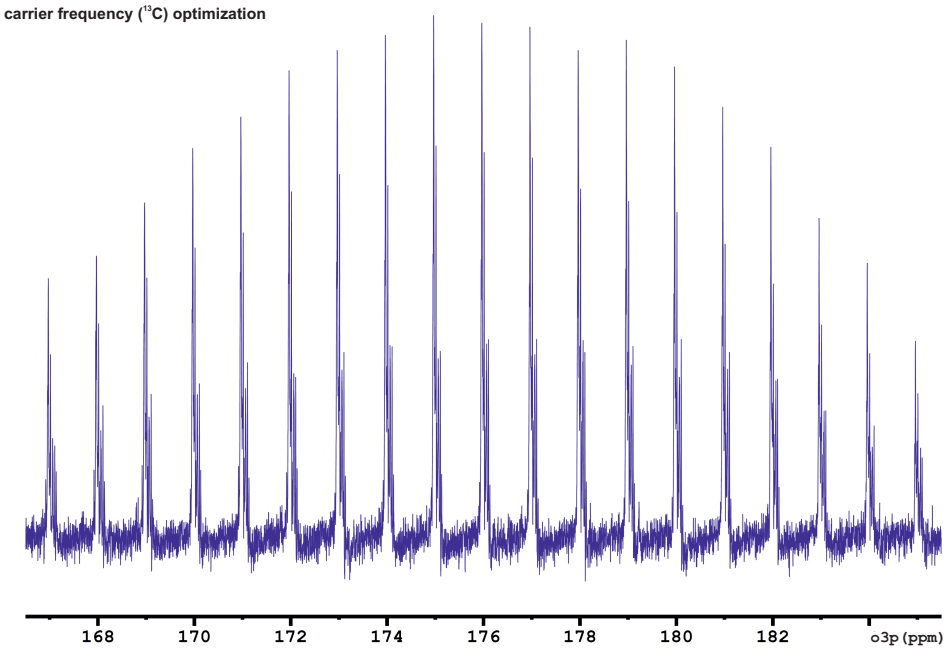

Figure 6.10: *Gaussian-like dependence of the signal as a function of ^{13}C carrier frequency in the HNCO CPMG experiment.*

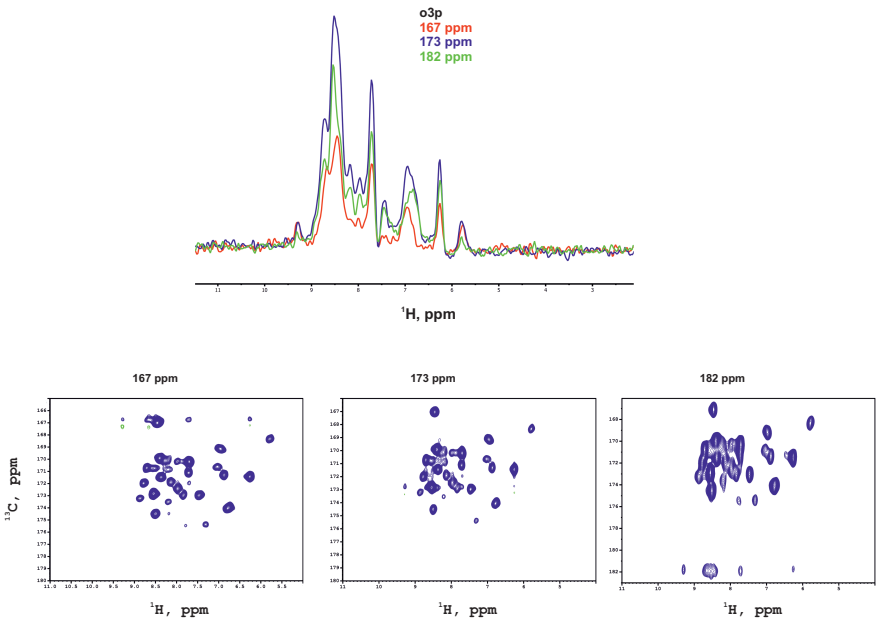

Figure 6.11: *1D and 2D HC spectra recorded at different carrier frequencies (167 ppm, 173 ppm, and 183 ppm). The shift of carrier frequencies leads to the artifacts.*

Figure 6.12 depicts the strip from HNCO CPMG for 4T=96 msec where H-bond F52-R21 is represented. The right part of the figure contains a 1D ^{13}C spectrum from the middle strip to see the cross peak. The signal from the cross peak is generally weak but still visible. Only three H-bonds were observed (see Appendix C) including K27-D14 and K26-D29.

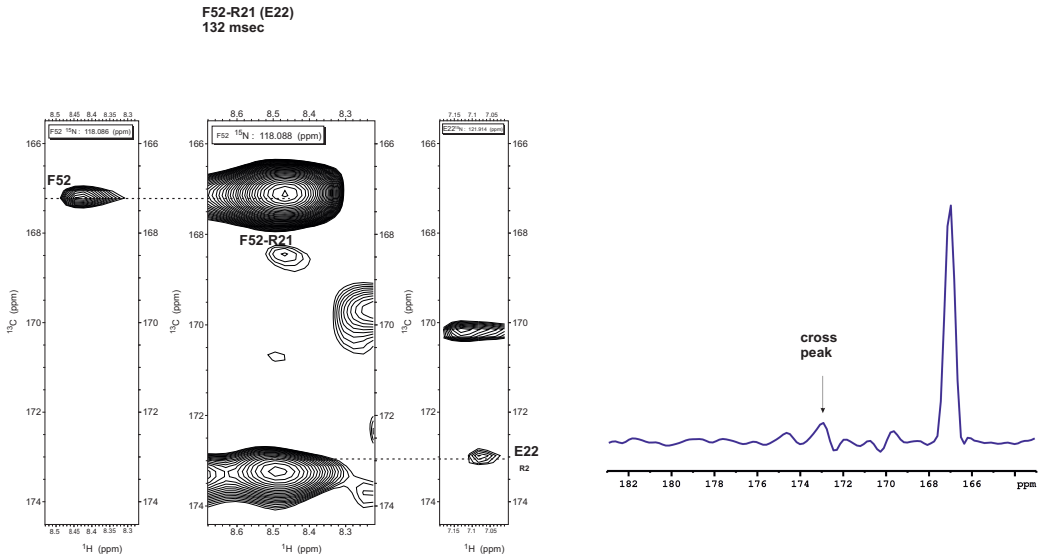

Figure 6.12: *HNCO CPMG. F52-R21 H-bond was detected with a mixing time of 2T=48 msec (4T=96 msec). Left and right strips refer to the short-range experiment. The middle strip is the long-range CPMG experiment. The 1D slice on the right shows the presence of cross-peak whose signal differs from the noise.*

Two extra experiments with 2T=66 msec and 2T=132 msec were recorded using the same conditions (number of scans, relaxation delay, pulse durations). Similar to the 4T=96 msec experiment, F52-R21 H-bond was also observed in all cases (figure 6.13). Cross-peaks have a lower intensity compared to the diagonal peak (F52) . Crucially, however, the relative ratio between the cross and diagonal peaks decreases with the increased mixing time, implying that the cross peak is not the artifact or something else. One note worth pointing here is that 4T=264 msec mixing time (despite its smaller S/N ratio) reveals more H-bonds than 4T=132 msec experiment (K26-D29 and K59-L10). The fundamental reason for detecting more H-bonds is

clear: a small value of J-coupling ($^{3h}J_{NC'}$). The remaining H-bonds for 4T=132 msec are in Appendix C.

The calculated values for $^{3h}J_{NC'}$ are presented in table 6.2 for conventional and CPMG experiments with 4T=132 msec. The variation of values for H-bonds can be explained by the low S/N ratio for cross peaks in long-range experiments. J-coupling values can be defined as a ratio between long-range (see figure 6.1 with n=1) and short-range (where carbonyl pulses are shifted by $\frac{1}{^1J_{NC'}}$ delay in order to "reduce effective time for ^{15}N to$^{13}C'$ defocussing and refocussing to a value of $2(T-\frac{1}{^1J_{NC'}}) = \frac{2}{2*^1J_{NC'}}$" [42]) intensities. The intensity for the long-range experiment is proportional to $\sin^2\Big(2\pi * {}^{3h}J_{NC'} * (\frac{T}{^1J_{NC'}})\Big) * \cos^2\Big(2\pi * {}^1J_{NC'} * \frac{T}{^1J_{NC'}}\Big)$ while for the reference experiment the intensity is proportional to $\sin^2\Big(2\pi * {}^1J_{NC'} * [\,(\frac{1}{^TJ_{NC'}}) - 16.5msec]\Big) * \cos^2\Big(2\pi * {}^{3h}J_{NC'} * [\,(\frac{T}{^1J_{NC'}}) - 16.5msec]\Big)$. By dividing these terms, one can obtain the value for the long-range scalar coupling, such as

$$|^{3h}J_{NC'}| \approx \frac{1}{2\pi T}\sqrt{\frac{I_{lr}\cdot NS_{ref}}{I_{ref}\cdot NS_{lr}}} \tag{6.2.1}$$

where T= 33.3 msec, I_{lr}, I_{ref}, NS_{lr} and NS_{ref} are long-range (cross-peak) and reference (diagonal peak) intensities and number of scans, respectively.

The reference HNCO CPMG experiment has another structure. Two CPMG blocks have the same delay but different loop counter values (k and m, for example, where k+m=n, see figure 6.1) separated by the nitrogen π pulse.

$$2\tau * k = \Delta_1 \tag{6.2.2}$$

$$2\tau * m = \Delta_2 \tag{6.2.3}$$

The absolute time difference between the 2 CPMG blocks is equal to

$$|\Delta_1 - \Delta_2| = \frac{1}{^1J_{NC'} * 2} \Rightarrow k - m = \frac{33msec}{2\tau} \tag{6.2.4}$$

And finally the ratio of long-range and reference intensities is

$$\frac{I_{lr}}{I_{ref}} = \frac{NS_{lr} * sin^2\Big(\pi * {}^{3h}J_{NC'}(\Delta_1+\Delta_2)\Big) * cos^2\Big(\pi * {}^1J_{NC'}(\Delta_1+\Delta_2)\Big)}{NS_{ref} * sin^2\Big(\pi * {}^1J_{NC'}(\Delta_1-\Delta_2)\Big) * cos^2\Big(\pi * {}^{3h}J_{NC'}(\Delta_1-\Delta_2)\Big)} \tag{6.2.5}$$

Using the expression (6.2.4) and considering that $\Delta_1 + \Delta_2 = \frac{2}{{}^1J_{NC'}}$

$$\frac{I_{lr}}{I_{ref}} = \frac{NS_{lr}}{NS_{ref}} * \left(\pi * {}^{3h}J_{NC'}(\Delta_1 + \Delta_2)\right)^2 \tag{6.2.6}$$

H-bond pair	${}^{3h}J_{NC'}$ **conv, Hz**	${}^{3h}J_{NC'}$ **CPMG, Hz**
Y15-M25	1.10 ± 0.41	none
M25-Y15	0.60 ± 0.12	0.94 ± 0.38
D29-A11	0.44 ± 0.09	none
L31-V9	1.56	none
V44-G51	1.04 ± 0.43	0.87 ± 0.24
A11-D29	none	1.78 ± 0.32
L12-Y57	none	1.21 ± 0.34
K27-D14	none	2.03 ± 1.12
N35-K43	none	2.02 ± 1.05
F52-R21	none	1.34 ± 0.2

Table 6.2: A table with calculate ${}^{3h}J_{NC'}$ values. The deviation of the values is due to the low S/N ratios of cross-peaks.

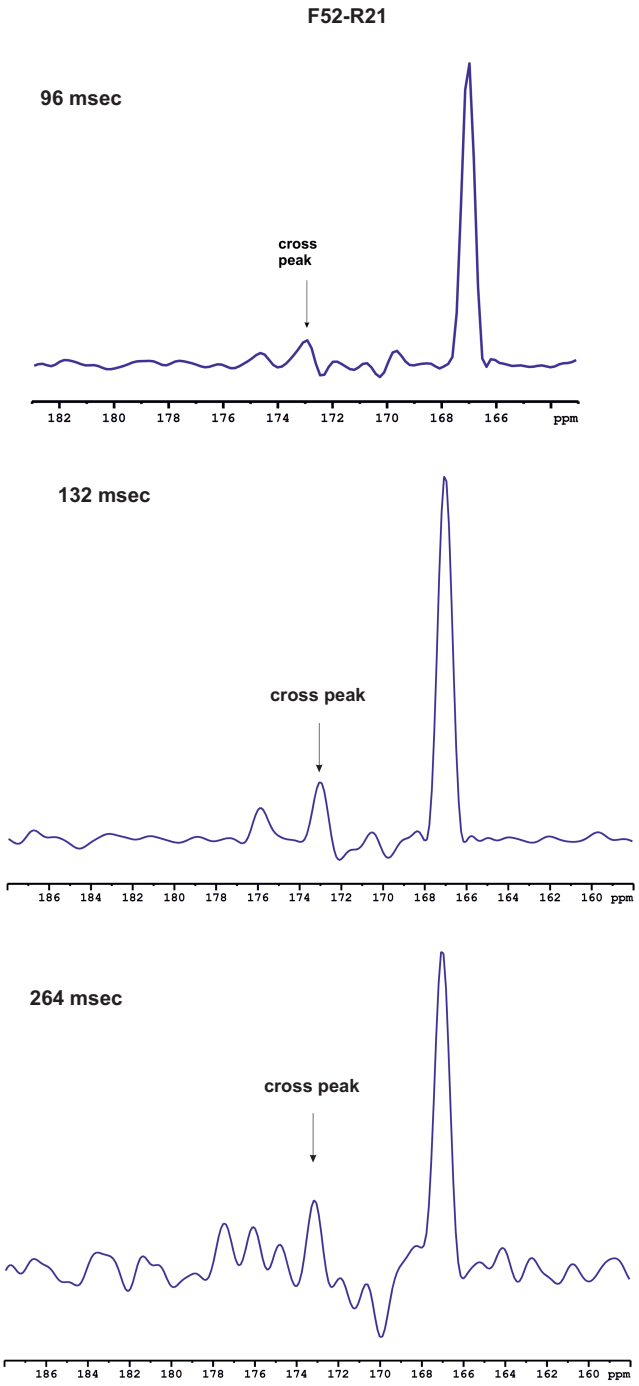

Figure 6.13: *1D traces of F52-R21 H-bond for different mixing times (4T=96 msec, 4T=132 msec and 4T=264 msec). The ratio between diagonal and cross peak intensities decreases with a mixing time. Therefore, the cross peak becomes more visible.*

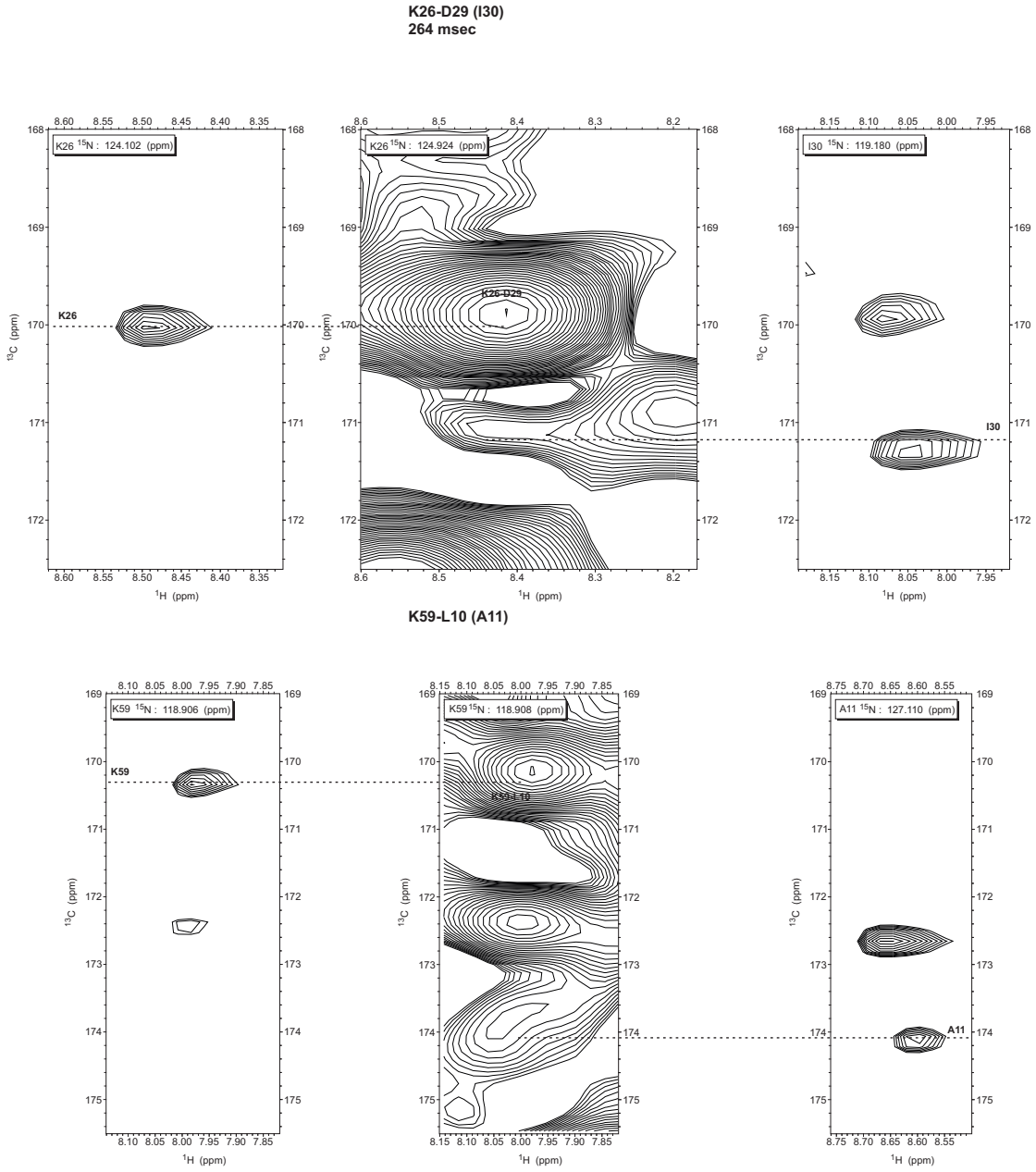

Figure 6.14: *K26-D29 and K59-L10 H-bonds found at 2T=132 msec (4T=264 msec) mixing time in the HNCO CPMG experiment.*

Chapter 7

Measurement of Dipolar Coupling using REDOR Experiment

The following chapter represents the results of the measurements of dipolar coupling values for SH3 and hIAPP proteins. The dipolar coupling was determined using the REDOR method. A detailed description of the experiment can be found in [81].

7.1 Dipolar coupling calculations in SH3 protein

The new, improved version of the REDOR experiment (see figure 7.1) proposed by P. Schanda in [81] has a prominent feature that differs from the standard experiment: shifted delays introduced in CPMG blocks. According to [81], shifting one of the sets of π pulses helps to scale the effective dipolar oscillation frequency, which becomes significant for samples with low sensitivity.

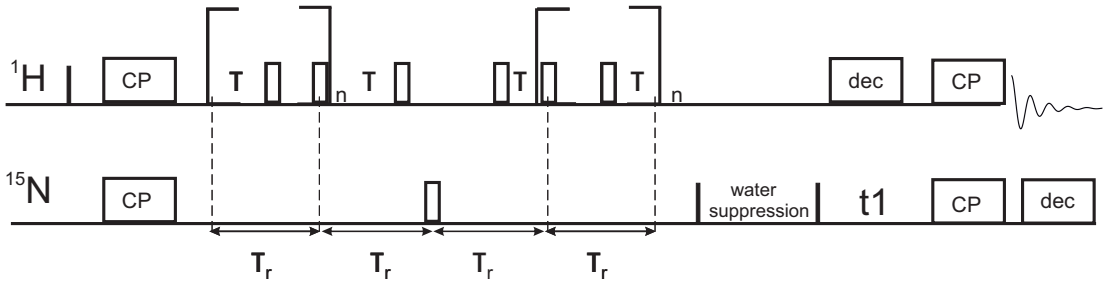

Figure 7.1: *Pulse scheme for CP based REDOR experiment. Rotor period was set to 18 usec corresponding to the spinning frequency of 55555 Hz.*

The measurements were done for SH3 protein (20% back exchanged). The rotation frequency was set to 55555 Hz to make the rotor period close to the integer value (18 usec). In this configuration, the shifted delay τ could not exceed nine usec. Optimization of this delay gave the maximum signal for the shifted delay of 3 usec. The total dephasing time was 1.2 msec.

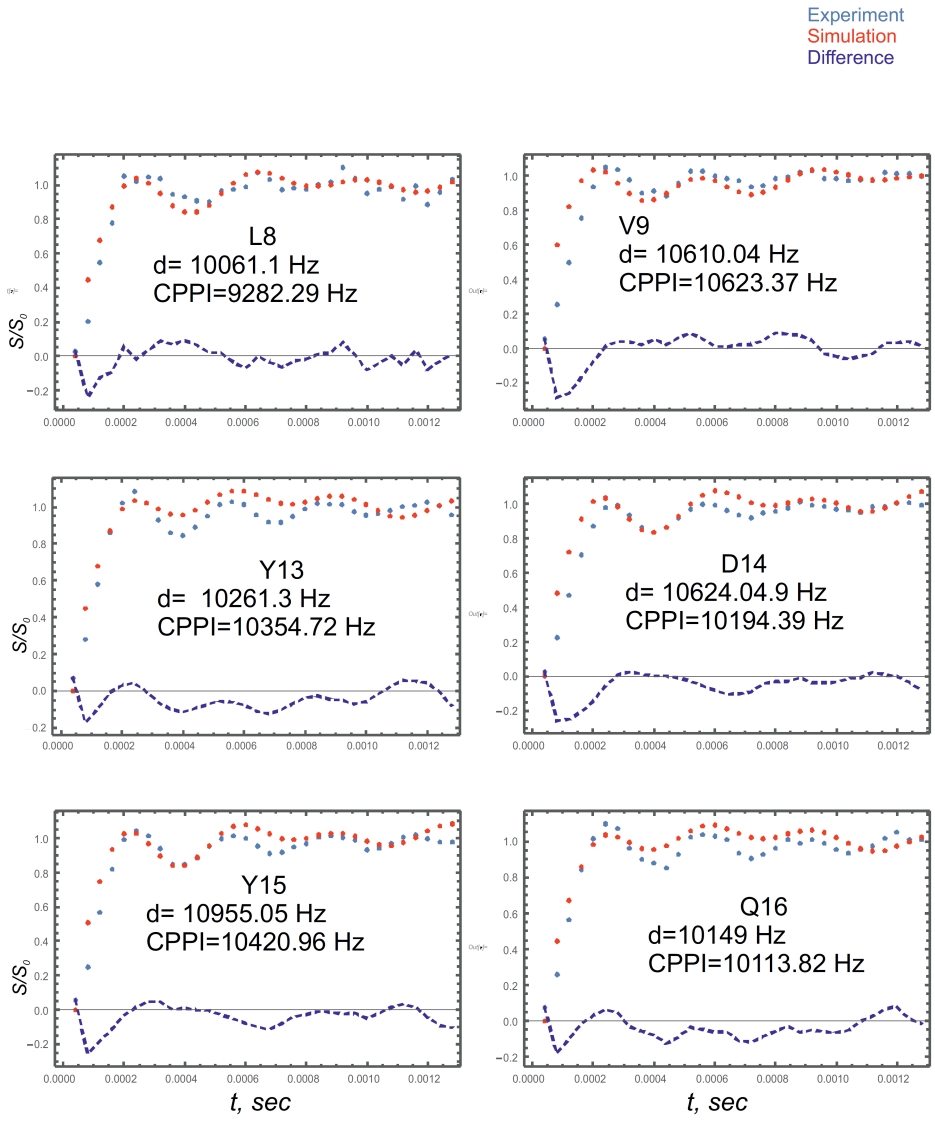

Figure 7.2: *REDOR curves for SH3 residues (light blue) and simulated curves (red); the difference is shown in dark blue. Calculated values for dipolar coupling (d) are in good agreement with previous results (CPPI, see [82]).*

In control experiments, it has been found out that all REDOR curves had an overshoot that exceeded the maximum value of 1. The study in [81] fails to answer the question whether there are any additional factors contributing to the overshoot. In this study, the CP-based experiment was replaced by the INEPT based since it did not have any overshoot in the first maximum in the REDOR curve. Six REDOR curves with calculated values for dipolar couplings are shown in figure 7.2. The REDOR curves were computed using the SIMPSON software program [83] with the subsequent visualization in Wolfram Mathematica. The dipolar coupling values obtained in the experiment were compared to the results from phase-inverted CP (CPPI) [82]. The remaining REDOR curves can be found in Appendix D. A potential problem that is visible in most curves is that experimental and simulated curves have a difference in the first six data points. This can be explained by choice of the shifted delay in simulation, which was set to 4 usec since the actual value (3 usec) computed dipolar coupling values. A further argument is that actual finite π pulses were used for the simulation.

Figure 7.3 demonstrates the calculation of the order parameter (S^2) for all detected residues. In case if the motion is axially symmetric, the order parameter can be defined as the ratio between experimental dipolar coupling (δ_D^{expt}) and theoretical one (δ_D^{rigid}) corresponding to the N-H bond length 1.015 Å

$$S^2 = \frac{\delta_D^{expt}}{\delta_D^{rigif}} \tag{7.1.1}$$

The results lend strong support to the argument that most residues are rigid since S^2 is around or more than 0.9. According to [82], residues that are stabilized by the H-bonds exhibit less flexibility and possess a larger dipolar coupling. For flexible residues such as T24, T37, l61, and D62 amide protons are bonded only to water, therefore, they have a smaller dipolar coupling. Since dipolar coupling values agree with the results from previous work [82], the experiments can be considered successful.

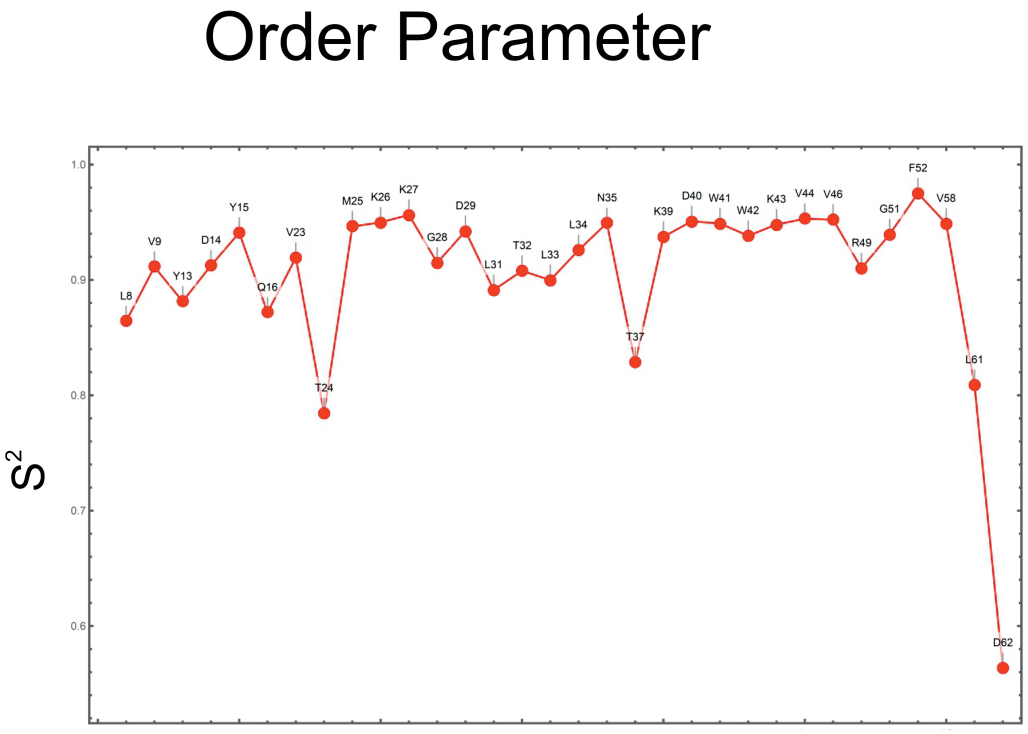

Figure 7.3: *Order parameter values for residues in SH3 protein.*

7.2 Dipolar coupling calculations in hIAPP protein

Similar to the previous paragraph, dipolar coupling values were measured for 1.3 mm rotor 20% back exchanged hIAPP protein. The only difference is that the experiments were made at 800 MHz spectrometer. Optimization of the shifted delay gave the optimal value of 3 usec. Figures 7.4 and 7.5 illustrate REDOR curves. Compared to the SH3 protein, experimental curves (blue) have more significant fluctuations, especially after the first local maximum. From the sparse distribution of experimental data points, the calculated dipolar coupling values should have larger errors. Table 7.2 presents the exact calculated values for dipolar couplings with estimated errors.

Residue	**Dipolar coupling, Hz**	**Error, HZ**
3N	9453.49	950
5A	9037.12	1600
8A or 25A	8527.94	500
10Q or 18H	8105.39	300
11R or 16L	8542.67	250
12l	8234.98	300
19S	9431.55	1000
21N	8971.14	500
22N	9972.85	950
27L	9010.59	600
28S or 30T	8916.15	400
29S	9334.49	950

Table 7.1: Calculation of dipolar couplings values for hIapp protein, including error bars.

The error bars were calculated using the expression for the reduced χ^2_{red} from [81] which can be rewritten as

$$\chi^2_{red} = \frac{1}{10}\sum_{i=1}^{12}\frac{((\Delta S/S_0)_{i,expt} - (\Delta S/S_0)_{i,calc})^2}{\sigma^2_{i,expt}} \tag{7.2.1}$$

where ΔS is the REDOR experiment, S is the reference experiment without refocussing pulses (i.e., without CPMG blocks), $\sigma^2_{i,expt}$ is the statistical error. Reported error bars were defined for the dipolar couplings where χ^2_{red} exceed the minimum value by 1(see Appendix D).

Analysis of the data revealed that assigned residues in N- and C-terminals have a smaller order parameter (S^2 is less than 0.8) compared to the SH3 protein. The problem is, however, that the S/N ratio and overlap of spectral residues can not provide good quantitative information about dipolar coupling values. Despite this, one can assume the same dipolar coupling dependence for residues in both terminals.

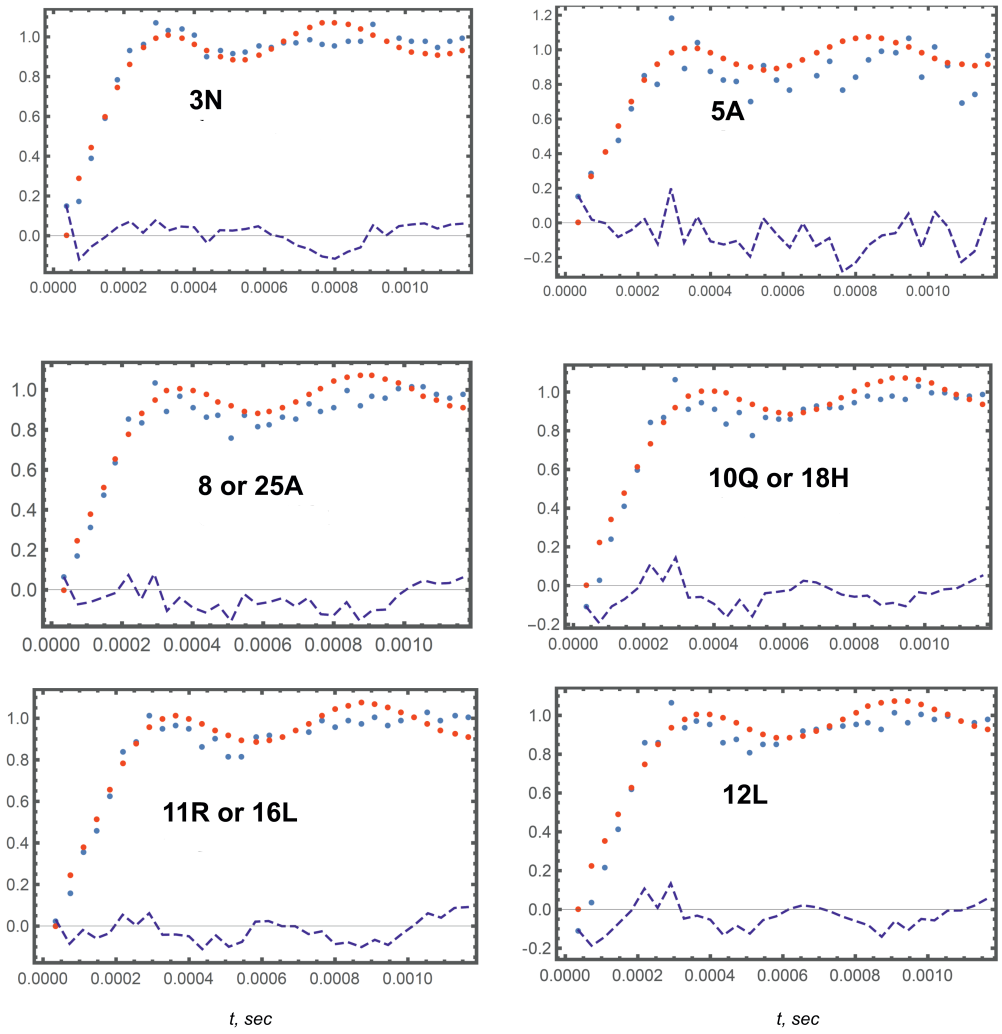

Figure 7.4: *REDOR curves for hIAPP protein. Parameters used in this experiment are identical to the experiments with SH3 except for the usage higher magnetic field (800 MHz), and shifted delay was set to 3 usec. Also, experimental results possessed huge fluctuations due to a poor S/N ratio.*

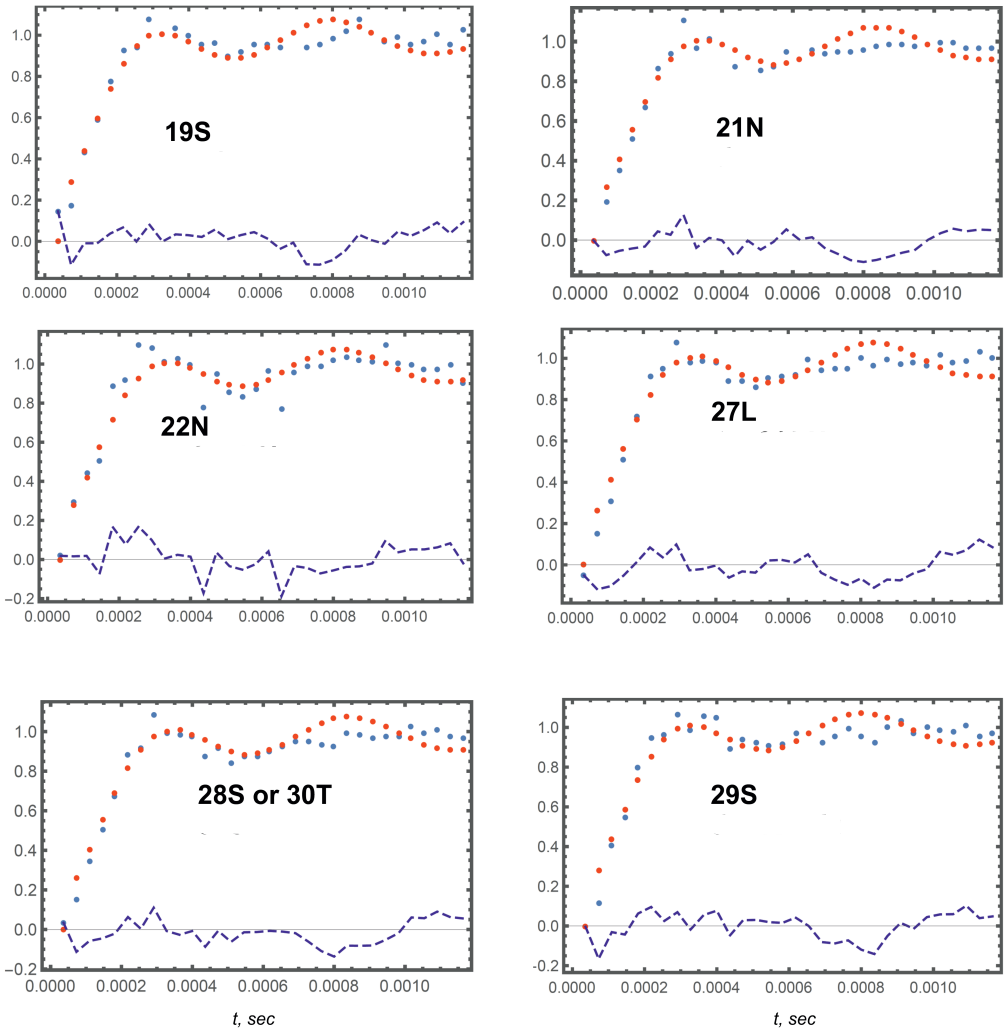

Figure 7.5: *REDOR curves for hIAPP protein. Compared to the first figure, the fluctuations are less, leading to smaller error values (table 7.1).*

Chapter 8

Summary

Overall, the results presented in this thesis represent an initial attempt to apply CPMG pulse trains in solid-state experiments for sensitivity enhancement with a following H-bond detection.

First, T_2 CPMG experiments revealed the increase in signal sensitivity for different mixing times. For 40 msec or 60 msec, the gain may not be so impressive since the T_2' relaxation is not dominant. However, when the mixing was above 100 msec, the single spin echo experiment showed very few peaks. The CPMG version was way better, indicating the increase of the S/N ratio more than ten times. Even for shorter mixing times, the intensity ratio was in a range from 2.5 and 3. It has been shown in Chapter 5 that the duration of π pulses in spin echo block behave differently as a function of ν_{CPMG}. In particular, hard pulses have intensity dips at almost random ν_{CPMG} values, which could lead to misunderstanding CPMG contribution to sensitivity enhancement. In the case of soft pulses, the intensity curve has a smooth dependence on ν_{CPMG}. Another interesting finding is that decoupling has affects the CPMG experiments. In particular, there is no gain in the signal when the decoupling is on during the mixing time. With the absence of decoupling, the signal has a monotonous growth.

HNCO CPMG experiments showed two main results (chapter 6). First, similar to T_2 CPMG experiments, signal sensitivity was better even at relatively low ν_{CPMG}. Second, H-bonds were observed for larger mixing time values. Moreover, F52-R21 and K27-D14 were seen in all these cases, which confirms the validity of the

experimental results. Moreover, compared to the last experiments, it has become possible to shorten experimental time at least twice (or even five times compared to [42]). The ability to identify H-bonds can help to predict the tertiary structure of proteins.

Lastly, applying the REDOR method helped estimate the order parameter for the hIAPP protein. To do this, test experiments were conducted with SH3 protein where the previous experiment's order parameter values are known. Although hIAPP spectra had poor quality, one can make a statement that assigned residues (including residues in N and C-terminals) have similar behavior, therefore, their order parameters should be almost similar.

Bibliography

[1] E. Pharma, "A step-by-step guide to 1d and 2d nmr interpretation." https://emerypharma.com/blog/a-step-by-step-guide-to-1d-and-2d-nmr-interpretation/, 2023.

[2] V. Higman, "Triple resonance backbone assignment." https://protein-nmr.org.uk/solution-nmr/assignment-theory/triple-resonance-backbone-assignment/, 2023.

[3] D. Pranitha, N. Parthiban, S. Dinakaran, S. Ghosh, D. Banji, and Saikiran, "Solid state nuclear magnetic resonance spectroscopy - a review," *Asian Journal of Pharmaceutical and Clinical Research*, vol. 4, pp. 9–14, 10 2011.

[4] K. Xue, R. Sarkar, Z. Tošner, and B. Reif, "Field and magic angle spinning frequency dependence of proton resonances in rotating solids," *Progress in Nuclear Magnetic Resonance Spectroscopy*, vol. 130-131, pp. 47–61, 2022.

[5] T. Le Marchand, T. Schubeis, M. Bonaccorsi, P. Paluch, D. Lalli, A. J. Pell, L. B. Andreas, K. Jaudzems, J. Stanek, and G. Pintacuda, "1H-Detected Biomolecular NMR under Fast Magic-Angle Spinning," *Chemical Reviews*.

[6] B. Reif, "Lecture notes in solid-state nmr," July 2017.

[7] B. Reif, S. E. Ashbrook, L. Emsley, and M. Hong, "Solid-state nmr spectroscopy," *Nature Reviews Methods Primers*, vol. 1, no. 1, p. 2, 2021.

[8] A. C. Sauerwein and D. F. Hansen, *Relaxation Dispersion NMR Spectroscopy*, pp. 75–132. Boston, MA: Springer US, 2015.

[9] E. L. Hahn, "Spin echoes," *Phys. Rev.*, vol. 80, pp. 580–594, Nov 1950.

[10] H. Y. Carr and E. M. Purcell, "Effects of diffusion on free precession in nuclear magnetic resonance experiments," *Phys. Rev.*, vol. 94, pp. 630–638, May 1954.

[11] R. Ishima and S. Bagby, "Protein dynamics revealed by CPMG dispersion," *Journal: Modern Magnetic Resonance*, pp. 1–19, 2016.

[12] J. P. Loria, M. Rance, and A. G. Palmer, "A relaxation-compensated carr-purcell-meiboom-gill sequence for characterizing chemical exchange by nmr spectroscopy," *Journal of the American Chemical Society*, vol. 121, no. 10, pp. 2331–2332, 1999.

[13] D. F. Hansen, P. Vallurupalli, and L. E. Kay, "An improved 15n relaxation dispersion experiment for the measurement of millisecond time-scale dynamics in proteins," *The journal of physical chemistry B*, vol. 112, no. 19, pp. 5898–5904, 2008.

[14] T. Horiuchi, M. Takahashi, J. Kikuchi, S. Yokoyama, and H. Maeda, "Effect of dielectric properties of solvents on the quality factor for a beyond 900 mhz cryogenic probe model," *Journal of Magnetic Resonance*, vol. 174, no. 1, pp. 34–42, 2005.

[15] D. Gadian and F. Robinson, "Radiofrequency losses in nmr experiments on electrically conducting samples," *Journal of Magnetic Resonance (1969)*, vol. 34, no. 2, pp. 449–455, 1979.

[16] B. Jiang, B. Yu, X. Zhang, M. Liu, and D. Yang, "A 15n cpmg relaxation dispersion experiment more resistant to resonance offset and pulse imperfection," *Journal of Magnetic Resonance*, vol. 257, pp. 1–7, 2015.

[17] V. Tugarinov, P. M. Hwang, J. E. Ollerenshaw, and L. E. Kay, "Cross-correlated relaxation enhanced 1h- 13c nmr spectroscopy of methyl groups in very high molecular weight proteins and protein complexes," *Journal of the American Chemical Society*, vol. 125, no. 34, pp. 10420–10428, 2003.

[18] F. A. Mulder, B. Hon, A. Mittermaier, F. W. Dahlquist, and L. E. Kay, "Slow internal dynamics in proteins: application of nmr relaxation dispersion spectroscopy to methyl groups in a cavity mutant of t4 lysozyme," *Journal of the American Chemical Society*, vol. 124, no. 7, pp. 1443–1451, 2002.

[19] E. Brunner, D. Freude, B. Gerstein, and H. Pfeifer, "Residual linewidths of nmr spectra of spin-12 systems under magic-angle spinning," *Journal of Magnetic Resonance (1969)*, vol. 90, no. 1, pp. 90–99, 1990.

[20] A. Samoson, T. Tuherm, and Z. Gan, "High-field high-speed mas resolution enhancement in 1h nmr spectroscopy of solids," *Solid state nuclear magnetic resonance*, vol. 20, no. 3-4, pp. 130–136, 2001.

[21] V. Chevelkov, K. Rehbein, A. Diehl, and B. Reif, "Ultrahigh resolution in proton solid-state nmr spectroscopy at high levels of deuteration," *Angewandte Chemie International Edition*, vol. 45, no. 23, pp. 3878–3881, 2006.

[22] V. Agarwal, K. Faelber, P. Schmieder, and B. Reif, "High-resolution double-quantum deuterium magic angle spinning solid-state nmr spectroscopy of perdeuterated proteins," *Journal of the American Chemical Society*, vol. 131, no. 1, pp. 2–3, 2009.

[23] D. VanderHart, W. L. Earl, and A. Garroway, "Resolution in 13c nmr of organic solids using high-power proton decoupling and magic-angle sample spinning," *Journal of Magnetic Resonance (1969)*, vol. 44, no. 2, pp. 361–401, 1981.

[24] R. Linser, R. Sarkar, A. Krushelnitzky, A. Mainz, and B. Reif, "Dynamics in the solid-state: perspectives for the investigation of amyloid aggregates, membrane proteins and soluble protein complexes," *Journal of biomolecular NMR*, vol. 59, no. 1, pp. 1–14, 2014.

[25] M. Barfield, "Structural dependencies of interresidue scalar coupling h3 j nc 'and donor 1h chemical shifts in the hydrogen bonding regions of proteins," *Journal of the American Chemical Society*, vol. 124, no. 15, pp. 4158–4168, 2002.

[26] M. Hennig and B. H. Geierstanger, "Direct detection of a histidine- histidine side chain hydrogen bond important for folding of apomyoglobin," *Journal of the American Chemical Society*, vol. 121, no. 22, pp. 5123–5126, 1999.

[27] F. Cordier and S. Grzesiek, "Direct observation of hydrogen bonds in proteins by interresidue 3h j nc 'scalar couplings," *Journal of the American Chemical Society*, vol. 121, no. 7, pp. 1601–1602, 1999.

[28] G. Cornilescu, J.-S. Hu, and A. Bax, "Identification of the hydrogen bonding network in a protein by scalar couplings," *Journal of the American Chemical Society*, vol. 121, no. 12, p. 2949, 1999.

[29] A. J. Dingley, J. E. Masse, R. D. Peterson, M. Barfield, J. Feigon, and S. Grzesiek, "Internucleotide scalar couplings across hydrogen bonds in watson- crick and hoogsteen base pairs of a dna triplex," *Journal of the American Chemical Society*, vol. 121, no. 25, pp. 6019–6027, 1999.

[30] M. Barfield, A. J. Dingley, J. Feigon, and S. Grzesiek, "A dft study of the interresidue dependencies of scalar j-coupling and magnetic shielding in the hydrogen-bonding regions of a dna triplex," *Journal of the American Chemical Society*, vol. 123, no. 17, pp. 4014–4022, 2001.

[31] S. Grzesiek, F. Cordier, V. Jaravine, and M. Barfield, "Insights into biomolecular hydrogen bonds from hydrogen bond scalar couplings," *Progress in Nuclear Magnetic Resonance Spectroscopy*, vol. 45, no. 3, pp. 275–300, 2004.

[32] J. Pople and D. Santry, "A molecular orbital theory of hydrocarbons: I. bond delocalization in paraffins," *Molecular Physics*, vol. 7, no. 3, pp. 269–286, 1964.

[33] H. Benedict, H.-H. Limbach, M. Wehlan, W.-P. Fehlhammer, N. S. Golubev, and R. Janoschek, "Solid state15n nmr and theoretical studies of primary and secondary geometric h/d isotope effects on low-barrier nhn- hydrogen bonds," *Journal of the American Chemical Society*, vol. 120, no. 12, pp. 2939–2950, 1998.

[34] C. Kojima, A. Ono, and M. Kainosho, "Studies of physicochemical properties of nh••• n hydrogen bonds in dna, using selective 15n-labeling and direct 15n 1d nmr," *Journal of Biomolecular NMR*, vol. 18, pp. 269–277, 2000.

[35] V. A. Jaravine, F. Cordier, and S. Grzesiek, "Quantification of h/d isotope effects on protein hydrogen-bonds by h3 j nc and 1 j nc couplings and peptide group 15 n and 13 c chemical shifts," *Journal of biomolecular NMR*, vol. 29, pp. 309–318, 2004.

[36] G. I. Makhatadze, G. M. Clore, and A. M. Gronenborn, "Solvent isotope effect and protein stability," *Nature structural biology*, vol. 2, no. 10, pp. 852–855, 1995.

[37] L. E. Kay, M. Ikura, R. Tschudin, and A. Bax, "Three-dimensional triple-resonance nmr spectroscopy of isotopically enriched proteins," *Journal of Magnetic Resonance (1969)*, vol. 89, no. 3, pp. 496–514, 1990.

[38] M. J. Plevin, D. L. Bryce, and J. Boisbouvier, "Direct detection of ch/π interactions in proteins," *Nature chemistry*, vol. 2, no. 6, pp. 466–471, 2010.

[39] R. Linser, U. Fink, and B. Reif, "Proton-detected scalar coupling based assignment strategies in mas solid-state nmr spectroscopy applied to perdeuterated proteins," *Journal of Magnetic Resonance*, vol. 193, no. 1, pp. 89–93, 2008.

[40] L. Chen, J. M. Kaiser, T. Polenova, J. Yang, C. M. Rienstra, and L. J. Mueller, "Backbone assignments in solid-state proteins using j-based 3d heteronuclear correlation spectroscopy," *Journal of the American Chemical Society*, vol. 129, no. 35, pp. 10650–10651, 2007.

[41] V. Chevelkov, K. Rehbein, A. Diehl, and B. Reif, "Ultrahigh resolution in proton solid-state nmr spectroscopy at high levels of deuteration," *Angewandte Chemie International Edition*, vol. 45, no. 23, pp. 3878–3881, 2006.

[42] P. Schanda, M. Huber, R. Verel, M. Ernst, and B. H. Meier, "Direct Detection of 3hJNC' Hydrogen-Bond Scalar Couplings in Proteins by Solid-State NMR Spectroscopy," *Angewandte Chemie International Edition*, vol. 48, no. 49, pp. 9322–9325, 2009.

[43] M. G. Iadanza, M. P. Jackson, E. W. Hewitt, N. A. Ranson, and S. E. Radford, "A new era for understanding amyloid structures and disease," *Nature Reviews Molecular Cell Biology*, vol. 19, no. 12, pp. 755–773, 2018.

[44] T. P. Knowles, M. Vendruscolo, and C. M. Dobson, "The amyloid state and its association with protein misfolding diseases," *Nature reviews Molecular cell biology*, vol. 15, no. 6, pp. 384–396, 2014.

[45] D. C. Rodriguez Camargo, *Nuclear Magnetic Resonance Characterization of Aggregating Biological Systems and Membrane Proteins*. PhD thesis, Technical University of Munich, 2015.

[46] A. K. Bishoyi, P. H. Roham, K. Rachineni, S. Save, M. A. Hazari, S. Sharma, and A. Kumar, "Human islet amyloid polypeptide (hiapp)-a curse in type ii diabetes mellitus: insights from structure and toxicity studies," *Biological chemistry*, vol. 402, no. 2, pp. 133–153, 2021.

[47] S. Mosselman, J. Höppener, J. Zandberg, A. Van Mansfeld, A. G. Van Kessel, C. Lips, and H. Jansz, "Islet amyloid polypeptide: identification and chromosomal localization of the human gene," *FEBS letters*, vol. 239, no. 2, pp. 227–232, 1988.

[48] S. J. Wimalawansa, "Amylin, calcitonin gene-related peptide, calcitonin, and adrenomedullin: a peptide superfamily," *Critical Reviews™ in Neurobiology*, vol. 11, no. 2-3, 1997.

[49] J. Wang, J. Xu, J. Finnerty, M. Furuta, D. F. Steiner, and C. B. Verchere, "The prohormone convertase enzyme 2 (pc2) is essential for processing pro-islet amyloid polypeptide at the nh2-terminal cleavage site," *Diabetes*, vol. 50, no. 3, pp. 534–539, 2001.

[50] C. E. Higham, R. L. Hull, L. Lawrie, K. I. Shennan, J. F. Morris, N. P. Birch, K. Docherty, and A. Clark, "Processing of synthetic pro-islet amyloid polypeptide (proiapp)'amylin'by recombinant prohormone convertase enzymes, pc2 and pc3, in vitro," *European Journal of Biochemistry*, vol. 267, no. 16, pp. 4998–5004, 2000.

[51] P. Westermark, U. Engström, K. H. Johnson, G. T. Westermark, and C. Betsholtz, "Islet amyloid polypeptide: pinpointing amino acid residues linked to amyloid fibril formation.," *Proceedings of the National Academy of Sciences*, vol. 87, no. 13, pp. 5036–5040, 1990.

[52] J. Höppener, H. Jacobs, N. Wierup, G. Sotthewes, M. Sprong, P. de Vos, R. Berger, F. Sundler, and B. Ahrén, "Human islet amyloid polypeptide transgenic mice: in vivo and ex vivo models for the role of hiapp in type 2 diabetes mellitus," *Experimental diabetes research*, vol. 2008, 2008.

[53] W. M. Macfarlane, S. C. Campbell, L. J. Elrick, V. Oates, G. Bermano, K. J. Lindley, A. Aynsley-Green, M. J. Dunne, R. F. James, and K. Docherty, "Glucose regulates islet amyloid polypeptide gene transcription in a pdx1-and calcium-dependent manner," *Journal of Biological Chemistry*, vol. 275, no. 20, pp. 15330–15335, 2000.

[54] W. M. Macfarlane, S. B. Smith, R. F. James, A. D. Clifton, Y. N. Doza, P. Cohen, and K. Docherty, "The p38/reactivating kinase mitogen-activated

protein kinase cascade mediates the activation of the transcription factor insulin upstream factor 1 and insulin gene transcription by high glucose in pancreatic β-cells," *Journal of Biological Chemistry*, vol. 272, no. 33, pp. 20936–20944, 1997.

[55] T. D. O'Brien, P. Westermark, and K. H. Johnson, "Islet amyloid polypeptide and insulin secretion from isolated perfused pancreas of fed, fasted, glucose-treated, and dexamethasone-treated rats," *Diabetes*, vol. 40, no. 12, pp. 1701–1706, 1991.

[56] H. Mulder, B. Ahrén, and F. Sundler, "Differential expression of islet amyloid polypeptide (amylin) and insulin in experimental diabetes in rodents," *Molecular and cellular endocrinology*, vol. 114, no. 1-2, pp. 101–109, 1995.

[57] T. A. Lutz, "Control of energy homeostasis by amylin," *Cellular and molecular life sciences*, vol. 69, pp. 1947–1965, 2012.

[58] G. Paxinos, S. Y. Chai, G. Christopoulos, X.-F. Huang, A. W. Toga, H. Wang, and P. M. Sexton, "In vitro autoradiographic localization of calcitonin and amylin binding sites in monkey brain," *Journal of chemical neuroanatomy*, vol. 27, no. 4, pp. 217–236, 2004.

[59] X.-X. Zhang, Y.-H. Pan, Y.-M. Huang, and H.-L. Zhao, "Neuroendocrine hormone amylin in diabetes," *World journal of diabetes*, vol. 7, no. 9, p. 189, 2016.

[60] M. Visa, G. Alcarraz-Vizán, J. Montane, L. Cadavez, C. Castaño, M. L. Villanueva-Peñacarrillo, J.-M. Servitja, and A. Novials, "Islet amyloid polypeptide exerts a novel autocrine action in β-cell signaling and proliferation," *The FASEB Journal*, vol. 29, no. 7, pp. 2970–2979, 2015.

[61] P. Y. Wielinga, C. Löwenstein, S. Muff, M. Munz, S. C. Woods, and T. A. Lutz, "Central amylin acts as an adiposity signal to control body weight and energy expenditure," *Physiology & behavior*, vol. 101, no. 1, pp. 45–52, 2010.

[62] C. N. Boyle, T. A. Lutz, and C. Le Foll, "Amylin–its role in the homeostatic and hedonic control of eating and recent developments of amylin analogs to treat obesity," *Molecular metabolism*, vol. 8, pp. 203–210, 2018.

[63] R. Hu, B. Ren, M. Zhang, H. Chen, Y. Liu, L. Liu, X. Gong, B. Jiang, J. Ma, and J. Zheng, "Seed-induced heterogeneous cross-seeding self-assembly of human and rat islet polypeptides," *ACS omega*, vol. 2, no. 3, pp. 784–792, 2017.

[64] S. B. Padrick and A. D. Miranker, "Islet amyloid: phase partitioning and secondary nucleation are central to the mechanism of fibrillogenesis," *Biochemistry*, vol. 41, no. 14, pp. 4694–4703, 2002.

[65] E. Chatani and N. Yamamoto, "Recent progress on understanding the mechanisms of amyloid nucleation," *Biophysical reviews*, vol. 10, no. 2, pp. 527–534, 2018.

[66] D. Radovan, V. Smirnovas, and R. Winter, "Effect of pressure on islet amyloid polypeptide aggregation: revealing the polymorphic nature of the fibrillation process," *Biochemistry*, vol. 47, no. 24, pp. 6352–6360, 2008.

[67] R. Kayed, J. Bernhagen, N. Greenfield, K. Sweimeh, H. Brunner, W. Voelter, and A. Kapurniotu, "Conformational transitions of islet amyloid polypeptide (iapp) in amyloid formation in vitro," *Journal of molecular biology*, vol. 287, no. 4, pp. 781–796, 1999.

[68] D. C. Rodriguez Camargo, K. Tripsianes, K. Buday, A. Franko, C. Göbl, C. Hartlmüller, R. Sarkar, M. Aichler, G. Mettenleiter, M. Schulz, *et al.*, "The redox environment triggers conformational changes and aggregation of hiapp in type ii diabetes," *Scientific reports*, vol. 7, no. 1, p. 44041, 2017.

[69] E. T. Jaikaran and A. Clark, "Islet amyloid and type 2 diabetes: from molecular misfolding to islet pathophysiology," *Biochimica et Biophysica Acta (BBA)-Molecular Basis of Disease*, vol. 1537, no. 3, pp. 179–203, 2001.

[70] E. T. Jaikaran, C. E. Higham, L. C. Serpell, J. Zurdo, M. Gross, A. Clark, and P. E. Fraser, "Identification of a novel human islet amyloid polypeptide β-sheet domain and factors influencing fibrillogenesis," *Journal of molecular biology*, vol. 308, no. 3, pp. 515–525, 2001.

[71] S. Bedrood, Y. Li, J. M. Isas, B. G. Hegde, U. Baxa, I. S. Haworth, and R. Langen, "Fibril structure of human islet amyloid polypeptide," *Journal of Biological Chemistry*, vol. 287, no. 8, pp. 5235–5241, 2012.

[72] S. Luca, W.-M. Yau, R. Leapman, and R. Tycko, "Peptide conformation and supramolecular organization in amylin fibrils: constraints from solid-state nmr," *Biochemistry*, vol. 46, no. 47, pp. 13505–13522, 2007.

[73] J. M. Griffiths, T. T. Ashburn, M. Auger, P. R. Costa, R. G. Griffin, and P. T. Lansbury Jr, "Rotational resonance solid-state nmr elucidates a structural model of pancreatic amyloid," *Journal of the American Chemical Society*, vol. 117, no. 12, pp. 3539–3546, 1995.

[74] J. T. Nielsen, M. Bjerring, M. D. Jeppesen, R. O. Pedersen, J. M. Pedersen, K. L. Hein, T. Vosegaard, T. Skrydstrup, D. E. Otzen, and N. C. Nielsen, "Unique identification of supramolecular structures in amyloid fibrils by solid-state nmr spectroscopy," *Angewandte Chemie*, vol. 121, no. 12, pp. 2152–2155, 2009.

[75] Q. Cao, D. R. Boyer, M. R. Sawaya, P. Ge, and D. S. Eisenberg, "Cryo-em structure and inhibitor design of human iapp (amylin) fibrils," *Nature structural & molecular biology*, vol. 27, no. 7, pp. 653–659, 2020.

[76] Y. LI and J. N. EVANS, "The importance of xy-8 phase cycling in the rotational-echo double-resonance experiment with total sideband suppression," *Journal of Magnetic Resonance, Series A*, vol. 116, no. 2, pp. 150–155, 1995.

[77] Y. Li and J. N. Evans, "The importance of xy-8 phase cycling in the rotational-echo double-resonance experiment with total sideband suppression," *Journal of Magnetic Resonance, Series A*, vol. 116, no. 2, pp. 150–155, 1995.

[78] D. Gołowicz, P. Kasprzak, V. Orekhov, and K. Kazimierczuk, "Fast time-resolved nmr with non-uniform sampling," *Progress in Nuclear Magnetic Resonance Spectroscopy*, vol. 116, pp. 40–55, 2020.

[79] L. Schrödinger and W. DeLano, "Pymol."

[80] W. Lee, M. Rahimi, Y. Lee, and A. Chiu, "POKY: a software suite for multidimensional NMR and 3D structure calculation of biomolecules," *Bioinformatics*, vol. 37, pp. 3041–3042, 03 2021.

[81] P. Schanda, B. H. Meier, and M. Ernst, "Quantitative analysis of protein backbone dynamics in microcrystalline ubiquitin by solid-state nmr spectroscopy,"

Journal of the American Chemical Society, vol. 132, no. 45, pp. 15957–15967, 2010.

[82] V. Chevelkov, U. Fink, and B. Reif, "Accurate determination of order parameters from 1h, 15n dipolar couplings in mas solid-state nmr experiments," *Journal of the American Chemical Society*, vol. 131, no. 39, pp. 14018–14022, 2009.

[83] D. W. Juhl, Z. Tošner, and T. Vosegaard, "Versatile nmr simulations using simpson," in *Annual Reports on NMR Spectroscopy*, vol. 100, pp. 1–59, Elsevier, 2020.

Appendix A

R_2 CPMG 60 msec evolution time using soft pulses

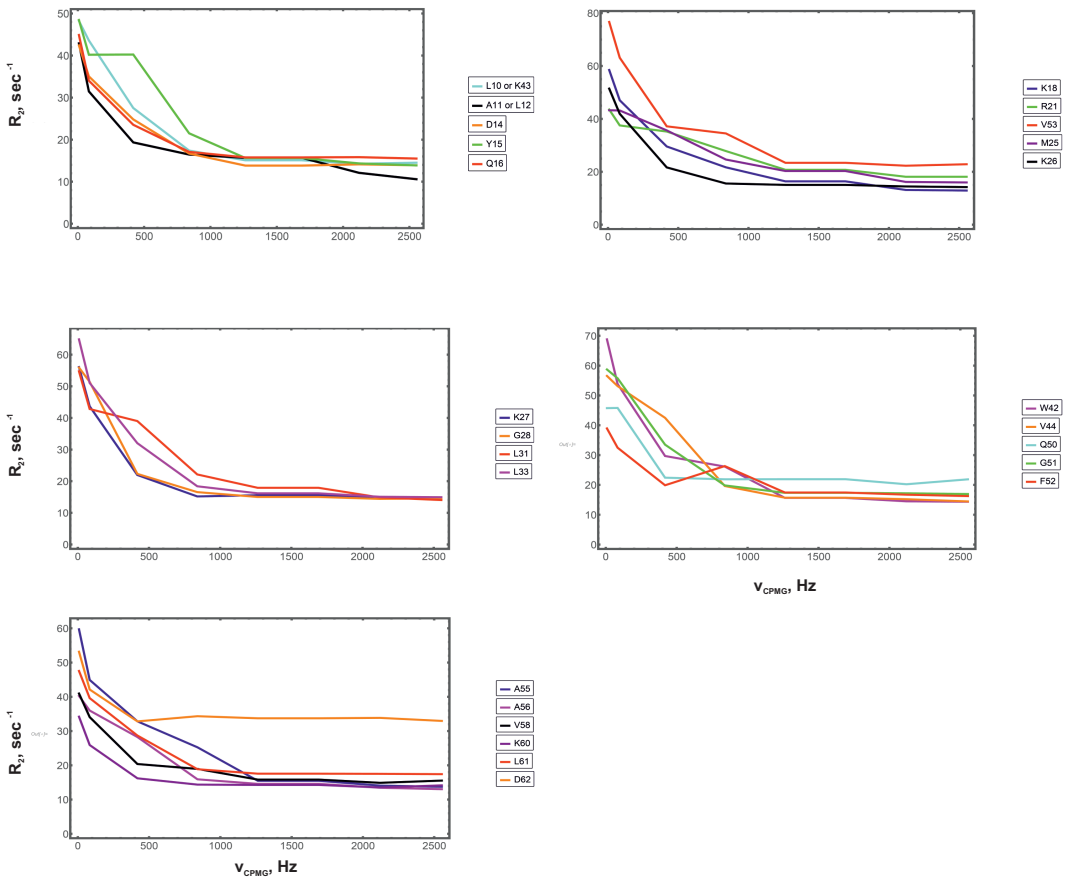

Figure A.1: *R_2 CPMG 60 msec.*

Appendix B

H-bonds detected at 4T=132 msec mixing time in conventional experiments

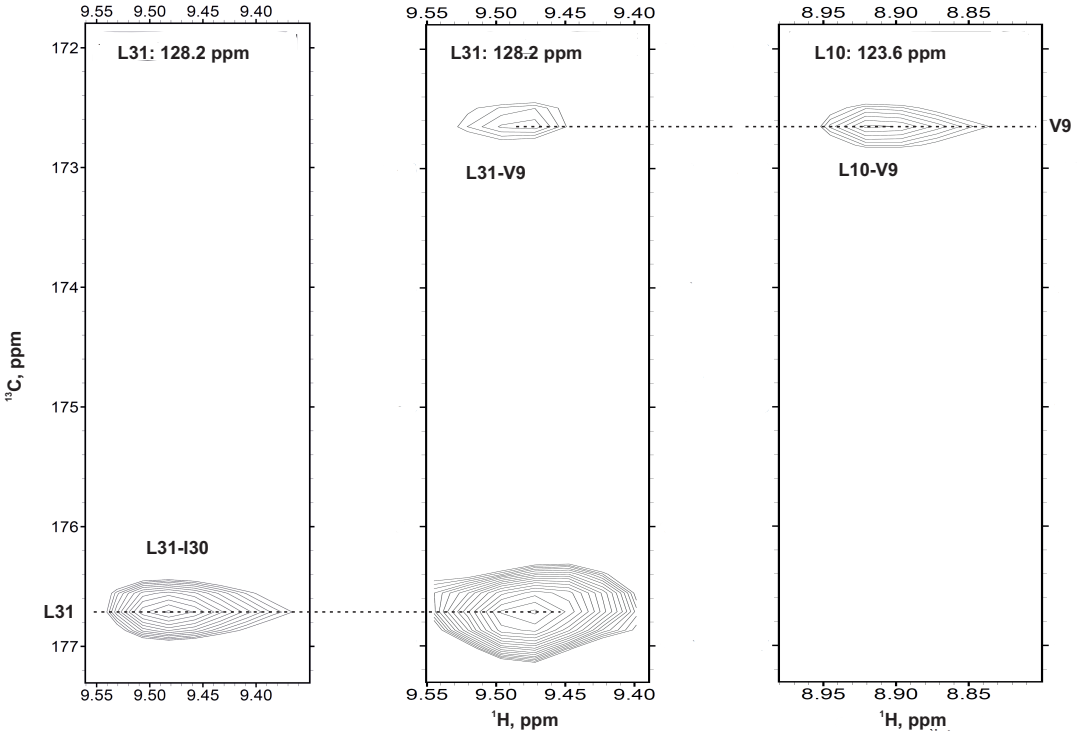

Figure B.1: *HNCO conventional L31-V9 H-bond.*

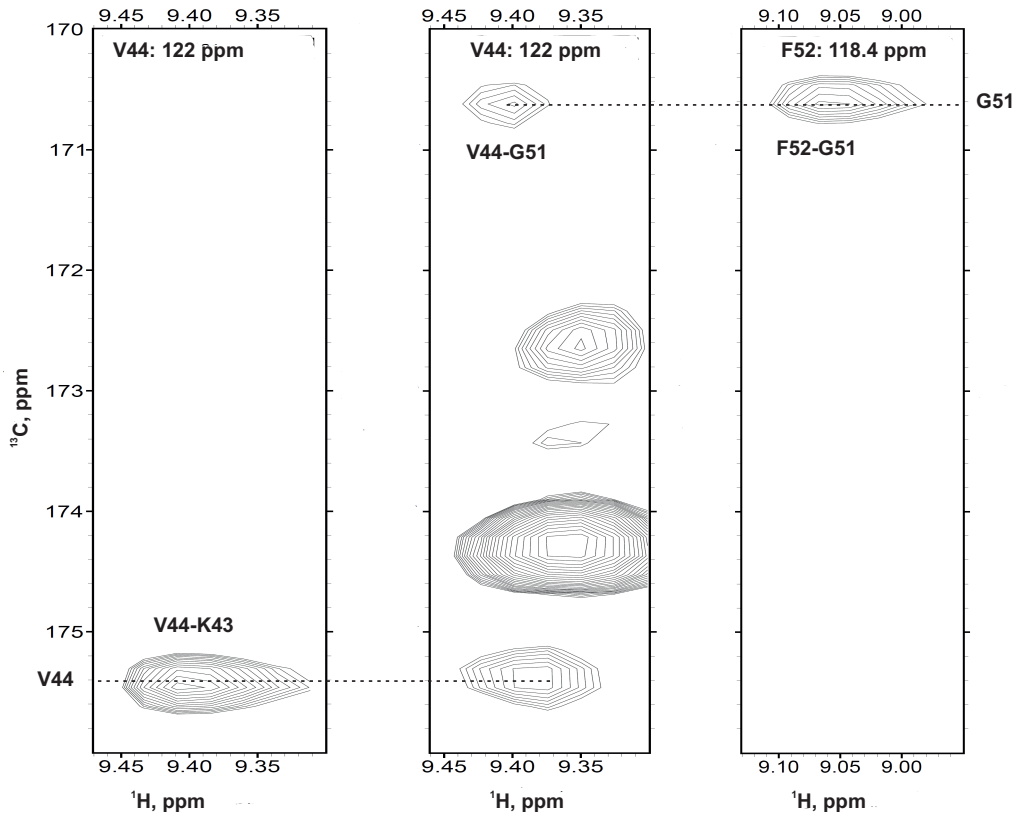

Figure B.2: *HNCO conventional V44-G51 H-bond.*

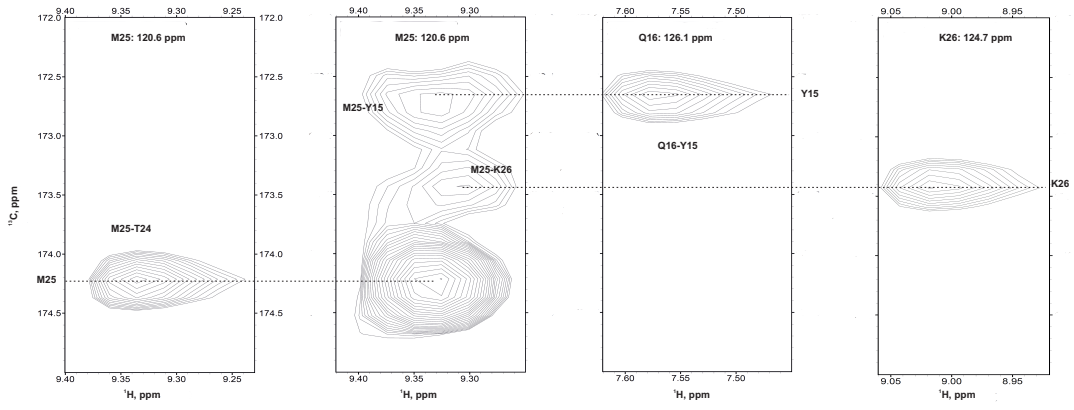

Figure B.3: *HNCO conventional M25-Y15 H-bond.*

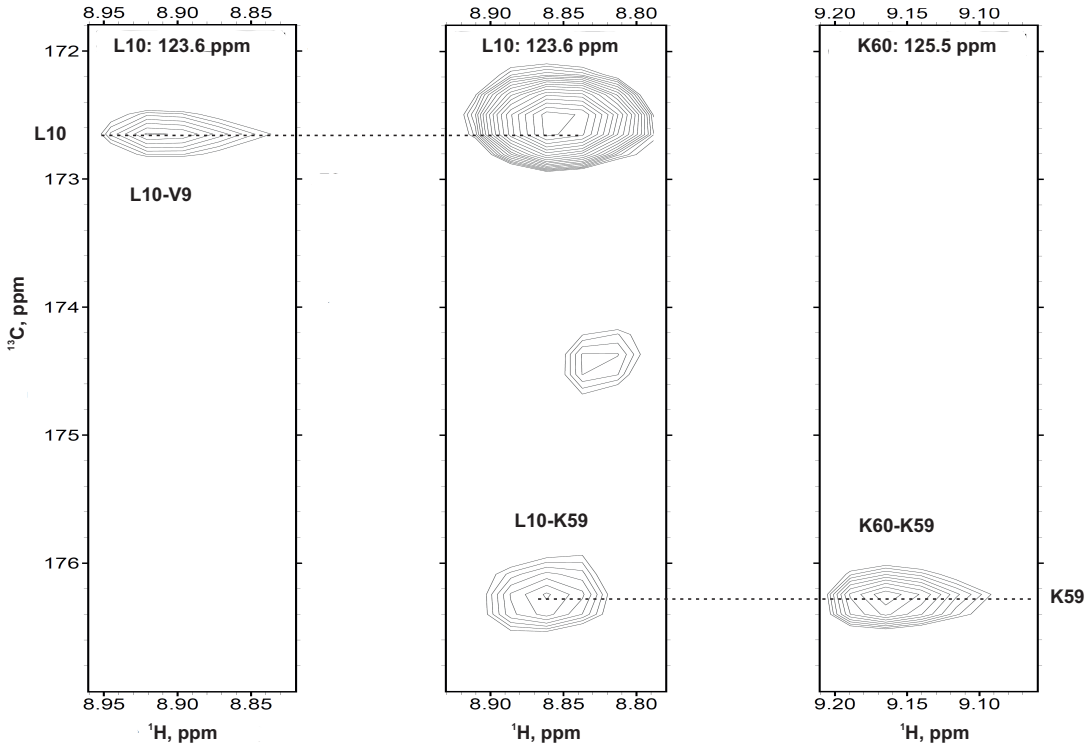

Figure B.4: *HNCO conventional L10-K59 H-bond.*

Appendix C

H-bonds detected at 4T=132 msec mixing time in CPMG based experiments

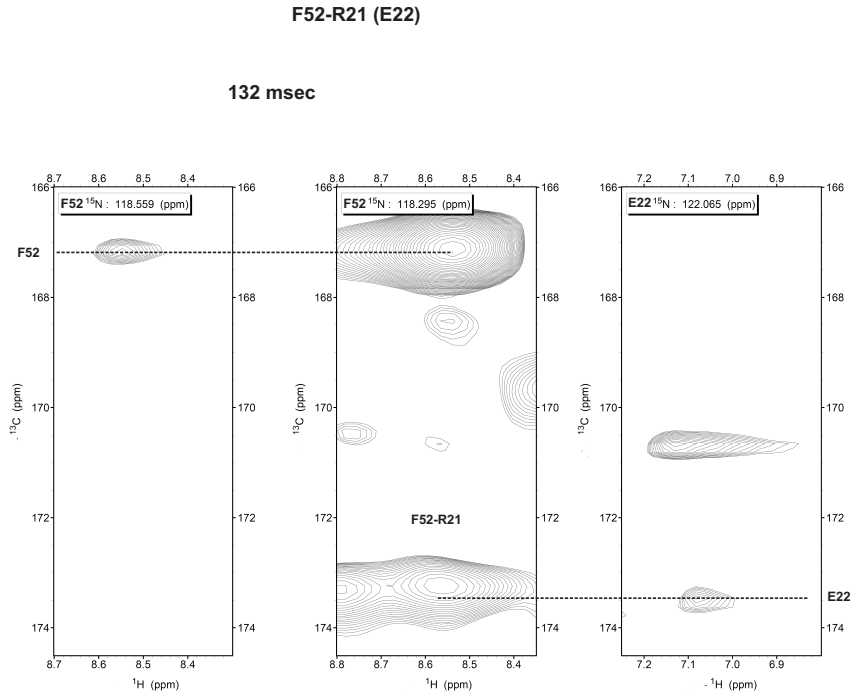

Figure C.1: *HNCO CPMG F52-R21 H-bond detected at 4T=132 msec mixing time.*

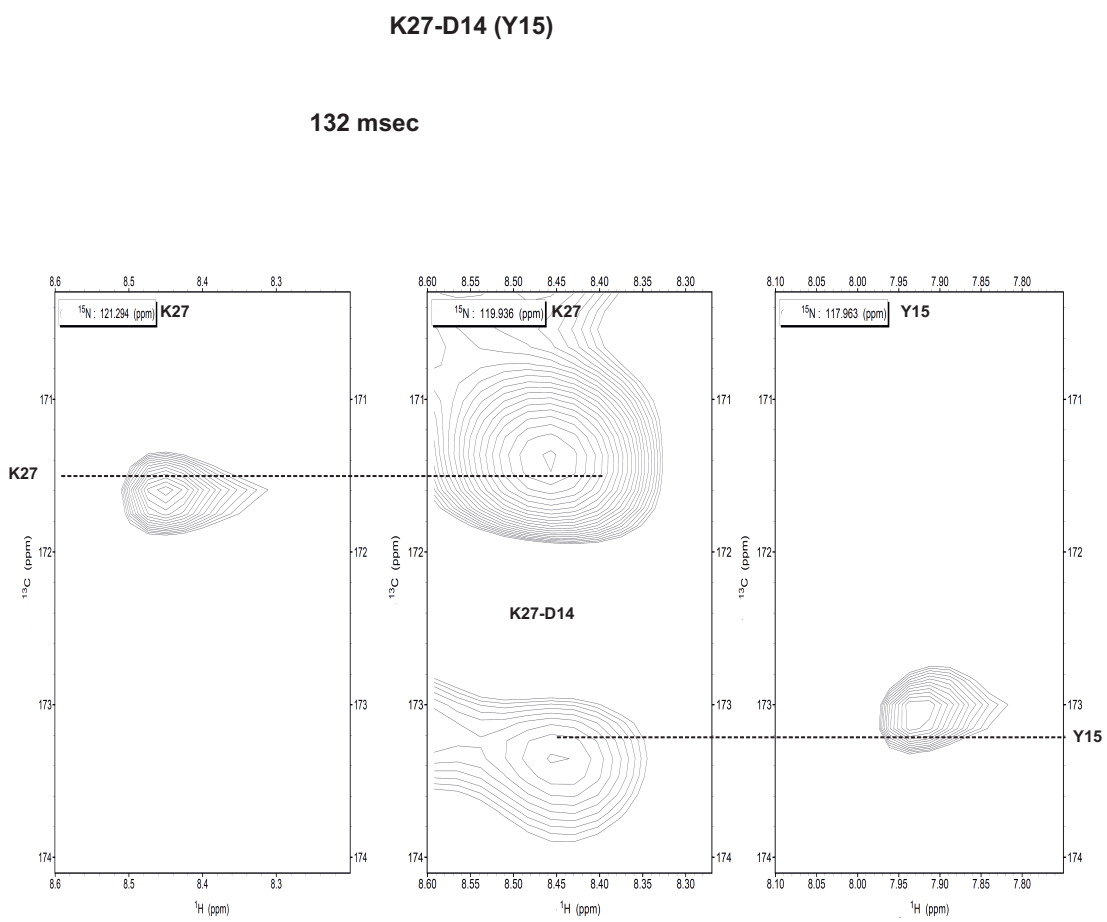

Figure C.2: *HNCO CPMG K27-D14 H-bond detected at 4T=132 msec mixing time.*

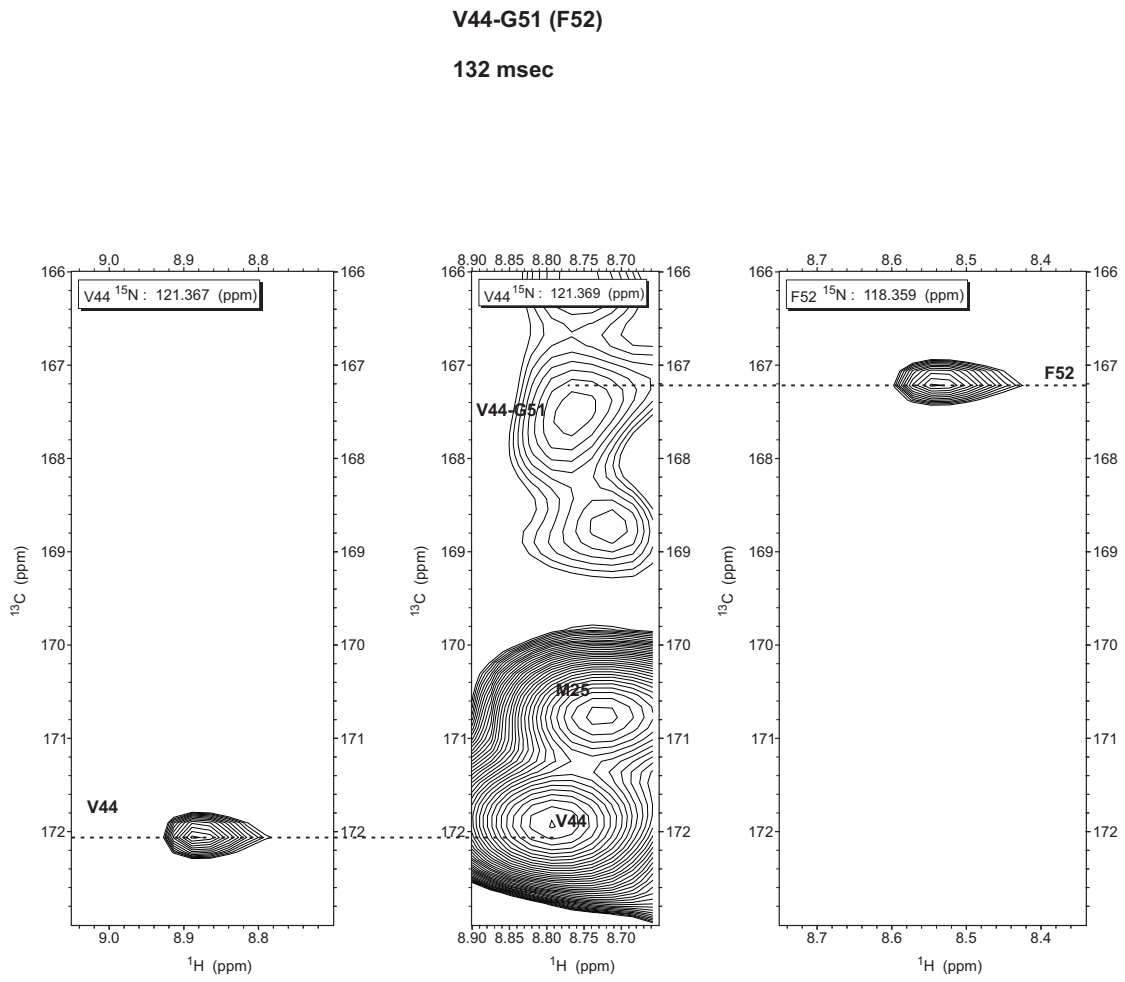

Figure C.3: *HNCO CPMG V44-G51 H-bond detected at 4T=132 msec mixing time.*

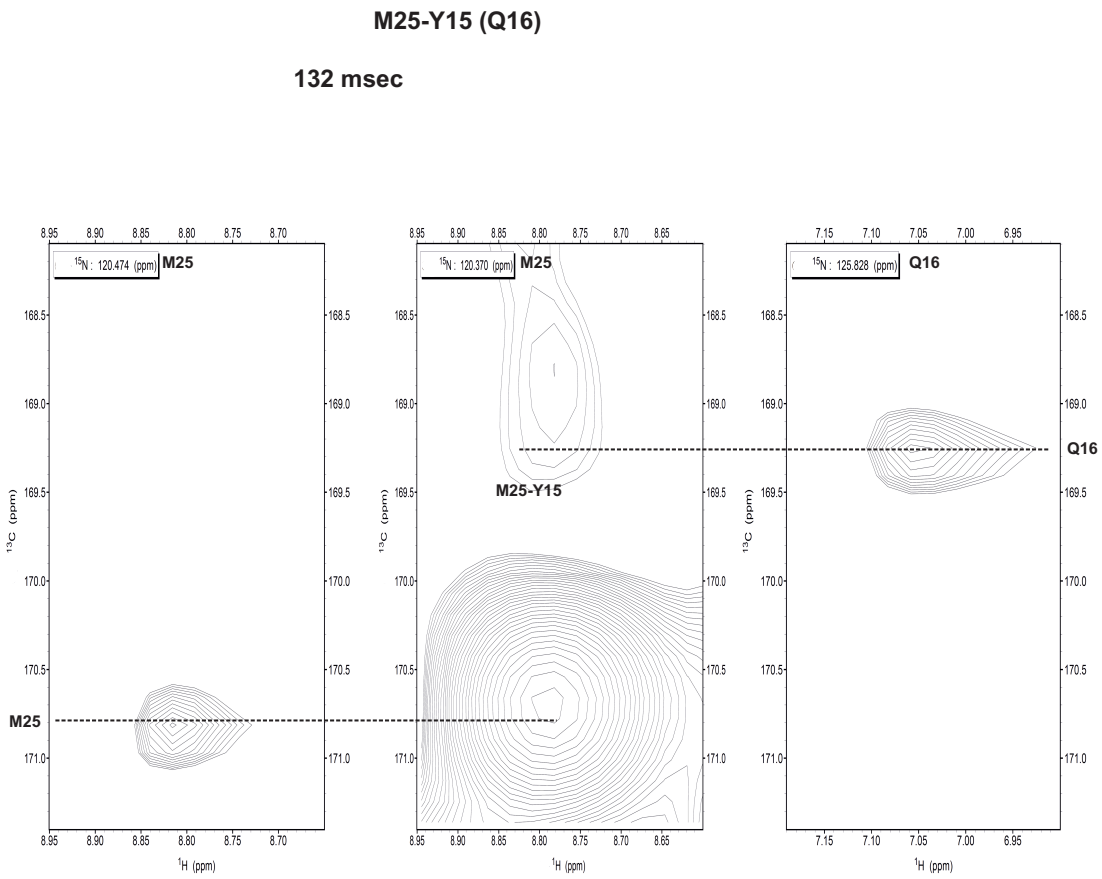

Figure C.4: *HNCO CPMG M25-Y15 H-bond detected at 4T=132 msec mixing time.*

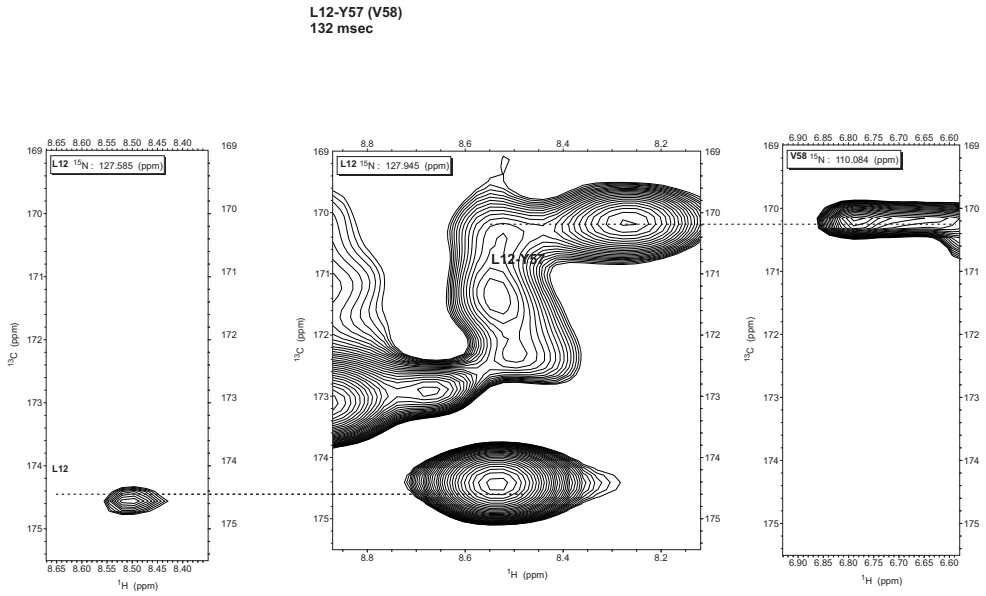

Figure C.5: *HNCO CPMG L12-Y57 H-bond detected at 4T=132 msec mixing time.*

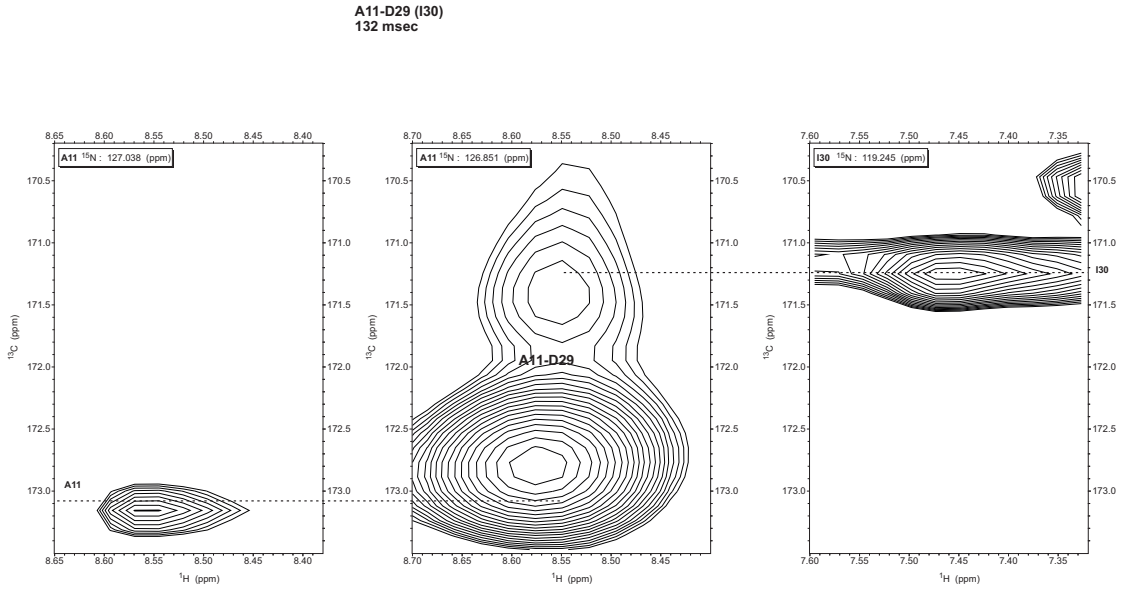

Figure C.6: *HNCO CPMG A11-D29 H-bond detected at 4T=132 msec mixing time.*

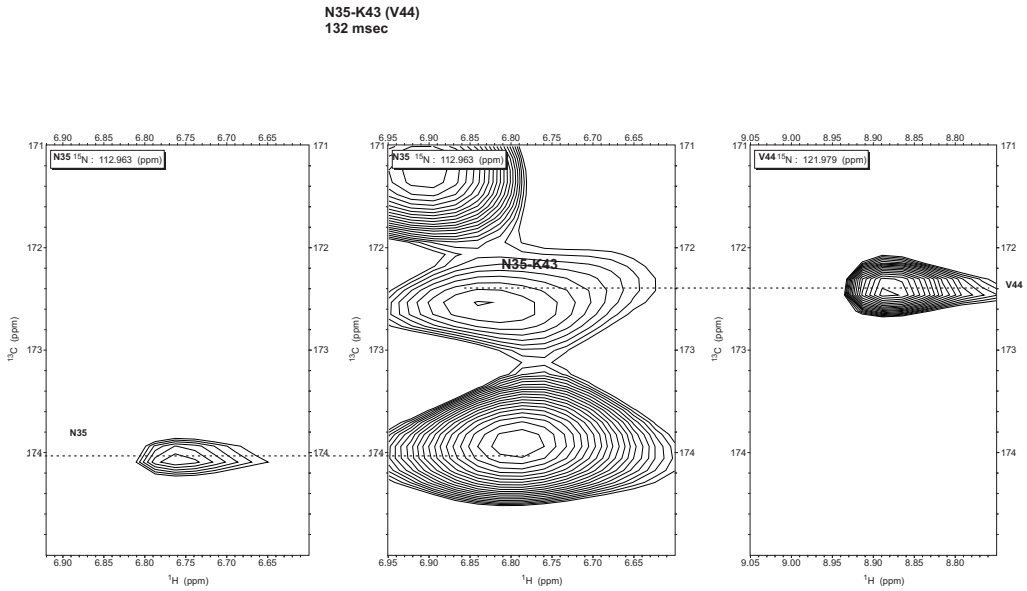

Figure C.7: *HNCO CPMG N35-K43 H-bond detected at 4T=132 msec mixing time.*

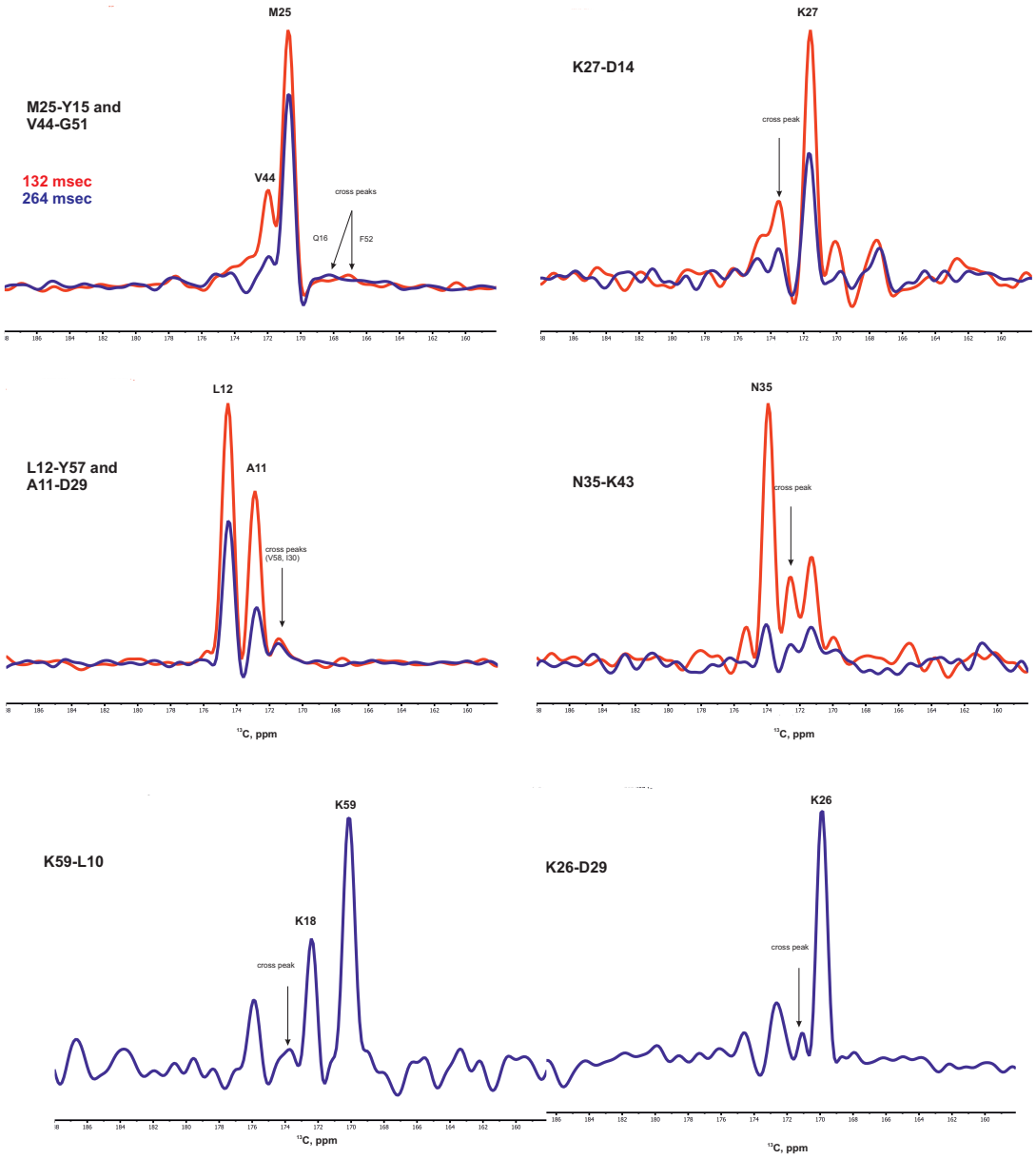

Figure C.8: *1D traces of H-bonds detected at 4T=132 msec (red) and 4T=264 msec (blue) mixing times.*

Appendix D

REDOR curves

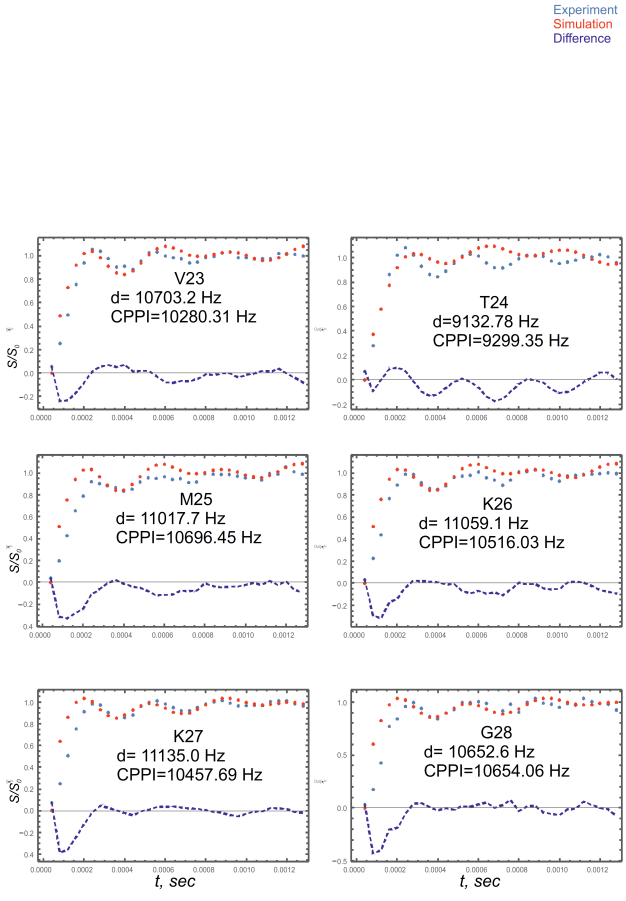

Figure D.1: *REDOR curves of SH3 residues. Part 1.*

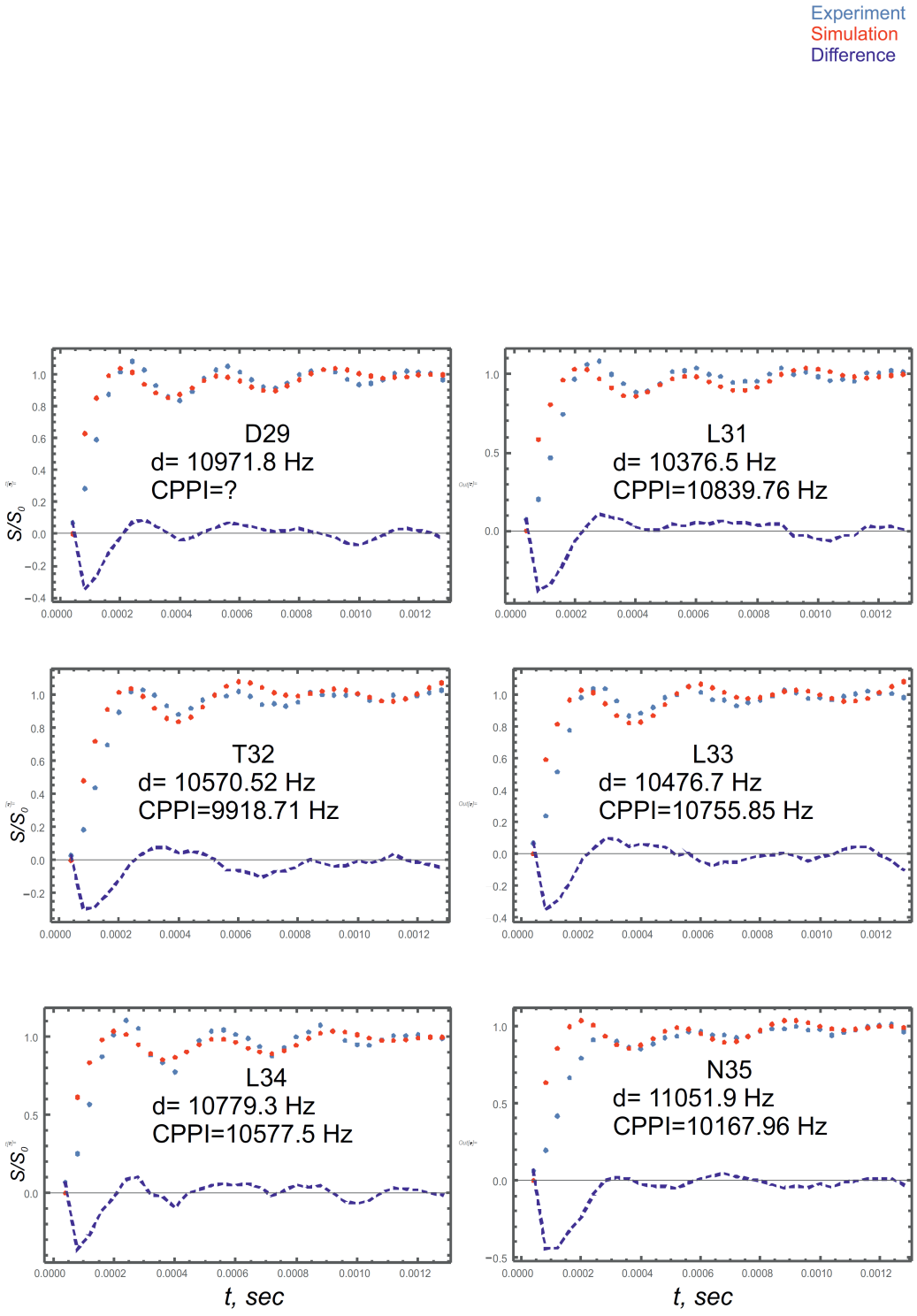

Figure D.2: *REDOR curves of SH3 residues. Part 2.*

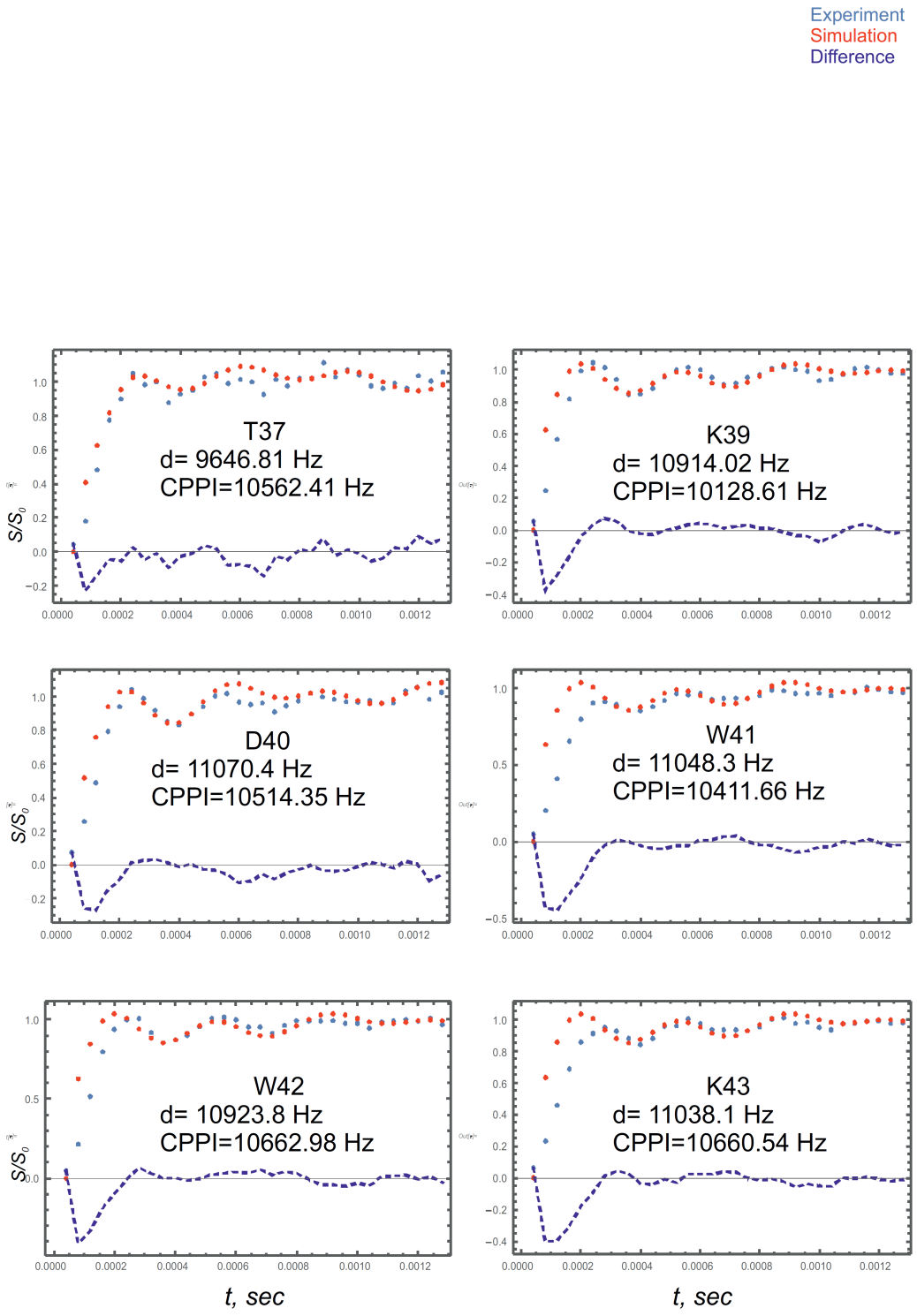

Figure D.3: *REDOR curves of SH3 residues. Part 3.*

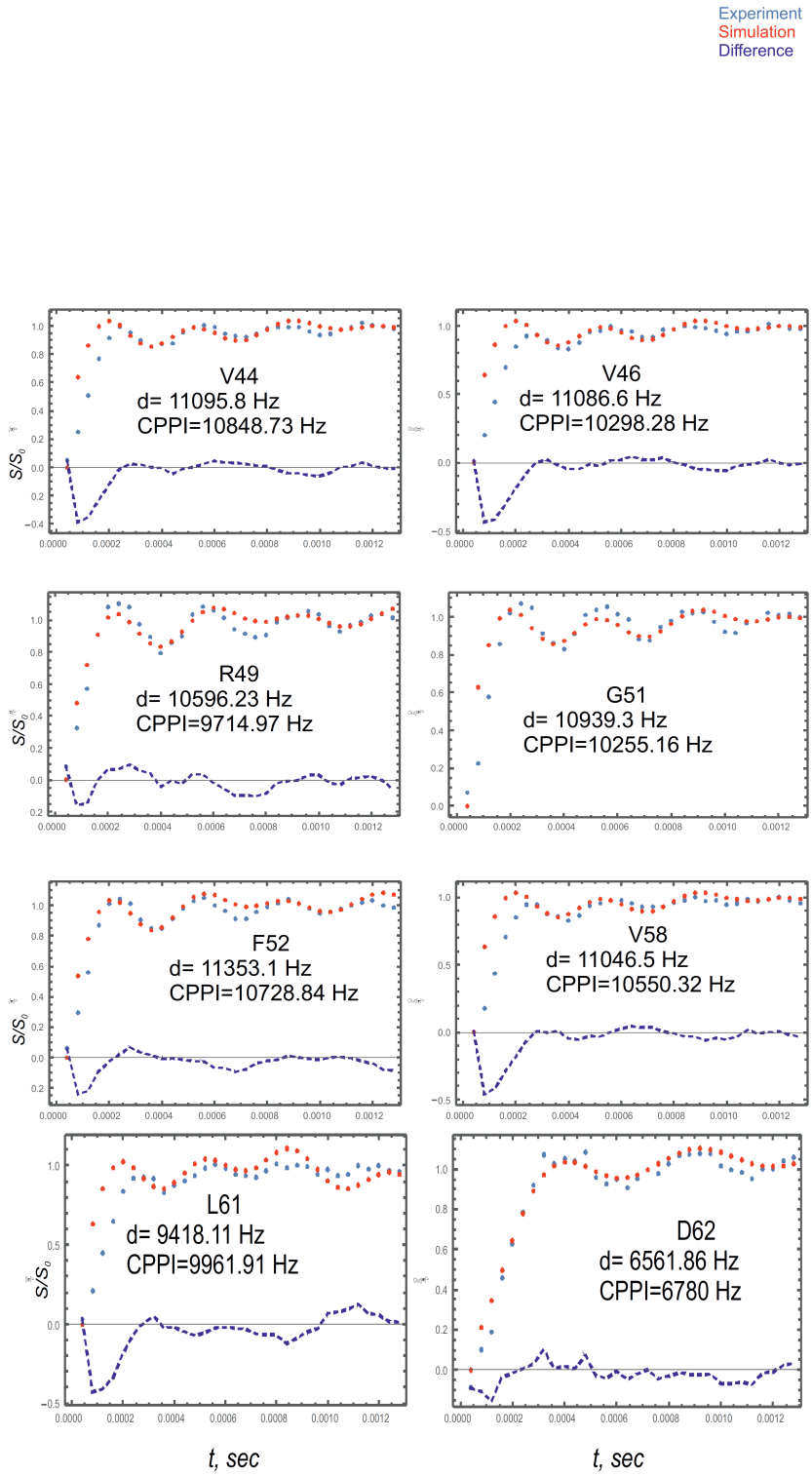

Figure D.4: *REDOR curves of SH3 residues. Part 4.*

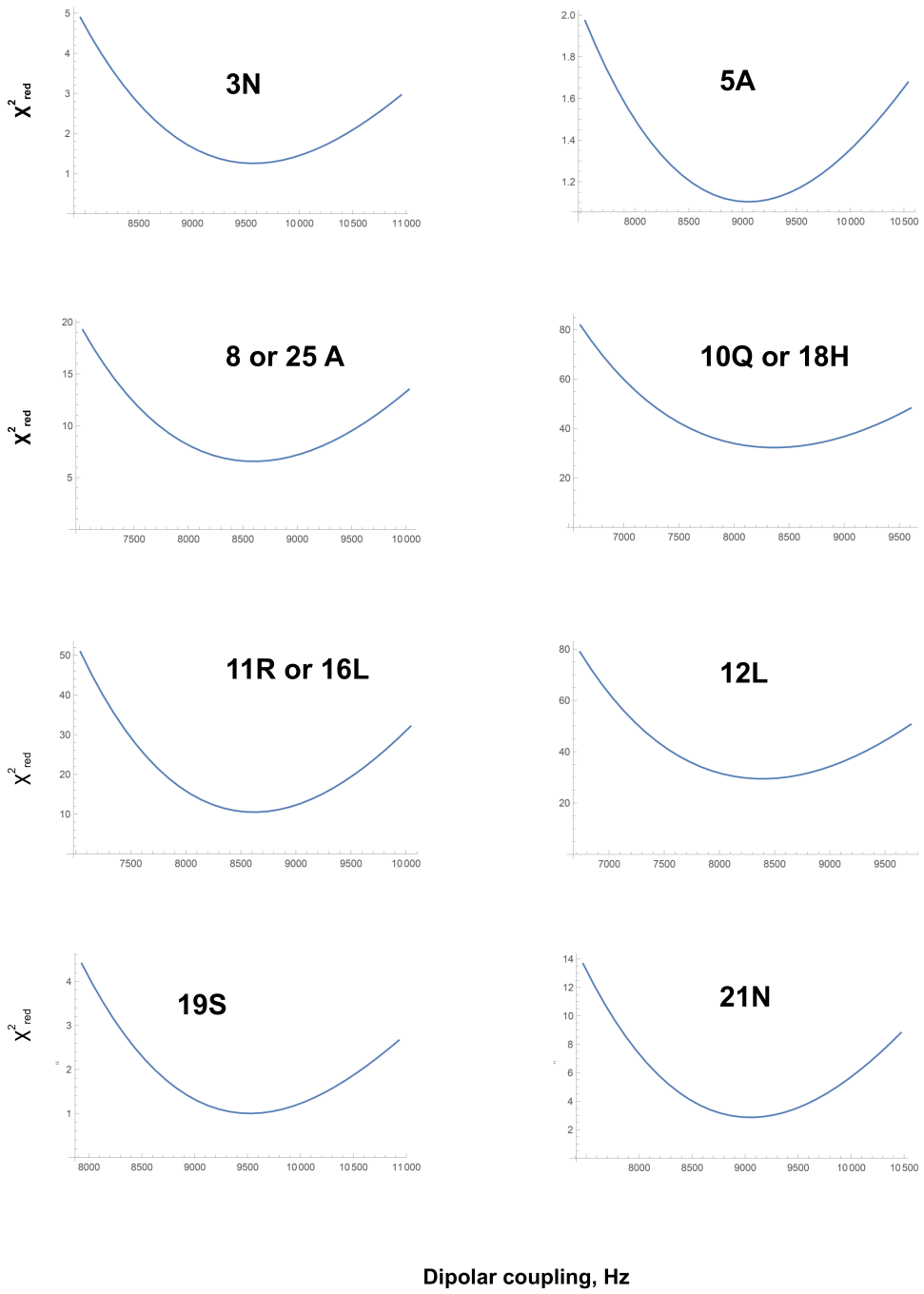

Figure D.5: *Dependance of reduced chi squared parameter as a function of dipolar coupling. Part 1.*

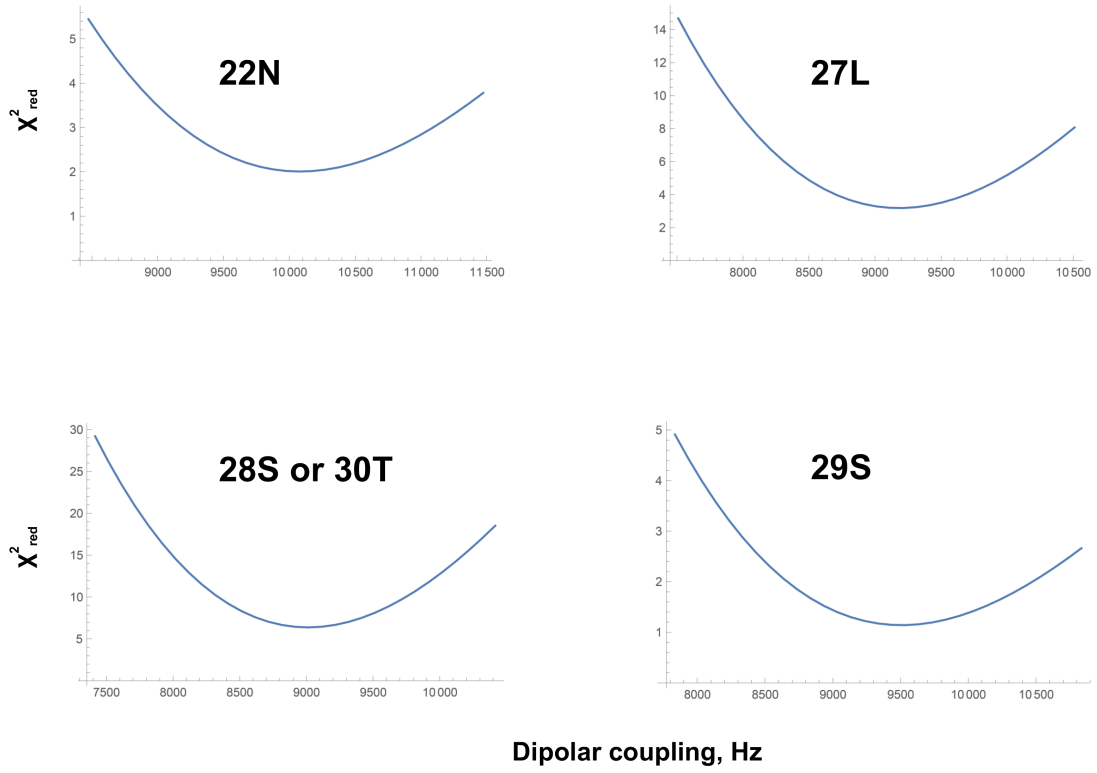

Figure D.6: *Dependance of reduced chi squared parameter as a function of dipolar coupling. Part 2.*

Appendix E

Pulse sequence for T_2 CPMG experiment

```
#include <Avancesolids.incl>
;cnst11 : to adjust t=0 for acquisition, if digmod = baseopt
"acqt0=1u*cnst11"
"in0=inf1"
"in30=inf1"
define delay TAU
"TAU=(1s/(4*cnst24))-larger(p1*2, p7*2)/2"


define delay delta
"delta=((d23/2)/10)-p7"

1 ze
2 d1 do:f2 do:f3
#include <p15_prot.incl>
#include <aq_prot.incl>

(p1 pl1 ph1):f1
(p25:sp42 ph10):f1  (p25:sp43 ph2):f2
#########################
; t1 evolution of 15N;
```

```
;#######################

0.5u pl12:f1
0.5u cpds1:f1

(center (d0) (p3*2 ph0 pl11):f3)
1u do:f1


; spin echo evolution with train pulses d23 is assumed to be any,

3 delta
(p7*2 pl7 ph17):f2
delta
lo to 3 times l0

;#######################


(p21 pl21 ph7):f2
0.5u pl13:f1
0.5u cpds4:f1
d30*0.25
1u do:f1
1u cpds5:f1
d30*0.25
1u do:f1
1u cpds5:f1
d30*0.25
1u do:f1
1u cpds4:f1
d30*0.25
1u do:f1
(p23 pl21 ph8):f2
;;;;;;;;;;;;;;;; water suppression block ends
```

```
(p25:sp42 ph11):f1  (p25:sp43 ph9):f2
1u cpds2:f2 cpds3:f3
go=2 ph31
1m do:f2 do:f3
10m mc #0 to 2 F1PH(ip2,id0)

HaltAcqu, 1m  ;jump address for protection files
exit
ph0=0
ph1  = 1 3
ph10 = 0
ph2 =  1
;ph5 =  2
;ph6 =  0
ph7 =  0
ph8= 0 0 2 2
ph17= 1
;ph18=2
ph9= 1
ph11 = 1 1 1 1 3 3 3 3
ph31 = 1 3 3 1 3 1 1 3
```

Appendix F

Pulse sequence for HNCO CPMG experiment

```
;********channel specifications*************
;1H : f1 or H (when HNC_defs.incl is used)
;15N : f2 or N (when HNC_defs.incl is used)
;13C : f3 or C (when HNC_defs.incl is used)

;************************** pulse lengths ***********
;p1 : at pl1 1H hard pulse
;p2 : at pl2 15N hard pulse
;p3 : at pl3 13C hard pulse
;p6 : at pl6 15N soft pulse
;p5 : at pl5 13C soft pulse

;********************constants ***************
;cnst5 : J(NH)= 90Hz
;cnst6 : J(NCO)= 15Hz (can vary)
;cnst30 : MAS rate Hz
;cnst25 : CO chemical shift 175 ppm
;cnst26 : Ca chemical shift 55 ppm

;********************CPDs ***********
```

```
;cpdprg1 : 1H sltppm power = 0.25*MAS, pcpd= 2*t_MAS
;cpdprg2 : 15N Waltz16_pl16 25us pcpd
;cpdprg3 : 13C Waltz16_pl17 25us pcpd

;*****************shaped pulses **********
;spnam18 : pi pulse Ca Q3.2000 normally 200us
;spnam19 : pi pulse CO Q3.2000 normally 200us
;spnam20 : pi/2 pulse Ca rect
;spnam21 : pi/2 pulse CO rect

;********delays**********
;d3 : 1/(4*JNH)
;d5 : 8-15ms NC evolution

;#############################;;;;;;;;;

#include <Delay.incl>

prosol relations=<biosolHCN>

#include <HNC_defs.incl>
; defines H:f1, N:f2, C:f3

#include <trigg.incl>
; definition of external trigger output

;"acqt0=-(p1*2/3.1416)-0.5u"      ; baseopt correction

;*****definitions of delays*******
"spoff18=bf3*(-(cnst25-cnst26)/1000000)"
"d3=(1s/(4*cnst5))"
"d4=(d5-1u)"
"d6= d4-1u"
"d7= d3-p30"
```

```
"d10=3u"
"d0=0u"
"d20=d0/2"
"d23=d5-p18"
"d11=(1s/(1*cnst30))"
"in10=inf2/2"
"in23=inf2/2"
"d8=d5-p18"
;"d23=d10"
"DELTA8=d5-d10-p18"
"DELTA5=(d5)/(2*l0)-larger(p5,p6)"
"in0=inf1"


"acqt0=0"
baseopt_echo

;aqseq 321



1 ze
2 d1 do:N do:C
3u rpp10
3u rpp11
3u rpp12
3u rpp13
3u rpp14
3u rpp15
3u rpp16
3u rpp17
20u reset:H reset:N

;********first HN INEPT******
(p1 pl1 ph1):H     ;-Hy
```

```
d3
(center (p1*2.0 pl1 ph0):H (p2*2.0 pl2 ph0):N)
d3                                                    ; HxNz
(center (p1 pl1 ph3):H (p2 pl2 ph4):N)                ;HzNy
d3
(center (p1*2.0 pl1 ph0):H (p2*2.0 pl2 ph0):N)
d3                                                    ;Nx
;*************NCO INEPT and putting 1H along z and decouple ******
;1u cpds1:H
;d5
3
DELTA5
(center (p5*2.0 pl5 ph10):C (p6*2.0 pl6 ph10 ipp10):N)
DELTA5
lo to 3 times l0

;d5                                                   ;CzNy
(center (p21:sp21 ph5):C (p2 pl2 ph0):N)              ;CyNz
;1u cpds1:H
;******** CO evolution***********

(center (d0) (p1*2.0 pl1 ph0):H (p18:sp18 ph0):C (p2*2.0 pl2 ph0):N)
5u
(center (p21:sp21 ph0):C (p2 pl2 ph0):N)    ; pi/2 on CO ;CzNy

;************rephasing period CPMG C-H 2D
7
DELTA5
(center (p5*2.0 pl5 ph10):C (p6*2.0 pl6 ph10 ipp10):N)
DELTA5
lo to 7 times l0

;**********MISSISSIPPI *********
(p2 pl2 ph21):N
```

```
0.5u cpds4:H
d19*0.25
0.5u do:H

0.5u cpds5:H
d19*0.25
0.5u do:H

0.5u cpds4:H
d19*0.25
0.5u do:H

0.5u cpds5:H
d19*0.25
0.5u do:H
(p2 pl2 ph9):N              ;Nx

;*********** end MISSISSIPPI ******


;***********back NH INEPT to 1H*******
d3
(center (p1*2.0 pl1 ph0):H (p2*2.0 pl2 ph0):N)
d3                  ;NyHz
(center (p1 pl1 ph3):H (p2 pl2 ph6):N)   ;NzHx
d3
(center (p1*2.0 pl1 ph0):H (p2*2.0 pl2 ph0):N)   ;Hy
d3
0.5u cpds2:N
go=2 ph31
1m do:N
10m mc #0 to 2
;F1PH(ip5, id0)
F1PH(calph(ph5, +90), caldel(d0, +in0) )
;F2PH(calph(ph21, +90), caldel(d10, +in10) & caldel(d23, -in23))
```

```
exit

ph0=0
ph1=0 2
ph4= 0
ph3=1
;ph5= 1 1 1 1 3 3 3 3
ph5= 0 0 0 0 2 2 2 2
ph6=0
ph7=3
ph8=2
ph21=1
ph9= 1 1 3 3
ph10=0 1 0 1 1 0 1 0
ph11=0 1 0 1 1 0 1 0
ph12=0 1 0 1 1 0 1 0
ph13=0 1 0 1 1 0 1 0
ph14=0 1 0 1 1 0 1 0
ph15=0 1 0 1 1 0 1 0
ph16=0 1 0 1 1 0 1 0
ph17=0 1 0 1 1 0 1 0
ph20=1
ph31= 0 2 2 0 2 0 0 2
;ph31= 2 0 0 2 0 2 2 0
```

Appendix G

Simpson code for REDOR simulations

```
spinsys {
        channels 1H 15N
        nuclei   1H 15N
        #dipole_ave   1 2 10194 0 0 136 83.22
        dipole_ave   1 2 10194 0.1 0 100 120
        #shift     1 10p 100p 0.5 0 0 0

}

par {
        variable index   4

        np               32
        spin_rate        55000
        proton_frequency 500e6
        start_operator   I2x
        detect_operator  I2p
        method           direct
        crystal_file     zcw20
        gamma_angles     8
        sw               spin_rate/1
```

```
        variable tsw      1e6/sw
        # verbose           1101
        variable tr       1e6/spin_rate
        variable tr2      0.5e6/spin_rate
        variable rf       100000
        variable rf2      45454.5
        variable t180     0.5e6/rf
        variable d7       3
        variable d18      5
        variable d27      tr-d18*1.5-d7
        #variable d27      tr-d7
        variable d25      d7-0.5*d18
        #variable d25      d7
        variable p19      11
        variable d26     tr-d18-d7-0.5*p19
        #variable d26      tr-d7
}

proc pulseq {} {
        global par

        acq
        for {set i 2} {$i <= $par(np)} {incr i} {

                reset
                delay $par(d7)
                #delay $par(d18)
                pulse $par(d18) $par(rf) x 0 0
                for {set j 1} {$j <= $i} {incr j} {
                        delay $par(d27)
                        pulse $par(d18) $par(rf) x 0 0
                        delay $par(d25)
                        pulse $par(d18) $par(rf) y 0 0
                }
                delay $par(d26)
```

```
                pulse $par(p19) 0 0 $par(rf2) x
                delay $par(d26)
                for {set j 0} {$j <= $i} {incr j} {
                        pulse $par(d18) $par(rf) y 0 0
                        delay $par(d25)
                        pulse $par(d18) $par(rf) x 0 0
                        delay $par(d27)
                }
                pulse $par(d18) $par(rf) y 0 0
                delay $par(d7)
                acq
        }
}



##################### acquisition ###########

proc main {} {
        global par


        ### take arguments from external program #####

        if {[llength $::argv] != 3} {
                puts stderr "Usage: simpson $par(name).in <dipole
                exit
        }

        set dipole12 [lindex $::argv 1]
        set eta12  [lindex $::argv 2]

        ##############################################
```

```
        set f [fsimpson [list \
        [list dipole_ave_1_2_aniso $dipole12] \
        [list dipole_ave_1_2_eta $eta12] \
        ]]

        for {set j 1} {$j <= $par(np)} {incr j} {

                set val [expr [findex $f $j -re]]
                puts $val
        }

        #set f [fsimpson]
        #puts $f
        #fsave $f $par(name).fid
        funload $f

}
```